LIGHT SCATTERING STUDIES OF SOLIDS AND ATOMIC VAPORS

by

Tai-chang Chiang

Lawrence Berkeley Laboratory
University of California
Berkeley, California 94720

LIGHT SCATTERING STUDIES OF SOLIDS AND ATOMIC VAPORS

Tai-Chang Chiang

ABSTRACT

We have used the general technique of light scattering and luminescence to study the properties of a number of material systems. First, multi-phonon resonant Raman scattering up to four phonons in GaSe and one- and two-phonon resonant Raman scattering in the mixed GaS_xSe_{1-x} crystals with $x \leq 0.23$ are investigated. The results can be explained by a simple theory in which the dispersion of the resonant behavior is dominated by resonances with the 1s direct exciton states. Second, the observation of one-phonon resonant Raman scattering in HfS_2 is reported. The dispersion of the Raman cross section shows no sharp structures attributable to excitonic transitions, and is therefore believed to be due to resonances with band to band transitions. The result is used to determine the position of the direct gap of HfS_2. Third, the first observation of the π-polarized one-magnon luminescence sideband of the $^4T_{1g}(^4G) \rightarrow {}^6A_{1g}(^6S)$ excitonic transition in antiferromagnetic MnF_2 is presented. The theory of Loudon is used to fit the experimental spectrum quantitatively. An effective temperature of the crystal is deduced from the simultaneously observed antiStokes sideband emission. Using pulsed excitation and detection, we have also observed multi-magnon (≤ 7) excitonic luminescence sidebands in MnF_2, $KMnF_3$, and $RbMnF_3$. A simple model based on two-ion local exchange is proposed to explain the results qualitatively. Fourth, the first observation of two-magnon resonant Raman

scattering in MnF_2 around the magnon sidebands is reported. The resonant scattering involves a different mechanism than the non-resonant case and leads to a number of new results. A simple theoretical description explains the experimental observations. Fifth, a detailed theory of exciton-exciton interaction in MnF_2 is developed to explain and to predict the experimental results on two-exciton absorption, high level excitation, and exciton-exciton scattering. Possible experiments on exciton-exciton and exciton-magnon interactions in MnF_2 are proposed and examined. Sixth, Brillouin scattering is used to obtain the five independent elastic constants of the layered compound GaSe. The results show clear elastic anisotropy of the crystal. Resonant Brillouin scattering near the absorption edge is also studied, but no resonant enhancement is found. Seventh, two-photon parametric scattering in sodium vapor is studied. Phase matching angles and scattering cross sections are calculated for a given set of experimental conditions. Preliminary experiment shows that the expected signal is much less than the sodium dimer fluorescence.

Acknowledgements

I would especially like to thank:

Professor Y. R. Shen, my thesis adviser, for his guidance and help;

Dr. N. M. Amer, Dr. J. P. Voitchovsky, Dr. J. Camassel, Dr. J. Dumas, Dr. J. Davies, and Dr. P. Salvi, co-workers and co-authors of our publications, whose help was invaluable;

Professor W. D. Knight, for providing us some of the samples used in the experiments;

Professor L. M. Falicov, for helpful discussions;

Rita Jones, for being so nice and for typing the manuscript.

This work was supported by the Division of Materials Sciences, Office of Basic Energy Sciences, U. S. Department of Energy.

Table of Contents

I. General Introduction

Laser light scattering has been widely used to study many fundamentally important properties of materials. Raman scattering and Brillouin scattering are among the most commonly used techniques. Raman scattering, loosely defined as light scattering off elementary excitations of higher frequencies, usually probes excitations in the energy range from about 10 to 10^4 cm^{-1}. Brillouin scattering, defined as light scattering off an elementary excitation of the acoustic branch, probes the energy range from about 0.01 cm^{-1} to 10 cm^{-1}. These two techniques have been used quite extensively to study the phonons, polaritons, ripplons, magnons, free carriers in semiconductors, impurity excitations, electronic excitations of an atom, etc. They provide rather detailed information about the energies and dispersions of the elementary excitations and their mutual interactions. Since the advent of tunable dye lasers, a new area in light scattering has appeared. By tuning the incoming photon frequency to resonate with the states of the material system, interesting new phenomena often show up. The spectral properties of the system in the range of energies of the photon itself can be directly investigated and the interactions between various elementary excitations can be probed. Thus, resonant Raman scattering and resonant Brillouin scattering have become extremely important spectroscopic tools. Strong enhancement of the phonon Raman cross sections and the appearance of multi-phonon modes near resonance are among the commonly observed resonant effects in semiconductors. Such an example is given in Section II on resonant Raman scattering in GaSe and mixed GaS_xSe_{1-x} crystals. We will see there that the dispersion of the photon-exciton interaction and the strong ex-

citon-phonon coupling are responsible for the resonant effects. This connection is actually also used in Section III to deduce the position of the direct gap of HfS_2, which has been controversial and difficult to determine by other means due to the weak transition moment associated with the direct gap. Magnetic excitations are also interesting subjects for resonant Raman study. Section V deals with resonant Raman scattering by two magnons in antiferromagnetic MnF_2. The symmetry of the wave functions, selection rules, and specific electron-spin coupling mechanisms lead to interesting new effects in this case. Although perfect theoretical fits to the experimental data are not available due to the inherent many-body nature of the above problems, the qualitative behaviors can be understood, interesting physics can be isolated, and even important physical parameters can often be deduced. We have also performed Brillouin scattering experiment in GaSe. Brillouin scattering can be considered as light diffraction by a sound wave as well as light scattering off an acoustic phonon. It can yield useful information connecting the macroscopic and microscopic properties. GaSe is chosen as the subject of study because of its layered structure and possible two-dimensional behaviors.

In a Raman or Brillouin process, the number of elementary excitations involved is in general small such that the phase memory is preserved during such a process. In contrast, a luminescence process in general refers to a light scattering process involving a large number of elementary excitations. After laser excitation, the system relaxes to a quasi-steady excited state and radiatively recombines. The phase memory is lost roughly in the sense that the system forgets at the time of radiative recombination how it has been prepared. The spectral features are

more characteristic of the properties of the system rather than the manner of excitation. A good deal of information can be obtained and often complements the Raman scattering results. Single and multiple phonon sidebands of electronic transitions are well-known luminescence phenomena in solids. We present in Section IV the study on single and multiple magnon sidebands of excitonic transitions in some antiferromagnetic crystals. The phonon sidebands are relatively weak in this case due to the spin selection rules peculiar to a magnetic system.

A Raman or Brillouin process is usually instantaneous while a luminescence process is characterized by finite rise and fall times. It is interesting to study the time evolution of a light scattering process since this is directly related to the dynamics of the system. Ordinary CW light scattering techniques yield only static or kinetic information about the system. With the introduction of short tunable laser pulses and fast electronics, the system can be selectively (resonantly) prepared and then probed or monitored at a later time. This time-resolved resonant light scattering has received much attention and is a fast growing area of research. The wealth of information that can be obtained is well illustrated in Section VI on the exciton-exciton and exciton-magnon interactions in MnF_2. The closely related high excitation experiment in MnF_2 is also discussed there. MnF_2 is chosen as the subject of study since it is a relatively simple system exhibiting a lot of interesting phenomena. It is a "clean" system to test the many-body theory.

Finally in Section VIII, we study light scattering of a different kind, namely, two-photon parametric scattering in sodium vapor. A parametric process is a nonlinear optical process in which two new frequencies are generated simultaneously. We consider sodium vapor as the nonlinear

medium since it is a simple atomic system whose optical properties can be calculated easily. A parameteic process is of practical importance as well as great theoretical interst, because it may lead to the construction of new tunalbe coherent sources.

II. Resonant Raman Scattering in GaSe and GaS_xSe_{1-x}

A. Introduction

Resonant Raman scattering (RRS) around excitonic transitions in solids has been a subject of extensive investigation in recent years.[1] Among the various semiconductors, the layered GaSe and GaS_xSe_{1-x} crystals seem to be particularly worth studying. They have direct as well as indirect exciton states near the band gap with relative positions varying with x. In this section, I will present[2] (i) measurements on multi-phonon RRS up to four phonons in pure GaSe and (ii) one- and two-phonon RRS in GaS_xSe_{1-x} with $x < 0.23$.

The layered compounds GaS and GaSe form a continuous series of mixed crystals GaS_xSe_{1-x} with $0 \leq x \leq 1$.[3] The crystal structures show three different types of stacking of the layers: ε, γ and β, which have been described in the literature.[4] For $0 \leq x < 0.23$, the ε-stacking dominates and is shown in Fig. 1.

Optical studies including absorption,[3,5] reflection[6] and photoluminescence[3,7] have been recently reported. It has been found that in each mixed crystal GaS_xSe_{1-x} with $0 \leq x < 0.25$ at liquid N_2 temperature, there exist a direct exciton at[8]

$$\omega_{dx}(x) = 2.102 + 0.728x(eV) \qquad (1)$$

with a binding energy of 20 meV, and an indirect exciton at[8]

$$\omega_{ix}(x) = 2.064 + 0.520x(eV) \qquad (2)$$

with a binding energy of ~ 35 meV.

The phonon modes of GaS_xSe_{1-x} have been studied by infra-red[9] and nonresonant Raman spectroscopy.[9,10] Corresponding to change in composition of the mixed crystals, some phonon modes show the two-mode behavior, while others show either the one-mode or the local-mode behavior.[10] It is interesting to see how the various modes behave as the exciting laser frequency varies around the excitonic transitions. Such study has already been reported in pure GaSe crystals.[11] The $A_2''^{(2)}$ (LO) mode at 247 cm^{-1} and $E'^{(2)}$ (LO) mode at 255 cm^{-1}, respectively, show a strong resonance enhancement, while the two A_1' modes at 135 and 310 cm^{-1} show much less apparent resonant behavior as the exciting laser frequency approaches the direct exciton. The strong enhancement of the two LO modes (unresolved in mixed crystals with $x > 0.1$) is presumably due to the Fröhlich interaction between LO phonons and excitons. In particular, the $E'^{(2)}$ (LO) phonon (255 cm^{-1}) appears to couple most strongly with the exciton states. As a result, we were able to observe multi-phonon modes up to four phonons involving $E'^{(2)}$ (LO) in pure GaSe and $2E'^{(2)}$ (LO) modes in the mixed crystals.

B. Experiment and Results

Monocrystalline samples of GaS_xSe_{1-x} with $x \approx 0$, 0.05, 0.12, 0.17, and 0.225 were grown by the Bridgeman technique. Back-scattering from a polished surface parallel to the crystal $\hat{c}$-axis was used in the measurements because of the larger oscillator strength in this configuration.[12] In order to reduce the luminescence background to a tolerable level without appreciably broadening the exciton line widths, the samples were immersed in liquid N_2 during the measurements. Before each meeasurment,

the Janis dewar holding the samples and the liquid N_2 coolant was pumped down to a pressure about 400 mmHg to reduce the temperature. The dewar was then backfilled and pressurized with He gas to eliminate N_2 bubbling. Temperature was stable within a few degrees during the measurements. The excitation was provided by a homebuilt jet stream CW dye laser with a typical output power of 100 mW. Rhodamine 6G, rhodamine 110 and coumarine 6 dyes were used as the lasing media to cover the spectral range from 6600 Å to 5300 Å. The laser light was focused onto the sample surface by a lens. Local heating was unimportant since the spectra normalized over laser power were independent of the incident power. The scattered light was collected by a F/1.6 projection lens, analyzed by a Spex 1400 double monochromator, and finally detected by a cooled FW-130 photomultiplier. Standard photon counting electronics and a multichannel analyzer were used to collect the data.

We will concentrate only on the strongly enhanced Raman modes. The observed Raman shifts of the $1E'^{(2)}$ (LO) and $2E'^{(2)}$ (LO) modes for x = 0, 0.05, 0.12, 0.17, 0.225 and the shifts of the $3E'^{(2)}$ (LO), $2E'^{(2)} + A_1'$ (310 cm^{-1}) and $4E'^{(2)}$ (LO) modes for pure GaSe are given in Table I. All numbers are within ± 1 cm^{-1} accuracy.

The experimental results are summarized in Figs. 2, 3, and 4. Figures 2 and 3 show the Raman cross sections of the one- and two-$E'^{(2)}$ (LO) phonon modes respectively, as functions of exciting laser frequency and sample composition. Figure 4 shows the Raman cross sections of the $3E'^{(2)}$ (LO), $2E'^{(2)}$ (LO) + A_1' (310 cm^{-1}), and $4E'^{(2)}$ (LO) modes of pure GaSe. All data points have been corrected for sample absorption according to the following formula[11]

$$\sigma_R = \frac{\alpha_\ell + \alpha_s + 3.93\ \mathrm{cm}^{-1}}{1 - \exp[-(\alpha_\ell + \alpha_s + 3.93\ \mathrm{cm}^{-1})d]} (1 - R_\ell)^{-1}(1 - R_s)^{-1}\sigma \quad (3)$$

where σ_R is the corrected Raman cross section, σ the uncorrected Raman cross section normalized over the laser power. α_ℓ, R_ℓ, α_s, R_s are the absorption coefficients and sample reflectances at the laser frequency and the scattered photon frequency respectively. d is the sample thickness. The factor 3.93 cm^{-1} takes account of the finite collecting depth of our lens. The absorption coefficient for GaSe was taken from Ref. 11 and those for the mixed crystals were measured in our laboratory in a standard manner.[13]

C. Theory

To explain our results, we use a simple cascade theory.[14] We assume the following absorption-emission processes (in decreasing order of importance) dominating in the n-phonon RRS:

1) Incoming photon at ω_1 excites an electron-hole (e-h) pair in the band continuum. The e-h pair then decays into the $k \simeq 0$ ls direct exciton by successively emitting n phonons. The direct exciton finally recombines and emits a Stokes photon at ω_s.

2) Incoming photon excites an e-h pair in the band continuum. The e-h pair decays into a $k \neq 0$ ls direct-exciton state by successively emitting $m(1 \leqslant m \leqslant n - 1)$ phonons. The direct exciton then recombines by an $(n - m)$-phonon-assisted transition and emits a Stokes photon.

3) Incoming photon excites the $k \simeq 0$ ls direct exciton. The direct exciton then either recombines by an n-phonon-assisted transition or decays into the ls indirect exciton by emitting a phonon and the resulting indirect exciton recombines by an $(n - 1)$-phonon-assisted transition.

Since the absorption curves of these crystals are rather flat immediately beyond the direct-exiton absorption peak, we can assume that the dispersion of the RRS curves is mainly due to resonances with the exciton states. The one-phonon cross-section can therefore be written approximately as a direct product of 2 resonant terms for i) the incident and ii) the scattered photon energies:

$$\sigma_R(\omega_{ph}) = A_1[\alpha(\omega_1) + B_1] \cdot [\alpha(\omega_S) + C_1], \qquad (4)$$

$\alpha(\omega)$ describes the direct-exciton absorption peak deduced from the absorption measurements and A_1, B_1 and C_1 are constants. The solid curves in Fig. 2 were actually obtained from Eq. (4) by using A_1, B_1 and C_1 as adjustable parameters. The nonresonant terms B_1 and C_1 were set equal to 650 cm^{-1} and 500 cm^{-1} respectively, for all the five crystals; A_1 was merely a normalizing constant. Our curves fit the experimental data points very well and *a posteriori* confirm the dominance of the 1s direct exciton.

By assuming all resonances to have the Lorentzian line shape, we can also write down the approximate analytical expression for the two-phonon Raman cross-section as

$$\sigma_R(2\omega_{ph}) = A_2\left[(\omega_1 - \omega_{dx} - 2\omega_{ph})^2 + \Gamma_{d0}^2\right]^{-1} + B_2F(\omega_1 - \omega_{dx} - \omega_{ph},\Gamma_d)$$

$$+ \left[C_2F(\omega_1 - \omega_{ix} - \omega_{ph},\Gamma_i) + D_2\right]\left[(\omega_1 - \omega_{dx})^2 + \Gamma_{d0}^2\right]^{-1}. \qquad (5)$$

For 3-phonon RRS, we have

$$\sigma_R(2\omega_{ph} + \omega'_{ph}) = A_3\left[(\omega_1 - \omega_{dx} - 2\omega_{ph} - \omega'_{ph})^2 + \Gamma_{d0}^2\right]^{-1}$$

$$+ B_3F(\omega_1 - \omega_{dx} - 2\omega_{ph},\Gamma_d) + C_3F(\omega_1 - \omega_{dx} - \omega_{ph},\Gamma_d). \tag{6}$$

For 4-phonon RRS, we have

$$\sigma_R(4\omega_{ph}) = A_4\left[(\omega_1 - \omega_{dx} - 4\omega_{ph})^2 + \Gamma_{d0}^2\right]^{-1} + B_4F(\omega_1 - \omega_{dx} - 3\omega_{ph},\Gamma_d)$$

$$+ C_4F(\omega_1 - \omega_{dx} - 2\omega_{ph},\Gamma_d). \tag{7}$$

In the above expressions, A_i, B_i, C_i and D_i are constants to be used as adjustable parameters; ω_{ph}, ω_{dx}, ω_{ix} are the frequencies of the optical phonon, direct exciton at k = 0, and indirect exciton at the bottom of the indirect exciton band respectively; Γ_d and Γ_i are the damping constants for the direct and indirect excitons respectively, with Γ_{d0} reserved specifically for the k = 0 direct exciton. The function F has the form

$$F(\Delta\omega,\Gamma) = \int_0^{Y_c} y^{\frac{1}{2}}((\Delta\omega - y)^2 + \Gamma^2)^{-1}dy, \tag{8}$$

where Y_c is a somewhat arbitrary cut-off chosen as $\frac{3}{2}$ times the exciton binding energy. The value of Γ_{d0} for each crystal is deduced from the corresponding absorption curve; Γ_d and Γ_i are taken to be $2\Gamma_{d0}$. (Dependence of theoretical curves on Γ_d and Γ_i is not critical.) For pure GaSe, the separation between direct and indirect exciton states is fairly close to the phonon frequency involved. Accordingly, we can drop the nonresonant D_2 term in Eq. (5). For the mixed crystals, it is, however, more

appropriate to drop the C_2 term.

The solid curves in Fig. 3 were obtained from Eq. (5) with $A_2:B_2:C_2:D_2$ = 12:1:10:0, 5:1:0:12 and 12:1:0:22 for x = 0, 0.12, and 0.17 respectively. The solid curves in Fig. 4 were obtained from Eqs. (6) and (7) with $A_3:B_3:C_3$ = 12:1:0.2 and 20:1:0.2 for $3E'^{(2)}$ (LO) and $2E'^{(2)}$ (LO) + A_1' (310 cm^{-1}) modes respectively, and $A_4:B_4:C_4$ = 12:1:0.2 for the $4E'^{(2)}$ (LO) mode in pure GaSe.

It is seen that the solid theoretical curves in Fig. 3 deviate from the experimental data at the low-energy tail. This is because we have assumed a Lorentzian line shape for all the transitions involved. If we replace the Lorentzian function in Eqs. (5) and (8) by the observed line shape $a(\omega,\Gamma)$ of the direct-exciton absorption peak, with Γ still being the half width, the theoretical curves remain essentially unchanged for $\omega_1 > \omega_{dx}$, but change into the dashed curves for $\omega_1 < \omega_{dx}$. The agreement between theory and experiment is then very good. The near-Gaussian line shape of excitonic transitions could be due to inhomogeneous broadening.

The theoretical curve for $GaS_{0.225}Se_{0.775}$ in Fig. 3 was obtained with the superposition of another Lorentzian-type resonance at $\omega_1 = \omega_{ix}$ with Γ_{i0} = 24 meV. It then describes the experimental results satisfactorily. This indicates that direct laser excitation of the indirect exciton is also operative in RRS although the contribution is relatively weak. The same resonance peak at $\omega_1 = \omega_{ix}$ was seen in the raw data of RRS in the other crystals, but, after absorption correction, was masked off by the much stronger direct-exciton resonance. This is presumably because the separation between direct and indirect excitons in these crystals is too small. Although momentum conservation forbids the direct excitation of indirect excitons, stacking faults in the crystals

can easily induce such a process.[11] The $\omega_1 \sim \omega_{ix}$ resonance should also appear in the one-phonon RRS in GaS_xSe_{1-x}. It was indeed observed in the raw data as a shoulder on the strong resonance tail, but became invisible after absorption correction.

D. Conclusions

The good agreement between theory and experiment in Figs. 2, 3, and 4 shows that the cascade description is appropriate and the dispersion of RRS in GaS_xSe_{1-x} is indeed dominated by resonances with the exciton states.

References

1. See, for example, P. Y. Yu and Y. R. Shen, Phys. Rev. B12, 1377 (1975) and references therein, and papers presented at the III International Conference on Light Scattering in Solids, Campinaas, Brazil, July 1975.
2. T. C. Chiang, J. Camassel, Y. R. Shen, and J. P. Voitchovsky, Solid State Commun. 19, 157 (1976); J. Camassel, T. C. Chiang, Y. R. Shen, J. P. Voitchovsky, and N. M. Amer, Solid State Commun. 19, 483 (1976); T. C. Chiang, J. Camassel, J. P. Voitchovsky, and Y. R. Shen, Il Nuovo Cimento 38B, 301 (1977).
3. A. Mercier, E. Mooser, and J. P. Voitchovsky, J. Lumin. 7, 241 (1973), and references therein.
4. K. Schubert, E. Dorre, and M. Kluge, Zeits. Metall. 46, 216 (1955); P. Weilink and H. Hann, Zeits. Naturf. 16b, 713 (1961).
5. J. L. Brebner, J. Phys. Chem. Solids 25, 1427 (1964); E. Aulich, J. L. Brebner, and E. Mooser, Phys. Stat. Solidi 31, 129 (1969).
6. M. Schluter, J. Camassel, S. Kohn, J. P. Voitchovsky, Y. R. Shen, and M. L. Cohen, Phys. Rev. B13, 3534 (1976).
7. A. Mercier, E. Mooser, and J. P. Voitchovsky, Phys. Rev. B12, 4307 (1975).
8. Equations (1) and (2) were deduced from the experimental data of J. P. Voitchovsky.
9. J. J. Wieting and J. L. Verble, Phys. Rev. B5, 1473 (1972).
10. M. Hyaek, O. Brabman, and R. M. A. Lieth, Phys. Rev. B8, 2772 (1973); A. Mercier and J. P. Voitchovsky, Solid State Commun. 14, 757 (1974).
11. R. M. Hoff and J. C. Irwin, Phys. Rev. B10, 3469 (1974); J. Reydellet

and J. M. Besson, Solid State Commun. 17, 23 (1975), and unpublished results.

12. J. D. Wasscher and J. Dieleman, Phys. Lett. 39A, 279 (1972); A. Bourdon and F. Khelladi, Solid State Commun. 9, 1715 (1971).

13. R. Le Toullec, N. Piccioli, M. Mejatty, and M. Balkanski, Il Nuovo Cimento 38B, 159 (1977).

14. R. M. Martin and C. M. Varma, Phys. Rev. Lett. 26, 1241 (1971).

Table I

Raman shift for various one and multiphonon modes in GaS_xSe_{1-x}.

Shift	x				
	0	0.05	0.12	0.17	0.225
$E'^{(2)}$ (LO)	255	254	251	250	249
$2E'^{(2)}$ (LO)	510	509	504	500	499
$3E'^{(2)}$ (LO)	767				
$2E'^{(2)} + A'_1$	821				
$4E'^{(2)}$ (LO)	1018				

Figure Captions

Fig. 1 Crystal structure of GaS_xSe_{1-x} with $0 \leq x < 0.23$. The crystal symmetry group is D_{3h}.

Fig. 2 Raman cross section of the $E'^{(2)}$ (LO) mode as a function of laser frequency. ○, ▲, □, ●, and △ are data points for GaS_xSe_{1-x} with x = 0, 0.05, 0.12, 0.17, and 0.225 respectively. Solid curves are obtained from theory in the text.

Fig. 3 Raman cross section of the two-phonon $2E'^{(2)}$ (LO) mode as a function of laser frequency. ○, ▲, □, ●, and △ are data points for GaS_xSe_{1-x} with x = 0, 0.05, 0.12, 0.17, and 0.225 respectively. Solid and dashed curves are obtained from theory in the text.

Fig. 4 Raman cross sections of the three- and four-phonon modes of pure GaSe: ○ $3E'^{(2)}$, ◒ $2E'^{(2)} + A_1'$ (310 cm^{-1}), △ $4E'^{(2)}$. Solid curves are obtained from theory in the text.

Figure 1

GaS_xSe_{1-x}

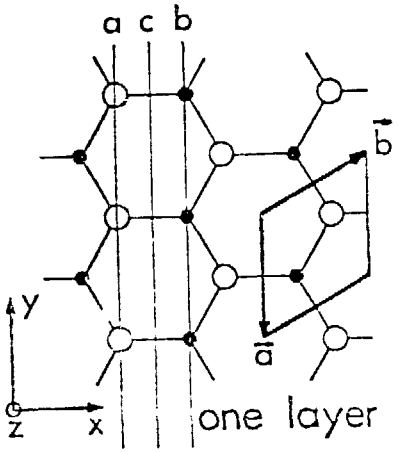

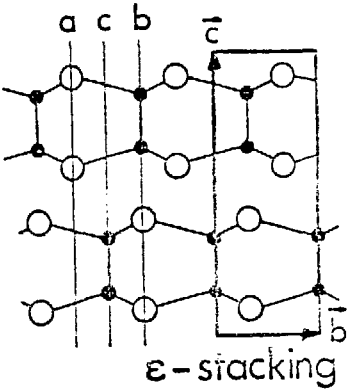

O Se or S atom

• Ga atom

XBL 764-1031

Figure 2

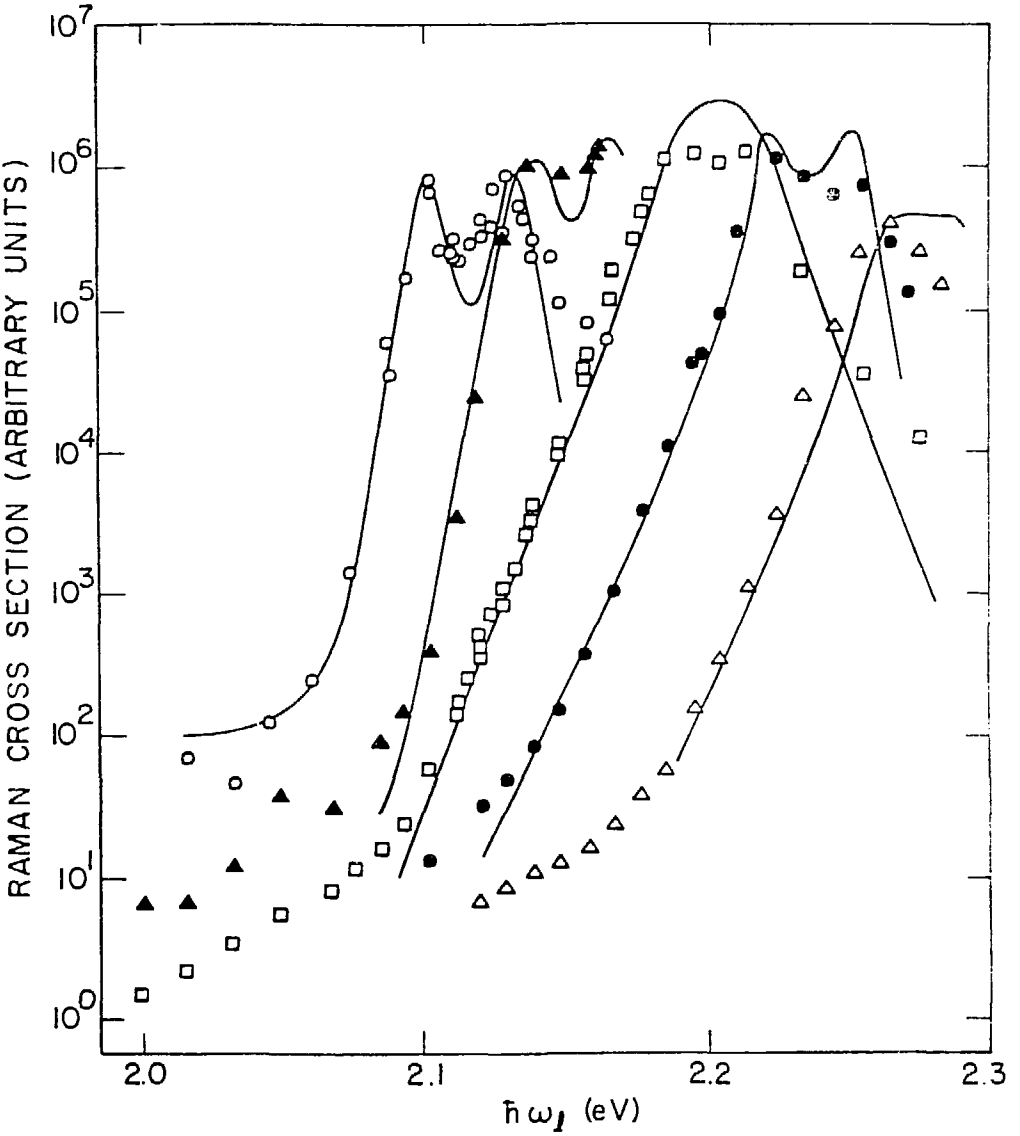
RAMAN CROSS SECTION (ARBITRARY UNITS)
10^7
10^6
10^5
10^4
10^3
10^2
10^1
10^0
2.0
2.1
2.2
2.3
$\hbar\omega_l$ (eV)
XBL761-6127

Figure 3

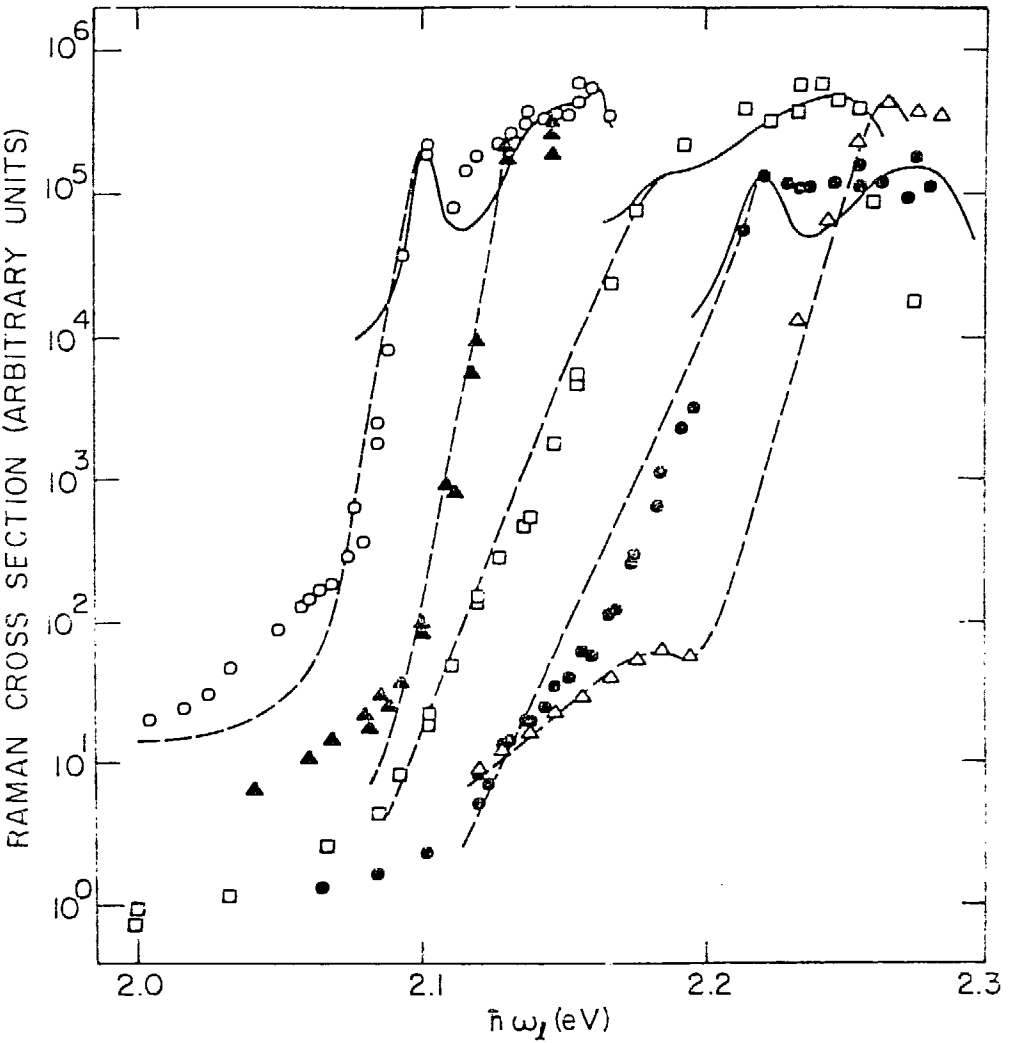
RAMAN CROSS SECTION (ARBITRARY UNITS)
10^6
10^5
10^4
10^3
10^2
10^1
10^0
2.0
2.1
2.2
2.3
$\hbar\omega_l$ (eV)
XBL 761-6126

Figure 4

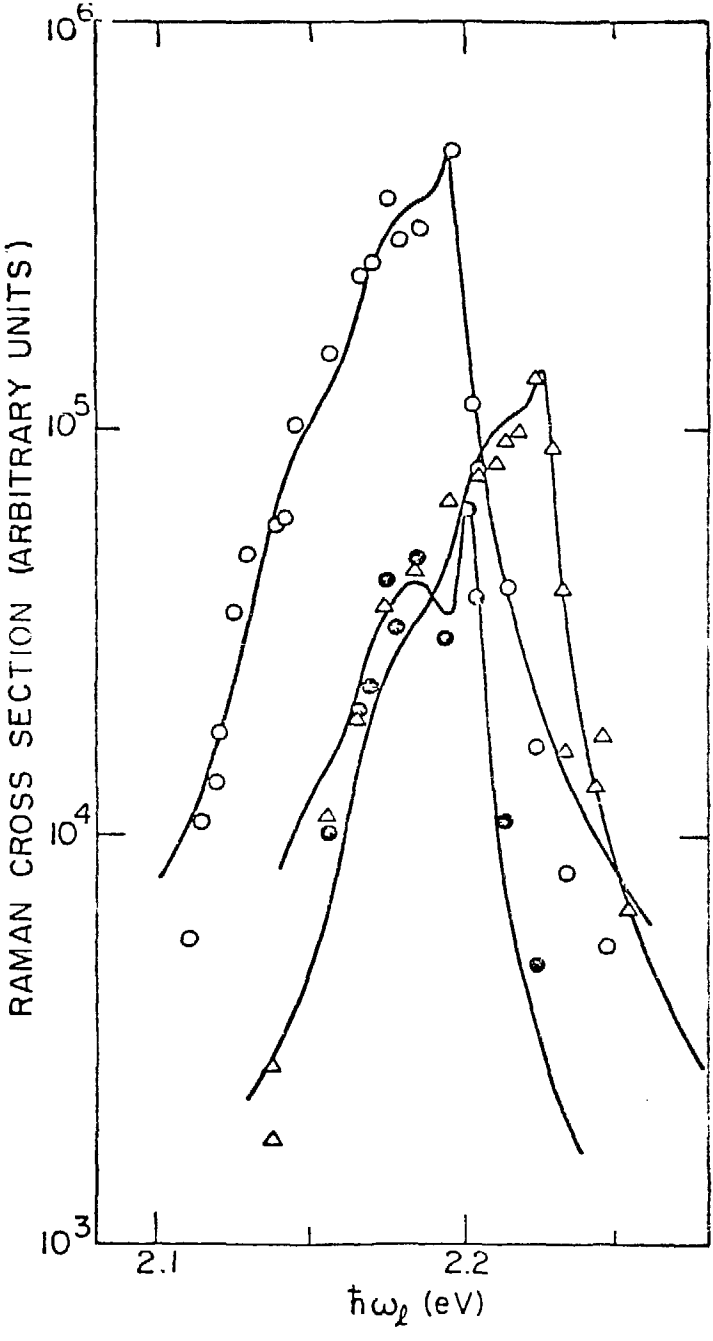
10^6
10^5
10^4
10^3
RAMAN CROSS SECTION (ARBITRARY UNITS)
2.1
2.2
$\hbar\omega_l$ (eV)

III. Resonant Raman Scattering in HfS_2

A. Introduction

Resonant Raman spectroscopy has been successfully applied to many semiconductors.[1] However, no such study has been made on transition metal dichalcogenides. In this section, I will present my recent experimental results on such a compound, viz., HfS_2.

Many transition metal dichalcogenides form layered compounds.[2] A typical layer consists of a plane of metal atoms sandwiched between two planes of the chalcogenides. Three different stacking polytypes are usually found: 1T, 2H, and 3R. The group IV B compounds including HfS_2 crystallize only in the 1T polytype. Within a layer, each metal atom is octahedrally surrounded by six chalogens as shown in Fig. 1. Due to the saturation of the p-orbitals, HfS_2 is a semiconductor.

The phonon spectra of HfS_2 have been investigated by infrared reflectance measurements[3] and non-resonant Raman spectroscopy.[4] With D_{3d} space group symmetry, there are four infrared-active modes $2A_{2u} + 2E_u$ and two Raman active modes $A_{1g} + E_g$.

The electronic band structures have been studied by optical transmission[5,6] and reflectivity[6,7] measurements. These results have been compared with theoretical band structure calculations.[7-9] It is generally believed it is an indirect-gap semiconductor with gap energy around 1.9 eV. However, the energy of the lowest direct transition is still the subject of much controversy. Fong, Camassel, Kohn and Shen (FCKS)[7] concluded from their work the lowest direct transition was $\Gamma_2^- \rightarrow \Gamma_3^+$ at ~ 2.4 eV. In contrast, Murray, Brumley, and Yoffe (MBY)[8] obtained 3.47 eV and Mattheiss[9] obtained 3.43 eV for the transition $L_3 \rightarrow L_1$ as the lowest. Since

the Raman cross sections should show resonant enhancement near the direct gap, resonant Raman spectroscopy provides a means to locate this lowest transition. This approach is demonstrated here.

B. Experiment and Results

We have measured the transmission of thin platelets of HfS_2 at both room temperature and liquid N_2 temperature. Very thin samples were obtained by repeated cleaving with adhesive tapes.[2] The thinnest sample obtainable was about 5 μ in thickness. Due to the strong absorption, the range of our transmission measurements was limited. The square root of the measured room temperature absorption coefficient as a function of photon energy is shown in Fig. 2; it consists of four straight line segments. At liquid N_2 temperature, the absorption curve is simply shifted by 0.096 eV toward higher energy side in agreement with Ref. 6.

The Raman setup used has been described in Section II. Since only thin samples were available, a back scattering geometry from a cleaved face was employed. Samples were immersed in liquid N_2 during the measurements. Both Raman active modes were observed: A_{1g} at 338 cm^{-1} and E_g at 263 cm^{-1}. The Raman cross sections, corrected for absorption in the manner described in Section II, are shown in Fig. 3 as functions of incident laser photon energy.

We have also performed luminescence measurements. No luminescence was observed even at He temperature indicating the existence of fast non-radiative relaxation processes.

C. Theory and Discussions

From Fig. 2, the onset of absorption is described by

$$\alpha(cm^{-1}) = \begin{cases} 0 & , \quad \omega < 1.820 \text{ eV} \\ 4154 \times (\omega - 1.82)^2 & , \quad 1.820 < \omega < 2.081 \text{ eV} \end{cases} \qquad (1)$$

which is characteristic of phonon-assisted indirect transitions.[10] Therefore, the lowest gap of HfS_2 is indirect with a gap energy around 1.9 eV. The kinks observed at 2.081 eV, 2.289 eV, and 2.417 eV on the absorption curve are probably due to other phonon-assisted transitions.

The Raman cross sections, shown in Fig. 3, showns resonant enhancement by about one order of magnitude within our dye laser tuning range. This indicates the onset of direct transitions should be near 2.2 eV. Since no excitonic structures in absorption have been observed, we assume the enhancement is due to direct band to band transitions. With parabolic conduction and valence bands and neglecting contributions from higher transitions, it can be shown,[11] for $\omega_\ell < \omega_g$,

$$\sigma(\omega_\ell) = A[\sqrt{\omega_g + \omega_o - \omega_\ell} - \sqrt{\omega_g - \omega_\ell}]^2 \qquad (2)$$

where $\sigma(\omega_\ell)$ is the Raman cross section at laser frequency ω_ℓ, A a constant, ω_g the band gap energy, and ω_o the phonon energy.

The solid curves in Fig. 3 were obtained by least square fitting using Eq. (2) with ω_g as an adjustable parameter. The detailed resonant enhancement behavior is only fairly described by Eq. (2) due to the assumption we have made. However, the value of ω_g determined in this way, being 2.231 eV at liquid N_2 temperature, should locate the onset of direct transitions fairly accurately. This value is close to FCKS's 2.4 eV at He temperature, and very different from MBY's 3.47 eV and Mattheiss's 3.43 eV. We therefore assign the direct gap to be $\Gamma_2^- \rightarrow \Gamma_3^+$ at the zone center with an energy of 2.231 eV at liquid N_2 temperature.

By taking into account the shift of absorption by 0.096 eV from liquid N_2 to room temperature, ω_g should be 2.135 eV at room temperature. The kink observed in absorption at 2.081 eV (Fig. 2) is then interpreted to be a phonon-assisted hot band transition involving the direct gap and a phonon of energy 54 meV ($\sim$ 400 cm^{-1}). The next higher kink in absorption at 2.289 eV is then naturally interpreted to be due to the phonon-assisted onset of the $\Gamma_3^- \rightarrow \Gamma_3^+$ transition involving the second highest valence band and the bottom conduction band. The separation between the two top valence bands is then 2.289 eV - 2.081 eV = 0.208 eV, in good agreement with theoretical predictions.[7] The accuracy of the numbers mentioned here should not be overemphasized, but we do obtain a consistent picture.

D. Conclusions

By applying resonant Raman spectroscopy to HfS_2, we have been able to determine the position of the direct gap. The gap value obtained is in good agreement with that obtained by FCKS. The dispersion of the Raman cross sections is due to resonances with the direct gap.

References

1. See, for example, M. A. Washington, A. Z. Genack, H. Z. Cummins, R. H. Bruce, A. Compaan, and R. A. Forman, Phys. Rev. B15, 2145 (1977) and references cited in Section II.
2. J. A. Wilson and A. D. Yoffe, Adv. Phys. 18, 193 (1969).
3. G. Lucovsky, R. M. White, J. A. Benda, and J. F. Revelli Phys. Rev. B7, 3859 (1973).
4. M. I. Nathan, M. W. Shafer, and J. E. Smith, Bull. Am. Phys. Soc. 17, 336 (1972).
5. A. R. Beal, J. C. Knights, and W. Y. Liang, J. Phys. C5, 3531 (1972).
6. D. L. Greenaway and R. Nitsche, J. Phys. Chem. Solids 26, 1445 (1965).
7. C. Y. Fong, J. Camassel, S. Kohn, and Y. R. Shen, Phys. Rev. B13, 5442 (1976).
8. R. B. Murray, R. A. Bromley, and A. D. Yoffe, J. Phys. C5, 746 (1972).
9. L. F. Mattheiss, Phys. Rev. B8, 3719 (1973).
10. R. J. Elliott, Phys. Rev. 108, 1384 (1957).
11. R. Loudon, Adv. Phys. 13, 423 (1964).

Figure Captions

Fig. 1 Hexagonal unit cell of HfS_2 (left) and the octahedral continuation within one layer (right).

Fig. 2 The square root of room temperature absorption coefficient as a function of photon energy.

Fig. 3 Raman cross sections of HfS_2 as functions of incident laser photon energy. Solid curves are theoretical curves discussed in the text.

Figure 1

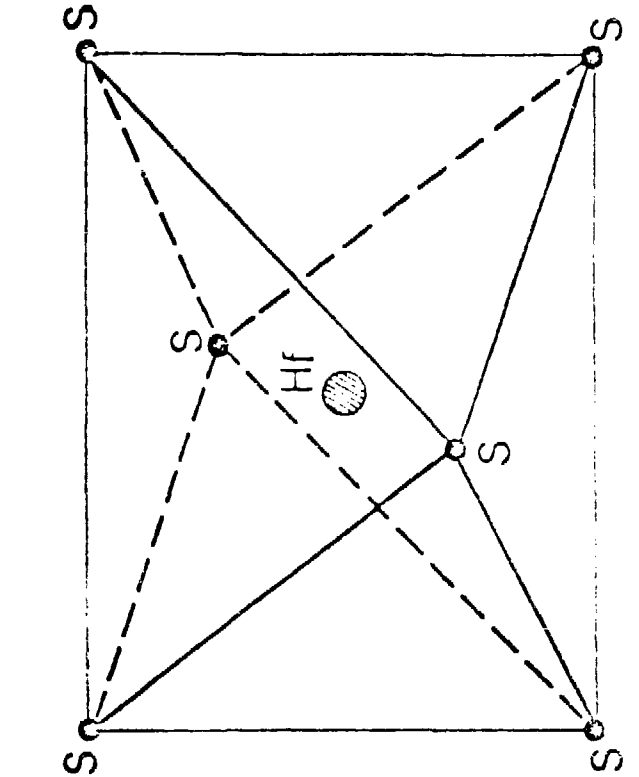

XBL 759-7161

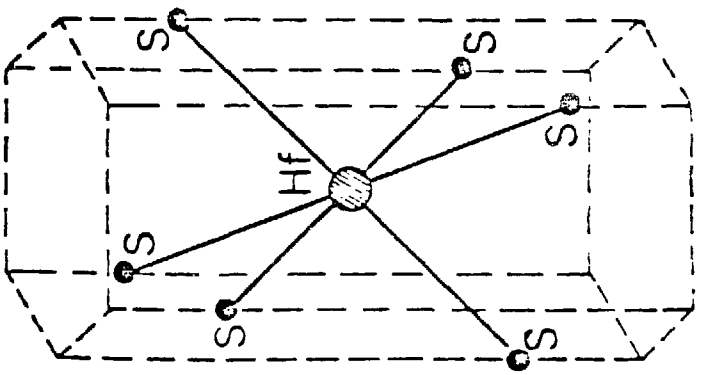

Figure 2

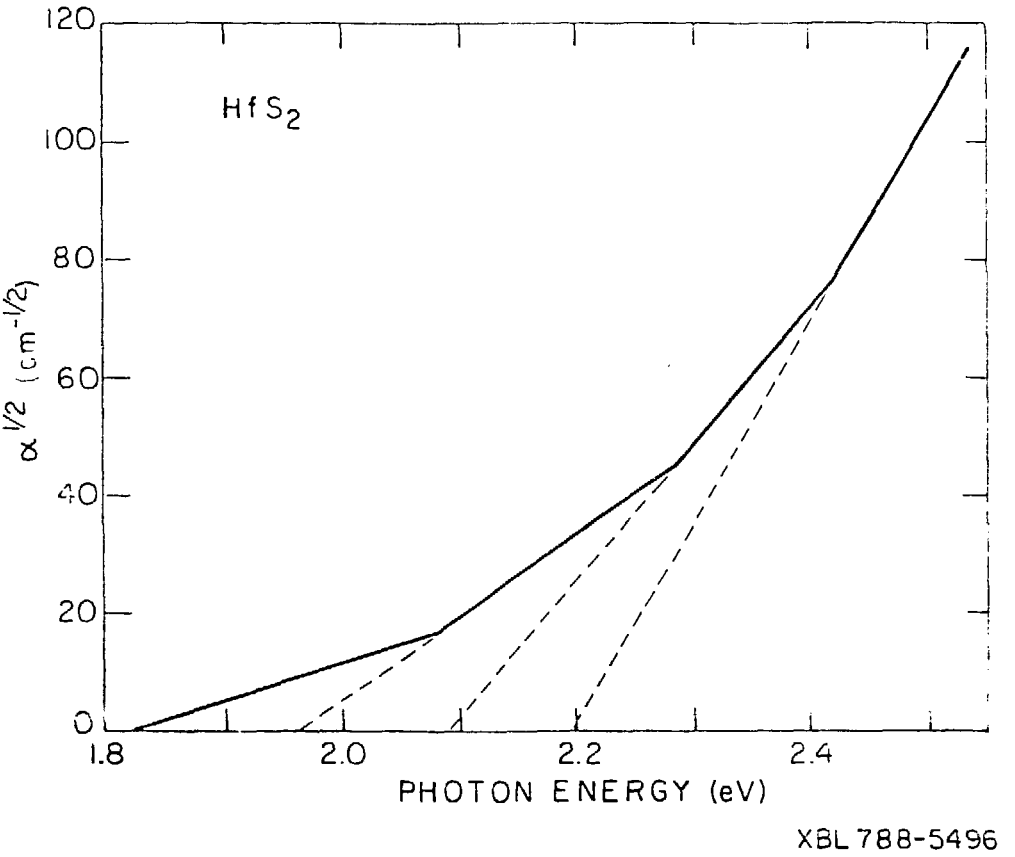
120
100
80
60
40
20
0
HfS_2
$\alpha^{1/2}$ ($cm^{-1/2}$)
1.8
2.0
2.2
2.4
PHOTON ENERGY (eV)
XBL 788-5496

Figure 3

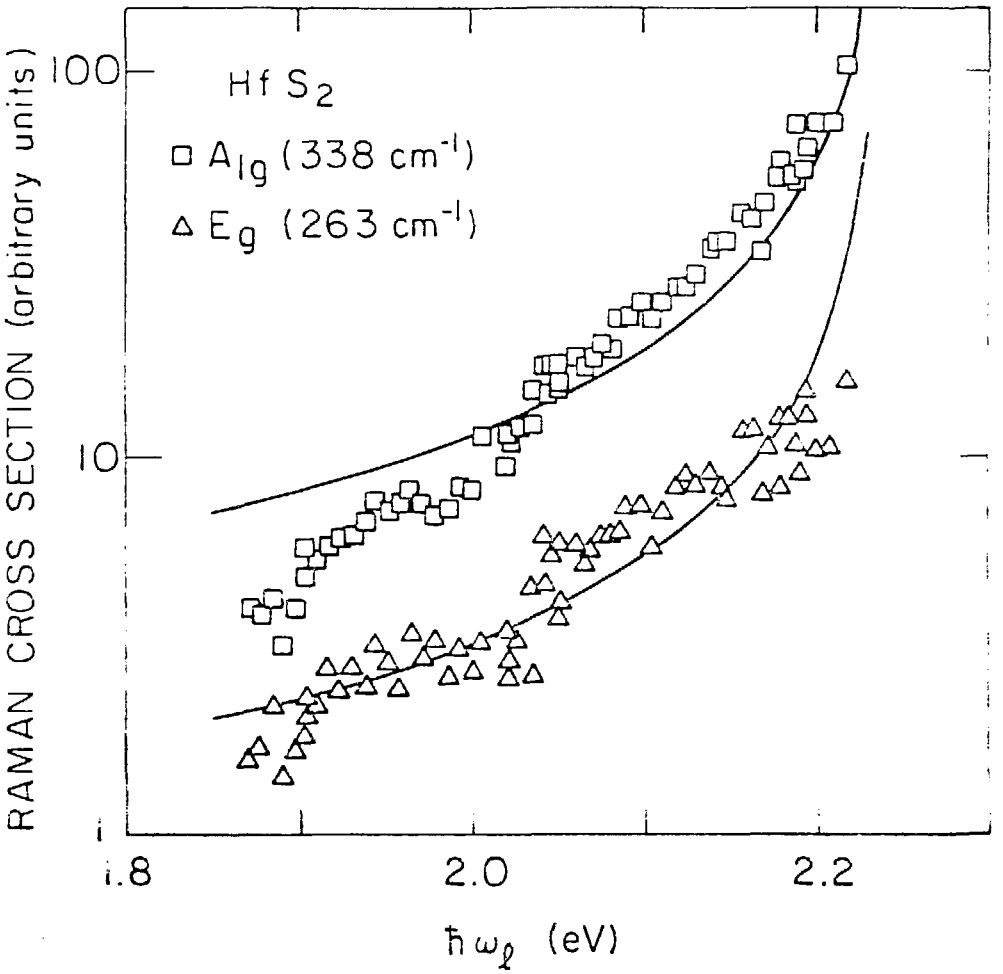

XBL788-5497

IV. Magnon Sidebands of Excitonic Luminescence from Antiferromagnets

A. Introduction

Magnon sidebands associated with excitonic absorption and emission in antiferromagnetic systems have long been a subject of extensive theoretical and experimental studies.[1,2] In particular, the one-magnon sideband of the excitonic transition in the $^6A_{1g}(^6S) - ^4T_{1g}(^4G)$ manifold in MnF_2 has been most thoroughly investigated.[3,4] In absorption, while the discrepancy between theory and experiment in the α- and σ-polarized[5] spectra is small, it is quite large in the π-polarization.[5] The discrepancy presumably results from ignoring the exciton-magnon interaction[6] in the theoretical calculation. In emission, since the exciton and magnon are not simultaneously present, the exciton-magnon interaction does not come into play. Then the theoretical calculation agrees very well with the experimental α- and σ-polarized spectra.[3] However, observation of the π-polarized one-magnon luminescence sideband, although predicted by theory,[2] has never been reported probably because of its much weaker intensity. In the first part of this section, our recent observation[7] of the π-polarized one-magnon sideband will be reported, which is indeed much weaker than those with α- and σ-polarizations. The spectrum can be described almost perfectly by the theory without the exciton-magnon interaction. At higher temperatures, antiStokes luminescence of the sideband has also been observed. The temperature deduced from the Stokes-antiStokes ratio agrees with that obtained from the $E_1 - E_2$ exciton luminescence ratio.

The magnon sideband work has often been limited to one- and two-magnon sidebands. Higher-order magnon sidebands are difficult to observe

because they are either too weak or buried in the background. In the luminescence spectrum, strong background usually arises from impurity emission bands.[8] With pulsed excitation and detection, however, long lived impurity luminescence can be largely suppressed. The second half of this section reports our recent observation[9] of luminescence spectra of up to 7-magnon sidebands in MnF_2 and a few less in $KMnF_3$ and $RbMnF_3$ using such a technique. We interpret the results qualitatively by a simple two-ion local interaction model. Multi-magnon sidebands have earlier been predicted by Bhandari and Falicov from the sudden approximation model.[10] In $KMnF_3$, n-magnon sidebands with $n \leq 3$ have been observed by Strauss et al.,[11] but no theoretical interpretation of the results has been attempted.

B. Background Information and Review

MnF_2, $KMnF_3$, and $RbMnF_3$ have similar excitonic and magnetic properties resulting from Mn^{++} ions. For simplicity, we consider only MnF_2. Relevant differences among these crystals will be pointed out when necessary. Figure 1 shows the crystal structure of MnF_2.[4] The crystal structure is that of rutile and is uniaxial with the $\hat{c}$-axis in the z-direction. Each Mn^{++} ion in the ground state has a nonzero spin ($S = 5/2$) and hence a nonzero magnetic moment. Below the Néel temperature of 68°K, the magnetic moments (or spins) of the Mn^{++} ions become antiferromagnetically ordered via the short range exchange interaction. The ground state of the crystal departs slightly from the perfectly aligned state (Néel state) shown in Fig. 1. A unit deviation of a spin from its equilibrium position in the ground state can propagate in the crystal via mutual exchange; this collective excitation is a spin wave (magnon).[12]

Figure 2 shows schematically the lower energy states of MnF_2 in the various approximations.[4,13,14] The d^5 configuration of an Mn^{++} ion is split into many terms by the Coulomb interaction. The lowest term is ^6S and the first excited term is ^4G which is rougly in the middle of the visible spectrum. All the other terms are much higher in energy and outside our laser tuning range. With the cubic crystal field added on, the ^6S term becomes the $^6A_{1g}$ state and the ^4G term becomes the $^4T_{1g}$ state. Turning on the exchange interaction, spin-orbit interaction, and orthorombic crystal field removes all the degeneracies. Twelve states are obtained from $^4T_{1g}$, though only the lowest two of these states, E_1 and E_2, have been identified experimentally. Six states are obtained from $^6A_{1g}$ in this molecular field approximation. All states discussed have even parity, therefore electric dipole transitions between any two levels are forbidden. Due to wavefunction overlapping in a real crystal, these molecular field states form energy bands in the Brillouin zone of the crystal. Thus, E_1 and E_2 states form the E_1 and E_2 Frenkel exciton bands, respectively. In the limit of low excitation, the ground manifold $^6A_{1g}$ can be treated very well in the spin-wave approximation. We then have a magnon branch above the true ground state in the Brillouin zone. At higher excitation levels, the magnon-magnon interaction has to be taken into account.[12,15] The exciton and magnon band structures are shown schematically in the inset of Fig. 3. The E_2 exciton has an energy of 18435 cm^{-1} (5424 Å) at the zone center and a small negative dispersion[16] toward the zone boundary. The E_1 exciton has an energy of 18418 cm^{-1} (5429 Å) and is nearly dispersionless. The magnon dispersion has been determined by inelastic neutron scattering.[17] It has an energy of 8.7 cm^{-1} at the zone center and a maximum energy of 55 cm^{-1} at the zone boundary.

The optical processes we are interested in can be described clearly in equation forms. For excitonic absorption and its magnon sideband, we have

$$\hbar\omega \rightarrow E_{1,2}(\vec{k} = 0) \tag{1}$$

$$\hbar\omega \rightarrow E_{1,2}(\vec{k}) + M(-\vec{k}) \tag{2}$$

respectively, where $\hbar\omega$ is the energy of the absorbed photon, $E_{1,2}(\vec{k})$ an E_1 or E_2 exciton with crystal momentum $\vec{k}$, and $M(\vec{k})$ a magnon with crystal momentum $\vec{k}$. A visible photon has essentially zero momentum, therefore momentum as well as energy is conserved in Eqs. (1) and (2). While the whole Brillouin zone contributes to the magnon sideband processes, only the zone center excitons are involved in the excitonic processes.

The experimentally observed transmission curves[4] of MnF_2 at ~ 2°K are shown in Fig. 3. The sharp lines E_1 and E_2 are the excitonic absorption lines described by Eq. (1). The broad bands $\sigma_1(\pi_1)$ and σ_2 are the magnon sidebands of the E_1 and E_2 excitons in the $\sigma(\pi)$-polarization respectively, as described by Eq. (2). From the polarization dependence, the excitonic absorption and its magnon sideband can be shown to be due to magnetic dipole and electric dipole transitions respectively. Therefore, the sideband absorption, though second order in nature, are actually more intense than the first order excitonic absorption. The widths of the E_1 and E_2 lines are typically about half a wavenumber and are sample dependent probably due to strain induced inhomogenous broadening. The widths of the magnon sidebands are determined by the dispersion of the excitons and magnons by virtue of Eq. (2). The detailed sideband shapes

are determined by the transition matrix elements and the density of states. Since the exciton and the magnon are generated simultaneously at close proximity in a sideband absorption process, the exciton-magnon interaction should affect the sideband positions.[6]

Similarly, for the excitonic luminescence and associated magnon sidebands, we have

$$E_{1,2}(\vec{k} = 0) \rightarrow \hbar\omega \tag{3}$$

$$E_{1,2}(\vec{k}) \rightarrow \hbar\omega + M(\vec{k}) \tag{4}$$

$$E_{1,2}(\vec{k}) + M(-\vec{k}) \rightarrow \hbar\omega \tag{5}$$

where Eq. (3) is the magnetic dipole direct exciton recombination process, and Eqs. (4) and (5) are the electric dipole Stokes and antiStokes magnon sideband processes respectively. The antiStokes sideband luminescence process described by Eq. (5) depends on the thermal population of the magnons, otherwise it is just the inverse process of magnon sideband absorption described by Eq. (2). On the other hand, the Stokes sideband luminescence process described by Eq. (4) is not related in a simple way to the antiStokes process. In particular, since the exciton and magnon involved in the process are never simultaneously present, the exciton-magnon interaction does not come into the picture.

The higher order luminescence sidebands are also possible, e.g.

$$E_1(\vec{k}) \rightarrow \hbar\omega + \sum_{i=1}^{n} M(\vec{k}_i) \tag{6}$$

with

$$\sum_{i=1}^{n} \vec{k}i = \vec{k}$$

This is the n-magnon luminescence sideband of the E_1 exciton.

Processes described by Eqs. (3), (4), (5), and (6) are our subjects of investigation.

C. Experimental Description

The MnF_2 samples used were grown by the zone refining technique. The methods of growth for the $KMnF_3$ and $RbMnF_3$ samples were unknown. All samples were x-ray oriented to within 1° and cut into the form of a parallelpiped with the conventional x, y, and z axes of the crystals along the edges. The relevant surfaces were polished to an optical finish. Samples were cooled by either superfluid helium or cold helium exchange gas. Temperature was measured by helium vapor pressure or by a thermocouple attached to the copper substrate. The polaroid used for analyzing the luminescence signal was mounted inside the helium Dewar to avoid depolarization effect introduced by the Dewar windows. 90° or backward scattering geometries were used.

Two exciton-detection techniques were used:

(i) CW excitation-detection

The Raman setup described in Section II was used. The 5145 Å output of an Ar^+ laser was used for excitation. Luminescence from a sample was analyzed by a double monochromator and detected by standard photon counting electronics and a multichannel analyzer. The laser light was focusd into the sample with a beam diameter of ~ 50 μ and typical power of 100

mW. Same spectra were obtained at different excitation levels and local heating effect was undetectable under our experimental conditions. Spectra taken with this technique were in general troubled by strong impurity luminescence.

(ii) Pulsed excitation-detection

A tunable flash-pumped dye laser was used as the excitation source. The laser pulses had a pulsewidth of 0.4 μsec and an energy of a few millijoules per pulse. Luminescence from a sample was analyzed by a double monochromator followed by a high gain RCA 7265 photomultiplier and a gated PAR-162 boxcar integrator. Part of the laser beam was used to trigger two independent fast PIN photodiodes (IR-7016L from Infrared Industries, Inc.). One of them with high gain circuit was used for reliable triggering of the boxcar gate; the other with linear gain circuit was connected to the second channel of the boxcar for signal normalization over the laser power. The boxcar gate had an adjustable width (1-20 μsec) and its opening was delayed by 1 μsec after the leading edge of the laser pulse to eliminate possible pickup.

Figure 4 shows schematically the timing sequence of the events. The impurity luminescence lifetimes ($>$ 1 msec) were much longer than the intrinsic luminescence lifetime ($<$ 200 μsec). We could eliminate most of the impurity luminescence while retaining most of the intrinsic luminescence by chosing a suitable gate width ($\leq$ 20 μsec). The laser pulse repetition rate was also kept low ($\leq$ 6 pps) in order to suppress the exceptionally long-lived impurity lines. Then the spectrum obtained was believed to be essentially intrinsic. This is supported by the following experimental observations. (1) With increasing gate width, impurity luminescence lines showed up with increasing strength. (2) For different

samples with different impurity luminescence, the intrinsic luminescence spectrum was the same. (3) The intrinsic luminescence at low excitation intensity normalized by photons absorbed was independent of the exciting laser wavelength λ_ℓ, while the impurity luminescence intensity changed rapidly with varying λ_ℓ. (4) Intrinsic luminescence depended strongly on the excitation intensity. In MnF_2 for example, the intrinsic luminescence lifetime decreased from ~ 200 μsec at low excitation intensities to ~ 5 μsec at ~ 50 MW/cm^2. At high excitation intensities, the luminescence decay became more and more non-exponential with a very steep initial slope (presumably due to exciton-exciton collisions), and the luminescence intensity was no longer proportional to the excitation intensity.

D. One-Magnon Luminescence Sidebands of MnF_2

(i) Experimental results

Typical polarized intrinsic luminescence spectra of MnF_2 obtained with the pulsed excitation-detection scheme are shown in Fig. 5. The observed exciton lines E_1 and E_2 in the $^4T_{1g} \rightarrow {}^6A_{1g}$ transitions and the σ, σ-polarized one-magnon sidebands σ_1 associated with E_1 agree well with those reported in the literature.[3] The corresponding π-polarized one-magnon sideband π_1 is appreciably weaker and broader. At relatively higher temperatures, the antiStokes sideband emission is also clearly visible, and is relatively more intense for the π-polarization. In order to determine the sideband lineshape more accurately, we have also recorded the luminescence spectrum with the CW excitation-detection scheme. The result for the π-polarization is shown in Fig. 6, where in (a) the spectrum was obtained with the sample immersed in superfluid helium, and in (b) the spectrum was obtained with the sample in cold helium gas at 13°K. A

strong impurity luminescence line is clearly present on the low-energy side of the sideband in Fig. 6(a), while the same line is apparently thermally quenched in Fig. 6(b).

(ii) Theory

To explain the observed sidebands, we use the theory of Loudon.[2] In his formalism, two-ion local exchange interaction is responsible for the magnon creation or annihilation and the exciton-magnon interaction is neglected. The interaction Hamiltonian is given by

$$H' = \left\{ \sum_{<ii'>}^{n} \vec{\pi}_{ii'} a_i^+ S_{i'}^+ + \sum_{<ij>}^{nn} \vec{\pi}_{ij} a_i^+ S_j^+ + \sum_{<jj'>}^{n} \vec{\pi}_{jj'} a_j^+ S_{j'}^- + \sum_{<ji>}^{nn} \vec{\pi}_{ji} a_j^+ S_i^- + \text{complex conjugate} \right\} \cdot \vec{E} \qquad (7)$$

where a^+ is the exciton creation operator, S^+ and S^- the spin raising and spin lowering operators respectively, $\vec{\pi}$'s the generalized dipole matrix elements, $\vec{E}$ the electric field of the light wave, i(i') and j(j') the Mn^{++} ions on the spin-up and spin-down sublattices respectively, the first term being summed over all nearest neighbor pairs (n) on the spin-up sublattice and the second term being summed over all next-nearest neighbor pairs (nn) on opposite sublattices, etc. The $\vec{\pi}$'s can not be calculated in practice and are regarded as parameters. The number of independent components of the $\vec{\pi}$'s can be reduced by symmetry arguments. The local operators for the excitons and spins can also be transformed to wave operators. The resultant Hamiltonian is then used to calculate the sideband shapes by the Fermi golden rule.

If only the interaction between next-nearest neighbors on the opposite sublattice is taken into account, then the one-magnon sideband ab-

sorption $A^{nn}(\omega)$ and emission $E^{nn}(\omega)$ in the α- or σ-polarization are given, in the zero-temperature approximation, by

$$\begin{Bmatrix} A^{nn}_{\alpha,\sigma}(\omega) \\ E^{nn}_{\alpha,\sigma}(\omega) \end{Bmatrix} = \sum_{\vec{k}} \left[C^2 \cos^2\left(\frac{k_x a}{2}\right)\cos^2\left(\frac{k_y a}{2}\right) + D^2 \sin^2\left(\frac{k_x a}{2}\right)\sin^2\left(\frac{k_y a}{2}\right)\right] \sin^2\left(\frac{k_z c}{2}\right) \begin{Bmatrix} u_k^2 \\ v_k^2 \end{Bmatrix} \delta[\hbar\omega - \varepsilon_0 \mp \varepsilon_m(\vec{k})] \tag{8}$$

and those in the π-polarization by

$$\begin{Bmatrix} A^{nn}_{\pi}(\omega) \\ E^{nn}_{\pi}(\omega) \end{Bmatrix} = F^2 \sum_{\vec{k}} \left[\sin^2\left(\frac{k_x a}{2}\right)\cos^2\left(\frac{k_y a}{2}\right) + \cos^2\left(\frac{k_x a}{2}\right)\sin^2\left(\frac{k_y a}{2}\right)\right] \cos^2\left(\frac{k_z c}{2}\right) \begin{Bmatrix} u_k^2 \\ v_k^2 \end{Bmatrix} \delta[\hbar\omega - \varepsilon_0 \mp \varepsilon_m(\vec{k})] \tag{9}$$

where C, D, and F are coupling constants of the same order of magnitude, a and c are lattice constants, ε_0 is the E_1 exciton energy, $\varepsilon_m(\vec{k})$ is the magnon energy at $\vec{k}$, and u_k and v_k are defined in Ref. 2 and reproduced here in Fig. 7. Similarly, one finds that the interaction between nearest neighbors on the same sublattice contributes to the sideband absorption and emission in the α- or σ-polarization as

$$\begin{Bmatrix} A^{n}_{\alpha,\sigma}(\omega) \\ E^{n}_{\alpha,\sigma}(\omega) \end{Bmatrix} = G^2 \sum_{\vec{k}} \sin^2(k_z c) \begin{Bmatrix} v_k^2 \\ u_k^2 \end{Bmatrix} \delta[\hbar\omega - \varepsilon_0 \mp \varepsilon_m(\vec{k})] \tag{10}$$

but contributes nothing to the sideband absorption and emission in the π-polarization, where G is again a coupling constant of the same order of magnitude as C, D, and F.

The summations over $\vec{k}$ in the above equations are weighted heavily towards the Brillouin zone edges by the large magnon density of states. However, near the zone edges, v_k^2 tends to zero while u_k^2 remains finite as shown in Fig. 7. It is then easy to see that

$$A_{\sigma,\alpha}(\omega) \cong A^{nn}_{\sigma,\alpha}(\omega) + A^{n}_{\sigma,\alpha}(\omega) \cong A^{nn}_{\sigma,\alpha}(\omega); \tag{11}$$

$$E_{\sigma,\alpha}(\omega) \cong E^{nn}_{\sigma,\alpha}(\omega) + E^{n}_{\sigma,\alpha}(\omega) \cong E^{n}_{\sigma,\alpha}(\omega); \tag{12}$$

$$E_{\pi}(\omega) \cong E^{nn}_{\pi}(\omega) \quad ; \quad A_{\pi}(\omega) \cong A^{nn}_{\pi}(\omega) \tag{13}$$

and $E_{\pi}(\omega) \ll A_{\pi}(\omega)$, $A_{\sigma,\alpha}(\omega)$, $E_{\sigma,\alpha}(\omega)$.

Dietz et al.[5] has used Eq. (10) to fit quantitatively the observed one-magnon luminescence sideband in the α,σ-polarization. Similarly, we can use Eq. (9) to fit the luminescence sideband in the π-polarization. Figure 6(a) shows that the agreement between theory and experiment is indeed excellent. In the inset of Fig. 6, we also show the comparison between theory and experiment on the π-polarized one-magnon absorption sideband. The discrepancy is obvious. Agreement in the luminescence case and disagreement in the absorption case clearly indicates that the exciton-magnon interaction is non-negligible in the absorption process. This interaction should appreciably broaden the sideband absorption and shift it to lower energy.[6] We notice that because of the difference in u_k^2 and v_k^2 associated with the sine and cosine terms in Eq. (9), the theoretical lineshapes of the π-polarized absorption and emission sidebands are very different. Also, the integrated strength ratio of absorption to emission is about 23.

We realize from Eqs. (2) and (5) that the antiStokes sideband emission is simply the inverse process of the sideband absorption only if the thermal population of magnons is properly taken into account. Therefore, we can expect to obtain the antiStokes sideband spectrum by simply multiplying the experimental absorption sideband, normalized to yield the correct sideband absorption-to-Stokes-emission ratio of 23, by a Bose-Einstein distribution function at a proper temperature. This is shown in Fig. 6(b). The theoretical antiStokes spectrum corresponding to a temperature of 13.3°K fits very well with the observed spectrum. This temperature is in good agreement with the one deduced from the luminescence intensity ratio of the E_1 and E_2 exciton lines.[18] In the σ- and σ-polarizations, deduction of the effective temperature from the antiStokes sideband emission is not possible because of lack of a normalization constant relating the strengths of the absorption and Stokes emission sidebands.

(iii) Conclusion

We have shown that the theory of Loudon gives an excellent description of the observed π-polarized one-magnon luminescence sideband in MnF_2. The effective temperature of the crystal can be deduced from the simultaneously observed π-polarized antiStokes luminescence sideband.

E. Multi-Magnon Luminescence Sidebands of MnF_2, $KMnF_3$, and $RbMnF_3$

(i) Experimental results

Figure 8 shows in an extended region the typical polarized luminescence spectra of MnF_2 obtained with the pulsed excitation-detection scheme. The impurity luminescence in this case was suppressed to an undetectable level. The exciton lines E_1, E_2 and the one-magnon sidebands

σ_1, π_1 and the antiStokes one-magnon sidebands have been discussed in Part D. Figure 8 also shows a series of luminescence peaks at lower energies. They form a more or less regular progression. Neighboring peaks are separated by ~ 55 cm^{-1} which is the maximum magnon frequency in MnF_2.[17] They are therefore identified as the multi-magnon sidebands. Arrows in Fig. 8 indicate where the cutoff frequencies of the multi-magnon sidebands should be. The polarization properties suggest that these sidebands are of electric-dipole origin. The π-polarization spectrum is however significantly different from the σ- and α-polarization spectra. With increasing temperature, the multi-magnon sidebands as well as the one-magnon sidebands gradually smeared out into the background as they should. As shown in Fig. 8, up to 7-magnon sidebands were actually observed in MnF_2. Higher-order magnon sidebands might exist, but our spectra were terminated by the difficulty of positively identifying small structure on the rising background. Phonon-assisted optical transitions are presumably responsible for this strong luminescence background.

We have observed similar multi-magnon sidebands in the luminescence spectra of $KMnF_3$ and $RbMnF_3$ as shown in Fig. 9. In $KMnF_3$, sidebands up to 5 magnons show up clearly. They are regularly spaced with a frequency separation close to the maximum magnon frequency[19] of 76.3 cm^{-1}. In $RbMnF_3$, the E_2 exciton line is too weak to be observed. Also, under our experimental conditions, two impurity lines at 5493 Å and 5517 Å still remained visible although they were greatly reduced in strength. As shown in Fig. 9, we have observed up to 3-magnon sidebands associated with E_1 in $RbMnF_3$. They are almost regularly spaced by the maximum magnon frequency[20] of 71 cm^{-1}. Interesting enough, we have also observed an almost identical series of magnon sidebands associated with the im-

purity exciton at 5493 Å. This strongly suggests the localized nature of the phenomenon.

(ii) Theory

We now concentrate our theoretical interpretation of the results on MnF_2. The discussion is equally applicable to $KMnF_3$ and $RbMnF_3$. The n-magnon luminescence sideband processes are represented mathematically by Eq. (6). From the perturbation point of view, such a process would appear to be of higher order as the number of magnons n increases. This is certainly not true for the observed multi-magnon sidebands since the luminescence peaks in Fig. 6 are generally of comparable magnitude. We can however qualitatively explain the results by the following two-ion local interaction model.

Instead of using the band picture shown in the inset of Fig. 3, we use the states in the molecular field approximation shown in Fig. 2. Figure 10 shows the energy level diagrams of three neighboring Mn ions;[4] A and B are nearest neighbors on the same sublattice while A and C are second nearest neighbors on the opposite sublattices. The ground states $\langle g, m_s|$ of each ion are split by the exchange field into a Zeeman sublevels denoted by the spin quantum number $m_s = \pm 5/2, \pm 3/2$, and $\pm 1/2$. The excited state E_1 is a mixed state $\sum_{m_s'} a_{m_s'} \langle e, m_s'|$ with $m_s' = \pm 1/2, \pm 3/2$, although $\langle e, m_s' = 3/2|$ or $\langle e, m_s' = -3/2|$ may dominate. In addition to the exchange field, there is also the off-diagonal exchange interaction[21] $J_{ij} S_i^{\pm} S_j^{\mp}$ between ion pairs. We shall treat it as a perturbation. Then, if the Mn ion A is initially excited, the one-magnon sideband emission results from an allowed electronic transition $\langle e, m_s'|_A \rightarrow \langle e', 3/2|_A$ followed by an exchange spin-flip transition between A and B, $\langle e', 3/2|_A \langle g, 5/2|_B \rightarrow \langle g, 5/2|_A \langle g, 3/2|_B$, or from the exchange spin-flip $\langle e, m_s'|_A$

$\langle g,5/2|_B \rightarrow \langle e',5/2|_A \langle g,3/2|_B$ followed by the allowed transition $\langle e',5/2|_A \rightarrow \langle g,5/2|_A$. Either process involves $\Delta m_s = 1$ corresponding to the emission of one magnon. Now, similar physical processes of the same perturbation order can give rise to the n-magnon sidebands with $n \leq 6$. For example, $\langle e,m_s'|_A \rightarrow \langle e',3/2|_A$ followed by $\langle e',3/2|_A \langle g,-5/2|_C \rightarrow \langle g,1/2|_A \langle g,-3/2|_C$ via $J_{AC} S_A^- S_C^+$ leads to a 3-magnon sideband which can have comparable strength to the one-magnon sideband. Experimentally, the π-polarization spectrum in Fig. 8 even shows a 3-magnon sideband stronger than the one-magnon sideband. In a similar manner, the 2-magnon sideband can be explained by $\langle e,m_s'|_A \rightarrow \langle e',1/2|_A$ followed by $\langle e',1/2|_A \langle g,5/2|_B \rightarrow \langle g,3/2|_A \langle g,3/2|_B$ and others; the 4-magnon sideband can be explained by $\langle e,m_s'|_A \rightarrow \langle e',1/2|_A$ followed by $\langle e',1/2|_A \langle g,-5/2|_C \rightarrow \langle g,-1/2|_A \langle g,-3/2|_C$ and others; etc.

In this model with $J_{ij} S_i^{\pm} S_j^{\mp}$ treated as a perturbation, the n-magnon sidebands with $n > 6$ will have to arise from a higher-order process utilizing $J_{ij} S_i^{\pm} S_j^{\mp}$ more than once. Strictly speaking, we should treat the exchange interaction as a strong coupling Hamiltonian and solve the eigenenergies and eigenstates for a cluster of neighboring Mn ions. If the spin part is isolated from the orbital part, then this is just the sudden approximation model proposed by Bhandari and Falicov.[10] In such a model, all the multi-magnon sidebands are treated on the same footing.

It is not easy to be quantitative in the above discussion. A realistic calculation taking into account just the nearest and next-nearest neighbor interactions is already extremely difficult. In addition, the relative amount of m_s' spin mixture in the excited state is not known so that the relative strengths of the magnon sidebands cannot be estimated. The magnon dispersion which results from exchange interaction between

many ion pairs over a distance is not included in our model, and hence the spectral lineshape of these sidebands cannot be calculated. Nevertheless, the model does give a correct qualitative interpretation of the results. In particular, it explains how several multi-magnon luminescence sidebands can exist with comparable strengths. Our model treating the exchange interaction as a perturbation will predict in the first-order approximation only a one-magnon sideband in the absorption spectrum. It therefore also explains why n-magnon sidebands with $n > 2$ has never been observed.

(iii) Conclusion

We have observed multi-magnon luminescence sidebands in antiferromagnetic MnF_2, $KMnF_3$, and $RbMnF_3$. We have shown that a simple model based on two-ion local exchange can explain qualitatively the observed results. A quantitative analysis is not yet available.

References

1. D. D. Sell, J. Appl. Phys. 39, 1030 (1968).
2. R. Loudon, Advan. Phys. 17, 243 (1968).
3. R. E. Dietz, A. E. Meixner, H. J. Guggenheim, and A. Misetich, J. Luminesc. 1, 2, 279 (1970).
4. D. D. Sell, R. L. Greene, and R. M. White, Phys. Rev. 158, 489 (1967).
5. Conventional notations σ, α, and π are used to denote the three polarization geometries ($\vec{E} \perp \hat{c}$, $\vec{k} \perp \hat{c}$), ($\vec{E} \perp \hat{c}$, $\vec{k} \parallel \hat{c}$), and ($\vec{E} \parallel \hat{c}$, $\vec{k} \perp \hat{c}$) respectively. For a uniaxial crystal, spectra in all three polarization geometries are needed in order to determine whether a transition is electric dipole or magnetic dipole in origin.
6. Y. Tanabe, K-i. Gondaira, and H. Murata, J. Phys. Soc. Japan 25, 1562 (1968).
7. T. C. Chiang, P. R. Salvi, J. Davies, and Y. R. Shen, Solid State Commun., to be published (1978).
8. R. L. Greene, D. D. Sell, R. S. Feigelson, G. F. Imbusch, and H. J. Guggenheim, Phys. Rev. 171, 600 (1968).
9. T. C. Chiang, P. R. Salvi, J. Davies, and Y. R. Shen, Solid State Commun., to be published (1978).
10. R. Bhandari and L. M. Falicov, J. Phys. C : Solid St. Phys. 5, 1445 (1972).
11. E. Strauss, V. Gerhardt, and H. Riederer, J. Luminesc. 12, 13, 239 (1976).
12. See, for example, C. Kittel, Quantum Theory of Solids.
13. R. S. Meltzer and L. L. Lohr, Jr., J. Chem. Phys. 49, 541 (1968).
14. A. M. Clogston, J. Phys. Chem. Solids, 7, 201 (1958).

15. R. J. Elliott, M. F. Thorpe, G. F. Imbusch, R. Loudon, and J. B. Parkinson, Phys. Rev. Lett. 21, 147 (1968).

16. N. M. Amer, T. C. Chiang, and Y. R. Shen, Phys. Rev. Lett. 34, 1454 (1975); 36, 1102 (1976).

17. A. Okazaki, K. C. Tuberfield, and R. W. H. Stevenson, Phys. Lett. 8, 9 (1964).

18. The luminescence intensity ratio of E_2 to E_1 is given by $e^{-\Delta/kt}(f_2/f_1)$, where Δ is the energy separation between E_2 and E_1 excitons, and f_2 and f_1 the oscillator strengths of the E_2 and E_1 excitons, respectively.

19. C. G. Windsor and R. W. H. Stevenson, Proc. Phys. Soc. 87, 501 (1966).

20. S. J. Pickart, M. F. Collins, and C. G. Windsor, J. Appl. Phys. 37, 1054 (1966).

21. K-I. Gondaira and Y. Tanabe, J. Phys. Soc. Japan 21, 1527 (1966).

Figure Captions

Fig. 1 Crystal structure of MnF_2. The dashed lines outline the chemical and magnetic unit cell. Mn^{++} ions numbered 1, 2, and 3 are the first, second, and third nearest neighbors of the central Mn^{++} ion in the cell. Arrows indicate the direction of the spins of the Mn^{++} ions in the Néel state.

Fig. 2 Schematic representation of the lower energy states of MnF_2 in the various approximations. See text for details.

Fig. 3 Absorption spectrum of MnF_2 at 1.6°K between 18400 and 18500 cm^{-1}. The solid and the dashed curves are for the σ- and π-polarizations respectively. The inset is a sketch of the relevant energy levels.

Fig. 4 Schematic timing sequence of the events in the pulsed excitation-detection scheme. The total integrated impurity luminescence is much greater than the total integrated intrinsic luminescence. However, the intrinsic luminescence is much greater than the impurity luminescence during the boxcar gate open time.

Fig. 5 Polarized intrinsic luminescence spectra of MnF_2 obtained by the pulsed excitation-detection scheme. The laser excitation had a wavelength of 5200 Å, a pulsewidth of 0.4 μsec, a peak power of ~ 30 MW/cm^2 for the π-polarization and ~ 20 MW/cm^2 for the α- and σ-polarizations, and a repetition rate of 6 pps. The boxcar used for detection had a gate width of 1 μsec. The sample was immersed in superfluid helium but laser heating was still apparent. The effective sample temperature was 12°K for the α- and σ-polarizations and 13.8°K

for the π-polarization.

Fig. 6 π-polarized CW luminescence spectra of MnF_2 obtained with a 92 mW, 5145 Å, Ar^+ laser light: (a) with the sample immersed in superfluid He, and (b) with the sample at 13°K. The spectrum in (b) is amplified by 10 relative to that in (a). Solid lines are theoretical curves with the background taken into account. The inset shows the comparison between theoretical and experimental absorption sideband spectra.

Fig. 7 u_k^2 and v_k^2 as functions of k in the Brillouin zone.

Fig. 8 Polarized intrinsic luminescence spectra of MnF_2. Laser intensity was ~ 20 MW/cm^2 for the α- and σ-polarizations and ~ 30 MW/cm^2 for the π-polarization; laser wavelength λ_ℓ = 5200 Å; laser repetition rate = 6 pps; boxcar gate width = 1 μsec. Arrows indicate the theoretical cutoff points of the multi-magnon sidebands as explained in the text.

Fig. 9 (a) Unpolarized intrinsic luminescence spectrum of $KMnF_3$ obtained with laser wavelength λ_ℓ = 5130 Å, boxcar gate width = 10 μsec, laser repetition rate = 6 pps, and laser intensity = 4 MW/cm^2. Arrows indicate the theoretical cutoff points of the multi-magnon sidebands.

(b) Unpolarized luminescence spectrum of $RbMnF_3$ obtained with λ_ℓ = 5230 Å, boxcar gate width = 1 μsec, laser repetition rate = 4 pps, and laser intensity = 60 MW/cm^2. Features marked I are due to impurities. Long arrows indicate the intrinsic multi-magnon progression, while short arrows indicate the extrinsic multi-magnon progression starting from the impurity exciton at 5492.7 Å.

Fig. 10 Energy level diagrams of three neighboring Mn ions in the molecular field approximation. Ions A and B are on the same sublattice; the associated E_1 exciton state $\langle e,m_s'|$ may have a dominant $m_2' = 3/2$ component. Ion C is on the opposite sublattice; the associated E_1 exciton state $\langle e,m_s'|$ may have a dominant $m_s' = -3/2$ component. Transtions between $\langle e,m_s'|$ and $\langle g,m_s|$ are magnetic-dipole allowed and electric-dipole forbidden.

Figure 1

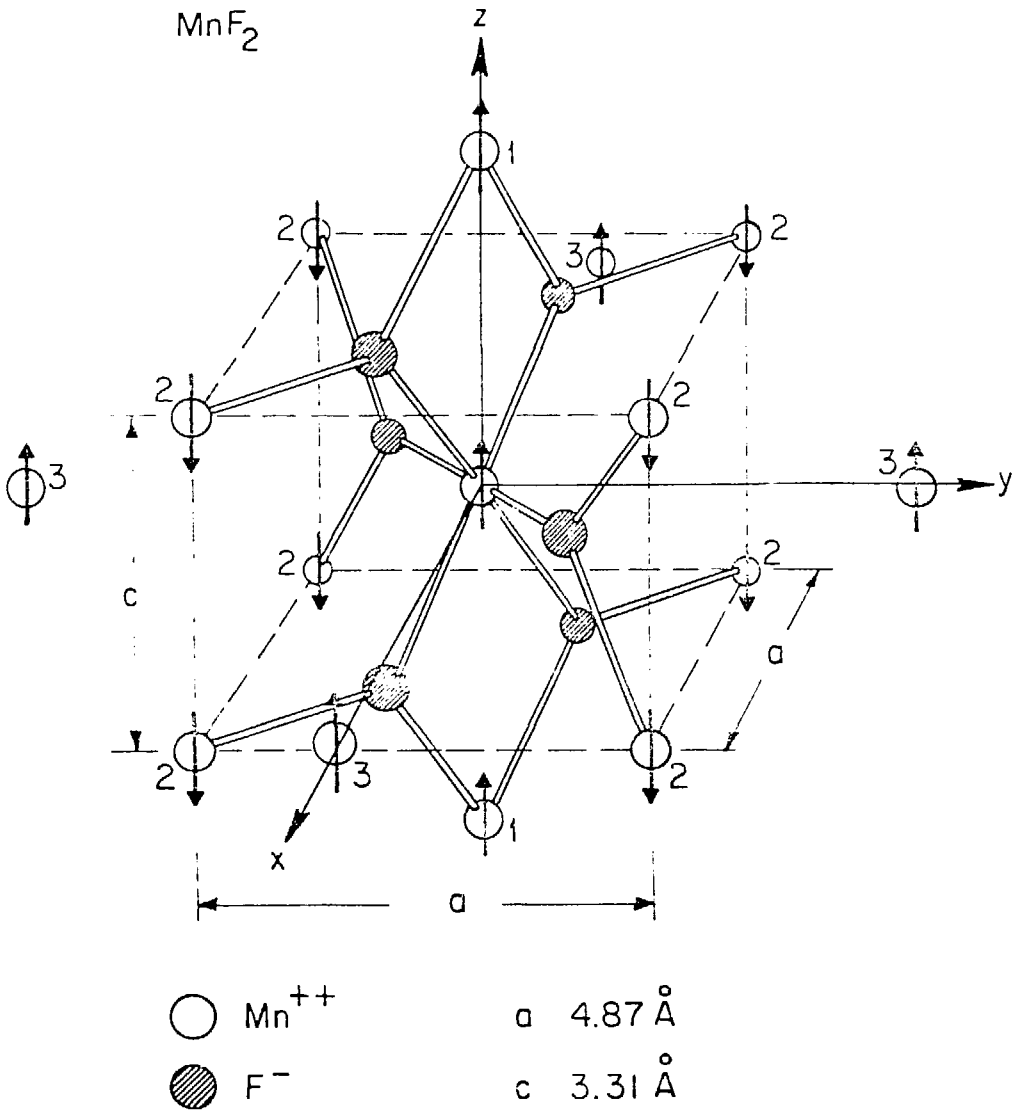

Figure 2

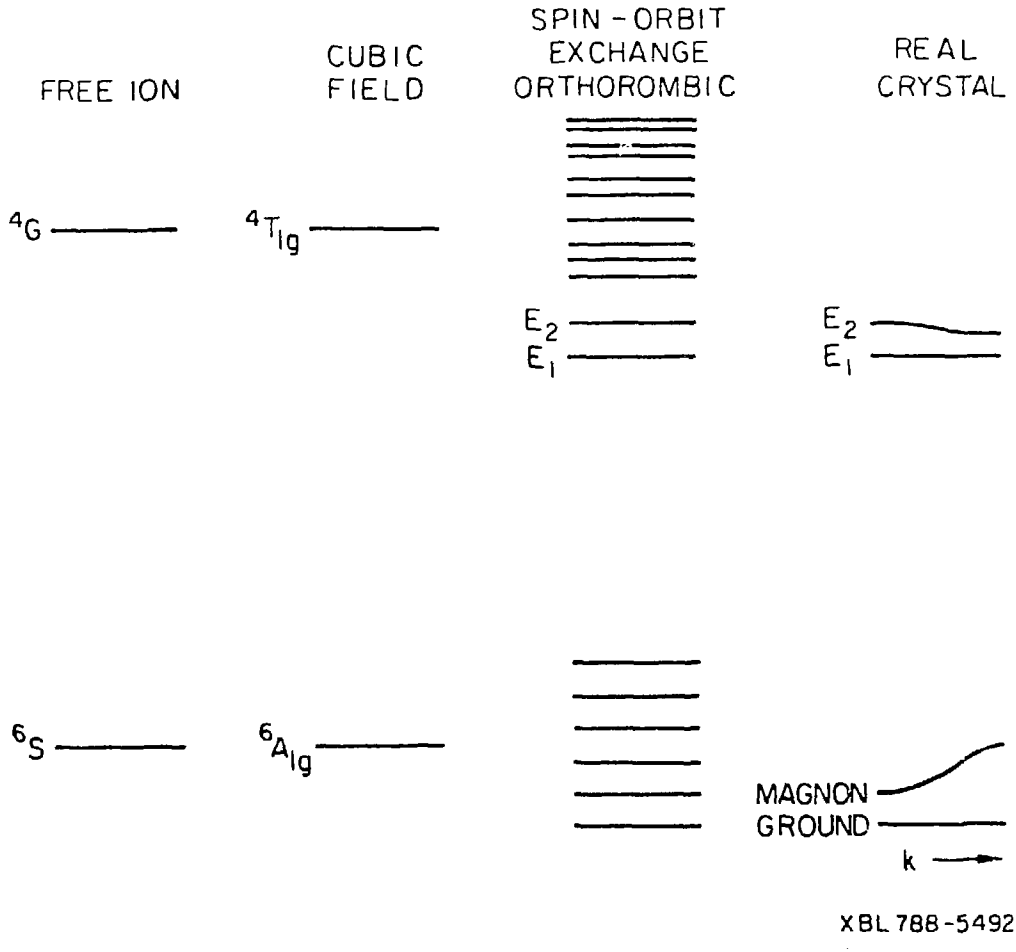
FREE ION
CUBIC FIELD
SPIN - ORBIT EXCHANGE ORTHOROMBIC
REAL CRYSTAL
^4G
$^4T_{1g}$
E_2
E_1
E_2
E_1
^6S
$^6A_{1g}$
MAGNON
GROUND
k
XBL 788-5492

Figure 3

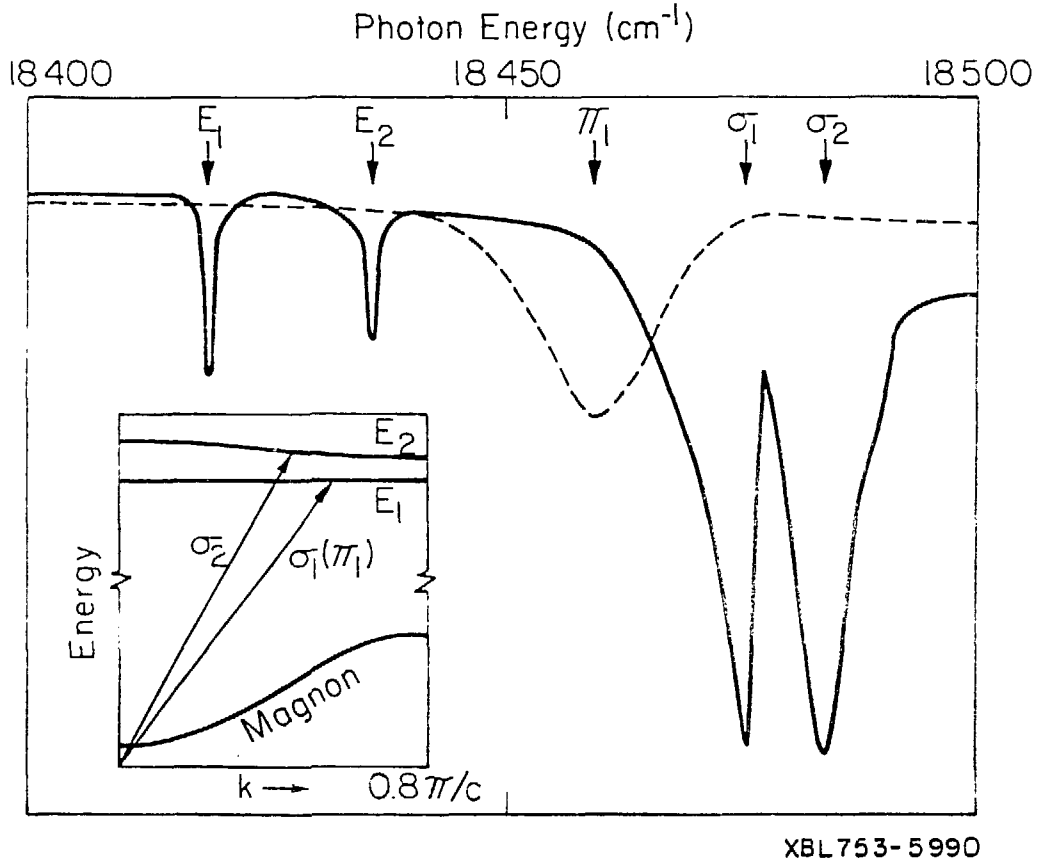
Photon Energy (cm-1)
18400
18450
18500
E1
E2
π1
σ1
σ2
E2
E1
σ2
σ1(π1)
Energy
Magnon
k →
0.8π/c
XBL753-5990

Figure 4

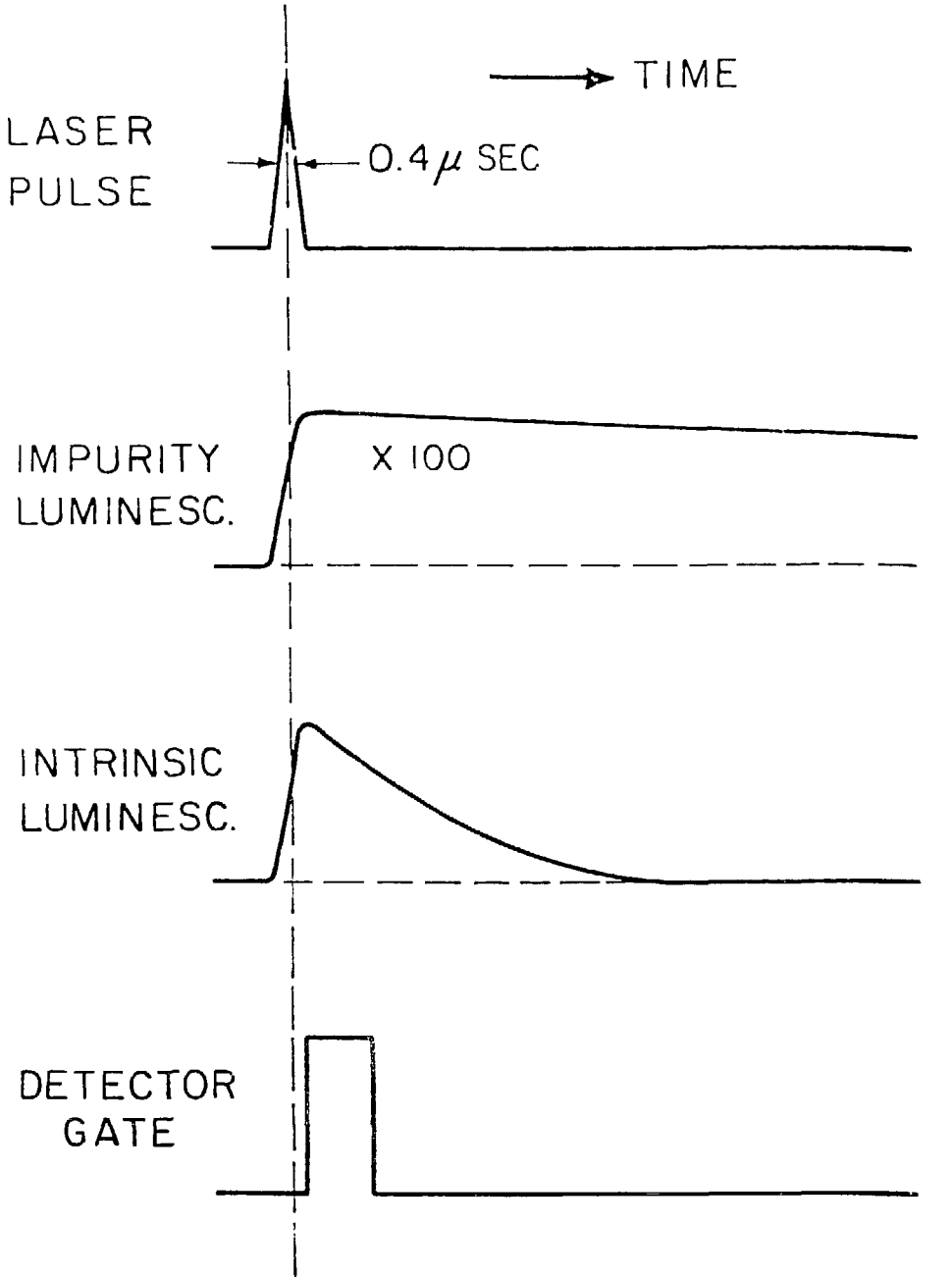
TIME
LASER
PULSE
0.4 μ SEC
IMPURITY
LUMINESC.
X 100
INTRINSIC
LUMINESC.
DETECTOR
GATE
XBL 788-5490

Figure 5

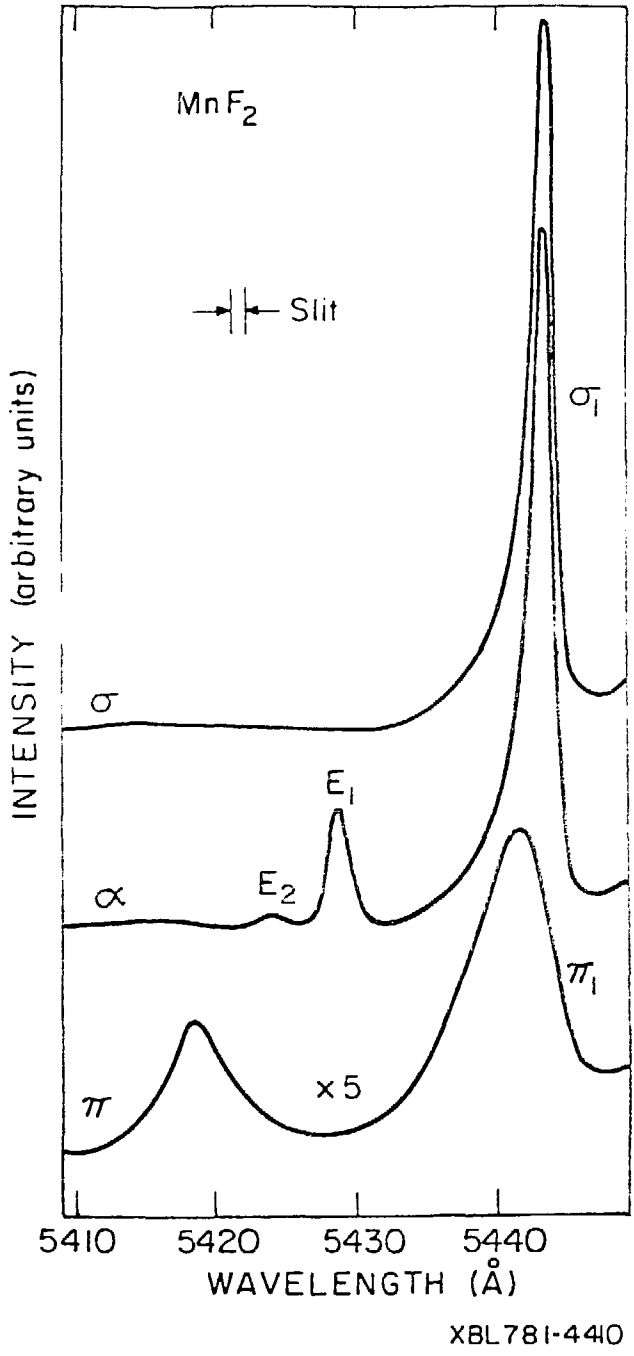
MnF2
Slit
σ1
σ
E1
α
E2
π1
π
x5
INTENSITY (arbitrary units)
5410
5420
5430
5440
WAVELENGTH (Å)
XBL781-4410

Figure 6

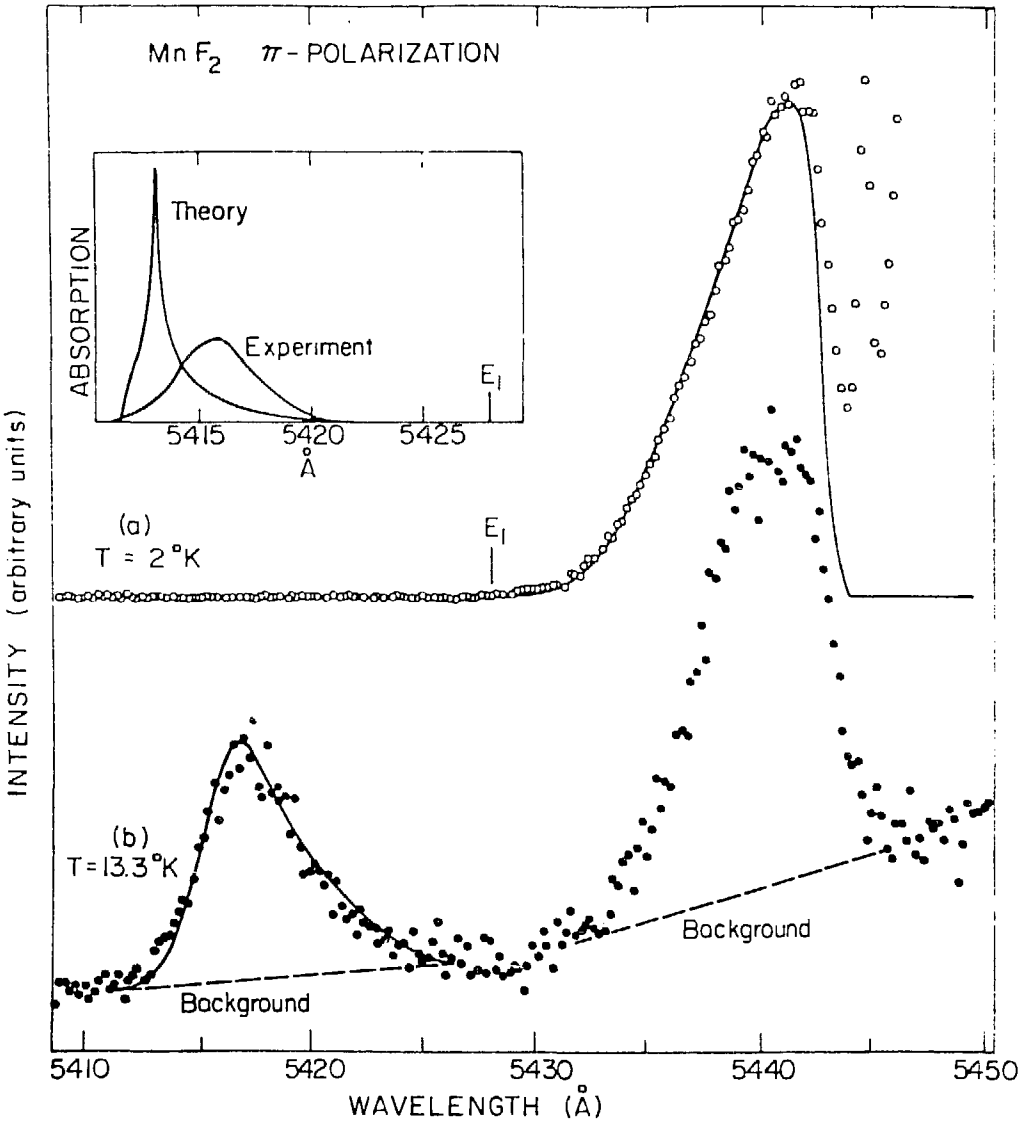

XBL781-4411

Figure 7

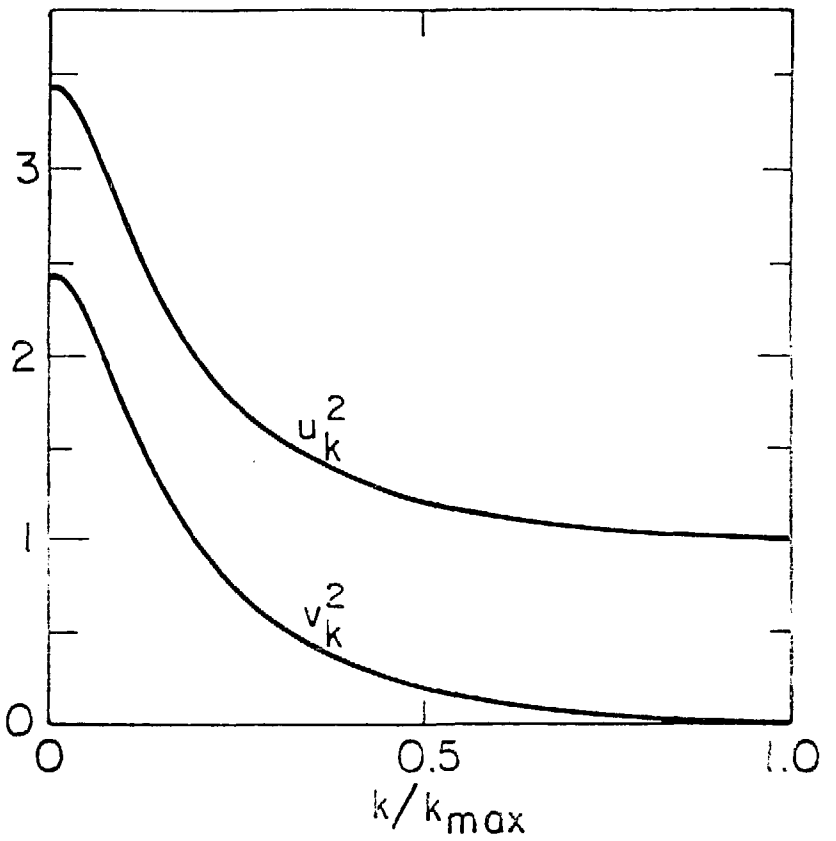

XBL 781-4409 A

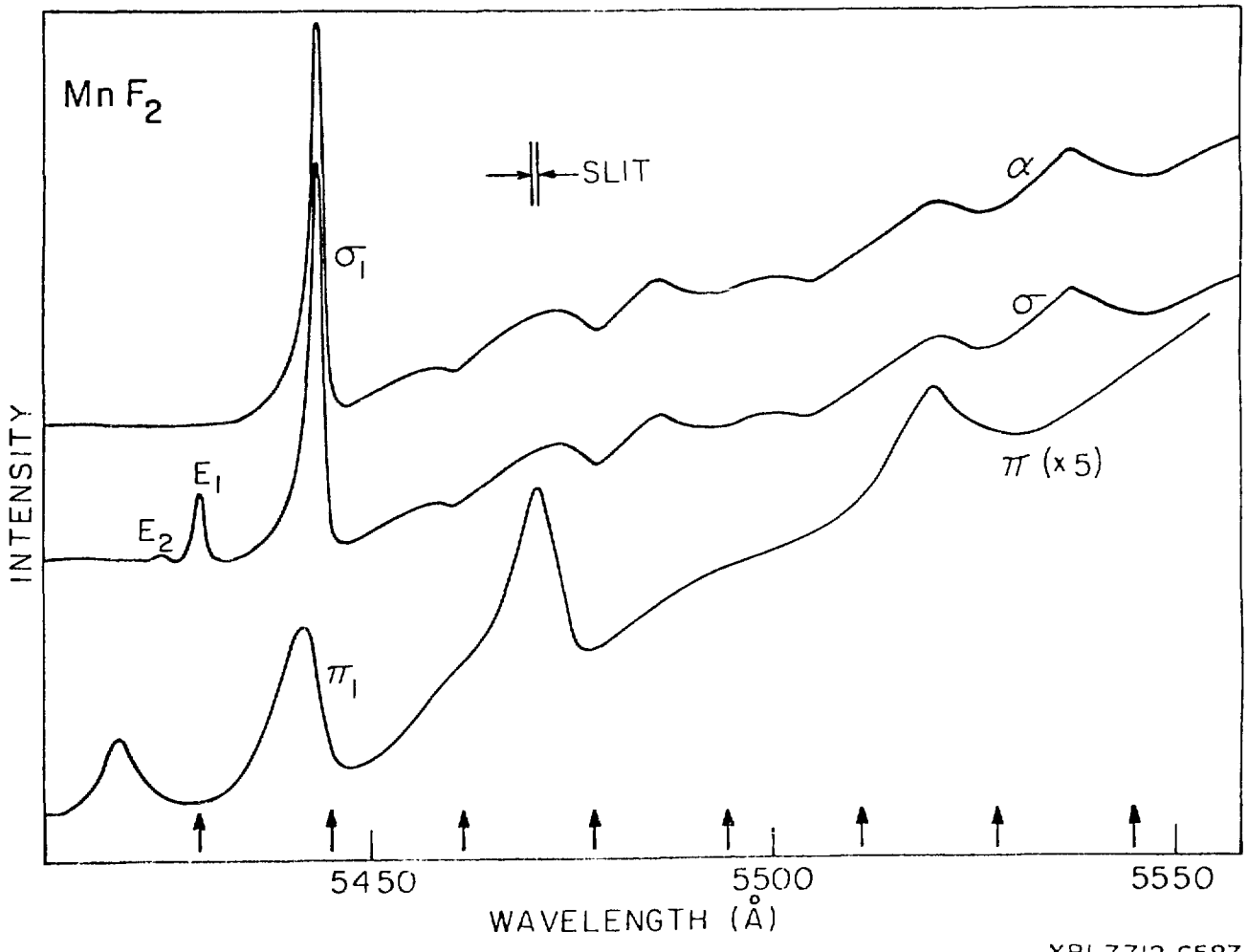
Mn F2
SLIT
α
σ1
σ
E1
E2
π (x 5)
π1
INTENSITY
5450
5500
5550
WAVELENGTH (Å)
XBL7712-6587

Figure 8

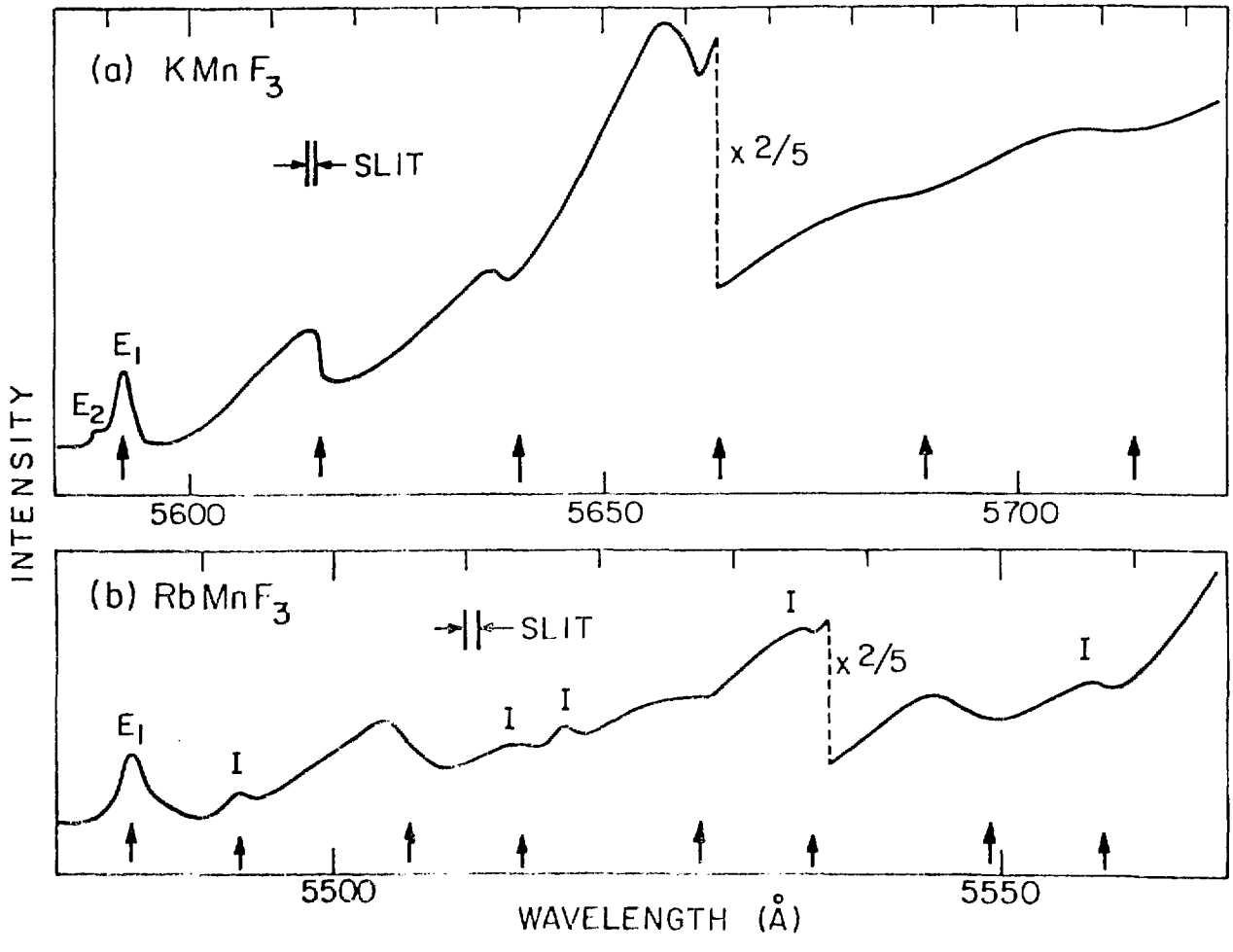

XBL 7712-6588

Figure 9

Figure 10

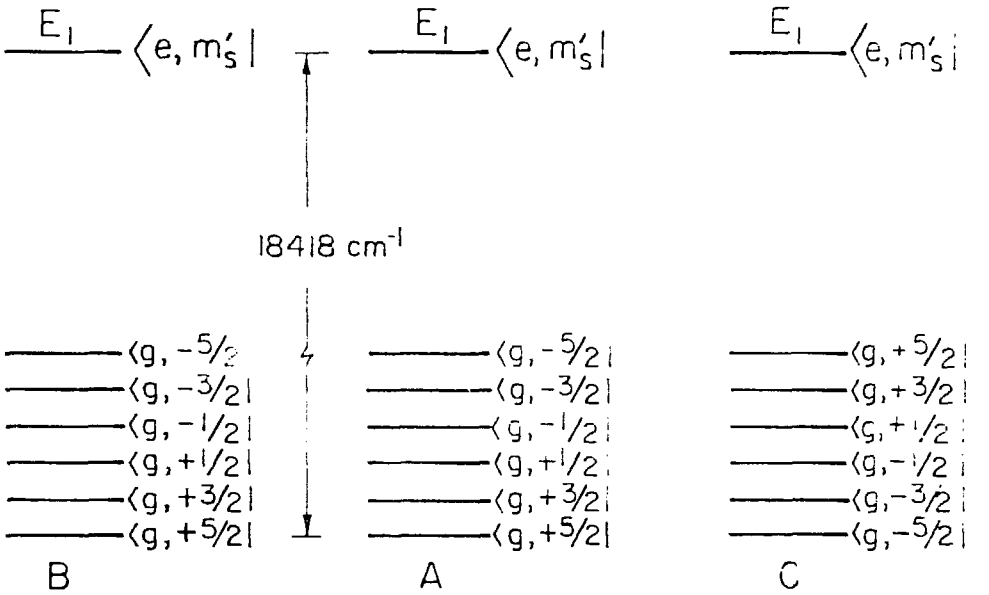

XBL7712-6586A

V. Two-Magnon Resonant Raman Scattering in MnF_2

A. Introduction

Resonant Raman scattering (RRS) involving phonons has been well studied in many semiconductors. Sections II and III in this work are good examples. Here, I report the first investigation[1] on RRS in a magnetically ordered crystal, viz., MnF_2 in the antiferromagnetic phase. We have observed RRS by two magnons.

The optical properties of MnF_2 involving excitons and magnons have been reviewed quite extensively in Section IV. In brief, there is a set of absorption lines around 18450 cm^{-1} (see Fig. 3, Section IV) arising from transitions within the $^6A_{1g} \rightarrow {}^4T_{1g}$ manifold. Lines E_1 and E_2 are due to creation of E_1 and E_2 excitons respectively, via direct magnetic dipole transitions while lines σ_1 (π_1) and σ_2 are the corresponding magnon sidebands. In the luminescence spectrum (see Fig. 5, Section IV), direct and magnon-assisted recombinations of the E_1 excitons give rise to the E_{1L} and σ_{1L} (π_{1L}) luminescence lines respectively, etc.

The Raman spectrum of MnF_2 has been thoroughly studied.[2-4] It consists of four phonon modes and one two-magnon line. No one-magnon line has yet been observed.[5] We are interested in the changes of the Raman spectra when the exciting laser frequency scans through the various absorption lines.

B. Theory

The peak position and the cross-section of the two-magnon line for excitation near σ_1, π_1, and σ_2 lines can be obtained following, for example, Loudon's derivation.[2,3,6] The spin Hamiltonian is of the form

(unless specified, we use the notations of Ref. 2)

$$H_s = \sum_{<i,j>} \sum_{\alpha,\beta} C_{ij}^{\alpha\beta} E_\ell^\alpha E_s^{\beta *} S_i^- S_j^+ \qquad (1)$$

where $C_{ij}^{\alpha\beta} = A_{ij}^{\alpha\beta} + B_{ij}^{\alpha\beta}$

$$A_{ij}^{\alpha\beta} = \sum_{\mu,\nu} \frac{<g_i\downarrow g_j\uparrow|er_\beta|g_i\downarrow\nu_j\uparrow><g_i\downarrow\nu_j\uparrow|V_{ex}|\mu_i\uparrow g_j\downarrow><\mu_i\uparrow g_j\downarrow|er_\alpha|g_i\uparrow g_j\downarrow>}{(E_\nu - \hbar\omega_s)(E_\mu - \hbar\omega_\ell)}$$

+ 11 similar terms

$$B_{ij}^{\alpha\beta} \cong \sum_{\mu,\nu} (<g_i\downarrow g_j\uparrow|er_\beta|\nu_i\downarrow g_j\uparrow><\nu_i\downarrow g_j\uparrow|V|e_i\downarrow g_j\uparrow><e_i\downarrow g_j\uparrow|V_{ex}|\mu_i\uparrow g_j\downarrow> \times$$

$$<\mu_i\uparrow g_j\downarrow|er_\alpha|g_i\uparrow g_j\downarrow>)/[(E_\nu - \hbar\omega_s)(E_\mu - \hbar\omega_\ell)\hbar(\omega_\ell - \omega_E - \omega_m + i\Gamma)] \ .$$

In the above equations, $<g_i|$ is the ground state of the ith Mn ion, $<\mu|$ and $<\nu|$ are the allowed excited states with energies E_μ and E_ν respectively, and $<e|$ is either the E_1 or the E_2 excitonic state with its energy denoted by $\hbar\omega_E$. The magnon frequency is ω_m. The quantities E_ℓ^α and E_s^β represent the α component of the exciting field and the β component of the scattered field respectively, and V and V_{ex} are respectively the direct and exchange terms of the Coulomb interaction. From Eq. (1) we find for the two-magnon Raman cross-section,

$$\frac{d\sigma_{\alpha\beta}}{d\omega_s} = \sum_{\vec{k}} \left| a_{\alpha\beta} + \frac{b_{\alpha\beta}}{\omega_\ell - \omega_E(\vec{k}) - \omega_m(\vec{k}) + i\Gamma} \right|^2 \times$$

$$f_{\alpha\beta}(\vec{k}) \frac{\Gamma'}{|\omega_\ell - \omega_s - 2\omega_m(\vec{k}) + i\Gamma'|^2} \qquad (2)$$

where $a_{\alpha\beta}$ and $b_{\alpha\beta}$ are constant coefficients if we assume the matrix elements in Eq. (1) are constant and $f_{\alpha\beta}(\vec{k})$ is a function of $\vec{k}$. Since the $b_{\alpha\beta}$ term is obtained from higher-order perturbation than the $a_{\alpha\beta}$ term, the former should be negligible in comparison with the latter unless the excitation frequency is close to one of the magnon sidebands, i.e., $\omega_\ell \sim \omega_E + \omega_m(\vec{k})$. Near such a resonance, if we use the approximation $|x + i\Gamma|^{-2} \approx \pi\delta(x)/\Gamma$, we can write

$$d\sigma_{\alpha\beta}/d\omega_s \cong (d\sigma_{\alpha\beta}/d\omega_s)_{NR} + (d\sigma_{\alpha\beta}/d\omega_s)_R \tag{3}$$

with

$$(d\sigma_{\alpha\beta}/d\omega_s)_{NR} = (\pi|a_{\alpha\beta}|^2/\Gamma') \sum_{\vec{k}} f_{\alpha\beta}(\vec{k})\delta[\omega_\ell - \omega_s - 2\omega_m(\vec{k})] \tag{3a}$$

$$(d\sigma_{\alpha\beta}/d\omega_s)_R = (\pi^2|b_{\alpha\beta}|^2/\Gamma\Gamma') \sum_{\vec{k}} f_{\alpha\beta}(\vec{k})\delta[\omega_\ell - \omega_E(\vec{k}) - \omega_m(\vec{k})] \times$$

$$\delta[\omega_\ell - \omega_s - 2\omega_m(\vec{k})] \ . \tag{3b}$$

The total two-magnon Raman cross-section is then given by

$$\sigma_{\alpha\beta} = (\sigma_{\alpha\beta})_{NR} + (\sigma_{\alpha\beta})_R \tag{4}$$

where

$$(\sigma_{\alpha\beta})_R \propto [(d\sigma_{\alpha\beta}(\omega_\ell - \omega_s = 2\omega_\ell - 2\omega_E)/d\omega_s]_{NR} \ . \tag{5}$$

Equation (3b) shows that at resonance, if $(d\sigma_{\alpha\beta}/d\omega_s)_R > (d\sigma_{\alpha\beta}/d\omega_s)_{NR}$,

the peak position of the two-magnon line is determined by

$$\omega_\ell - \omega_s = 2\omega_m(\vec{k}) = 2\omega_\ell - 2\omega_E(\vec{k}) \quad . \tag{6}$$

The above results are easy to understand physically since the resonant part can be considered as due to a magnon-assisted absorption immediately followed by a magnon-assisted emission.

C. Experiment

Our Raman setup described in Sections II and IV was used. A CW dye laser with a linewidth of 0.2 cm^{-1} was used as the excitation source and the sample was immersed in superfluid He at 1.6°K. Scattered light was collected near the sample surface in a 90° or backward scattering geometry. For the particular sample used in the experiment, there was an impurity luminescence line (denoted by I in Fig. 1) overlapping with the σ_{1L} luminescence line.

D. Results and Discussion

No RRS by phonons was observed.[7] Here, we discuss only RRS by two magnons. We found that the two-magnon line showed a resonance enhancement at the magnon sidebands but not at the E_1 and E_2 exciton lines, just as we expected. Figure 1 shows a set of two-magnon Raman spectra at several different excitation frequencies around σ_1 and σ_2 absorption bands. It is seen that the two-magnon line (denoted by M) varies in frequency with ω_ℓ. Deep in resonance, the line is considerably sharper (limited by instrument resolution in Fig. 1). When ω_ℓ falls in the region where σ_1 and σ_2 overlap, two two-magnon lines show up, due to simul-

taneous resonances in σ_1 and σ_2 with two different sets of magnon modes involved. We have plotted the Raman peak shift of the two-magnon line as a function of ω_ℓ in Fig. 2(a), and the corresponding Raman cross-section σ_{xy} (corrected for absorption) vs ω_ℓ in Fig. 2(b). The same results for σ_{xz} are given in Fig. 3.

The results of Figs. 2 and 3 agree well with our earlier description. When $(d\sigma_{\alpha\beta}/d\omega_s)_R > (d\sigma_{\alpha\beta}/d\omega_s)_{NR}$, the Raman shift should obey Eq. (6). We find that we can indeed fit that portion of the data by Eq. (6) assuming $\omega_E(\vec{k})$ is independent of $\vec{k}$. This is shown by the straight lines in Figs. 2(a) and 3(a). The values of constant ω_E deduced from the fit, for RRS near σ_1, σ_2, and π_1 absorption peaks respectively, are $\omega_E(\sigma_1)$ = 18420.7 cm^{-1}, $\omega_E(\sigma_2)$ = 18429.5 cm^{-1}, and $\omega_E(\pi_1)$ = 18405 cm^{-1}. If $\sigma_1(\pi_1)$ and σ_2 are indeed magnon sidebands of E_1 and E_2 and if the assumption of dispersionless $\omega_E(\vec{k})$ is correct, then $\omega_E(\sigma_1)$ and $\omega_E(\pi_1)$ should be equal to the frequency of the E_1 absorption peak and $\omega_E(\sigma_2)$ to the frequency of the E_2 peak. The observed E_1 and E_2 lines are at ω_{E1} = 18419.5 cm^{-1} and ω_{E2} = 18436.5 cm^{-1}. The agreement between $\omega_E(\sigma_1)$ and ω_{E1} is within the experiment uncertainty, supporting the previous suggestion that the dispersion of the E_1 exciton is less than 0.5 cm^{-1}.[8] There is a discrepancy of 7 cm^{-1} between $\omega_E(\sigma_2)$ and ω_{E2}. This indicates that the E_2 exciton has a negative dispersion of 7 cm^{-1} from the zone center to the zone edge, in agreement with the 6.2 cm^{-1} estimate of Sell et al.[9] The fact that the data can still be fitted by a straight line suggests a negligible dispersion of E_2 near the zone edge. There is a big discrepancy of 14.5 cm^{-1} between $\omega_E(\pi_1)$ and ω_{E1}. Since we know E_1 is nearly dispersionless, this makes us suspect that π_1 is not a magnon sideband of E_1 but of a lower-energy excitonic state. However, no such state has

been found in absorption and π_1 has been shown to be indeed the magnon sideband of E_1 in the previous section. Similar difficulty exists in the calculation of the π_1 absorption sideband shape. Even with the exicton-magnon interaction taken into account, the calculated sideband shape[10] and position are quite different from those obtained experimentally.

The rest of the data in Figs. 2(a) and 3(a) can be interpreted qualitatively as follows. On the low-energy side of a magnon sideband, when $(d\sigma_{\alpha\beta}/d\omega_s)_{NR}$ becomes more and more dominant over $(d\sigma_{\alpha\beta}/d\omega_s)_R$, the two-magnon line gradually changes into its off-resonance lineshape and the Raman peak shift moves towards the off-resonance value. On the high-energy side close to the peak of a magnon sideband, the resonance enhancement of those two-magnon modes near the zone edge still dominates (consider Eq. (2) with finite damping constants), leaving the peak position of the two-magnon line more or less unchanged.

We have also found that Eq. (5) describes the observed two-magnon resonance Raman enhancement near magnon sidebands quite well. In Figs. 2(b) and 3(b), the theoretical curves are obtained from Eq. (5) using the experimental lineshape of $(d\sigma_{\alpha\beta}/d\omega_s)_{NR}$ and with $(\sigma_{\alpha\beta})_R$ normalized to its peak value. The discrepancy between theory and experiment is probably a result of the δ-function approximation in the theoretical derivation.

E. Conclusion

We have observed two-magnon RRS in MnF_2 around the magnon sidebands. The mechanism for the two-magnon RRS is different from that for the non-resonant case. With a given excitation frequency ω_ℓ, it selects a particular set of two-magnon modes to be most strongly resonantly enhanced.

Consequently, because of the presence of magnon dispersion, the two-magnon line shifts in frequency as ω_ℓ varies, and two two-magnon lines show up when simultaneous resonance with two magnon sidebands occurs. The resonance enhancement agrees quite well with a simple theoretical description.

References

1. N. M. Amer, T. C. Chiang, and Y. R. Shen, Phys. Rev. Lett. 34, 1454 (1975); 36, 1102 (1976).

2. P. A. Fleury, S. P. S. Porto, and R. Loudon, Phys. Rev. Lett. 18, 658 (1967).

3. P. A. Fleury and R. Loudon, Phys. Rev. 166, 514 (1968).

4. S. P. S. Porto, P. A. Fleury, and T. C. Damen, Phys. Rev. 154, 522 (1967).

5. J. P. Gosso and P. Moch, Proc. III Intl. Conf. Light Scatt. Solids 214 (1975).

6. R. Loudon, Adv. Phys. 17, 243 (1968).

7. With the CW excitation-detection scheme, the phonon modes were in general masked by strong impurity luminescence when exciting near the absorption lines. Therefore, we used the pulsed excitation-detection scheme described in the previous section to look for possible RRS by phonons. The phonon modes were clearly observed and no RRS was found. This is probably due to the weakness of the coupling between lattice vibrations and magnetic excitations.

8. R. E. Dietz, A. E. Meixner, H. J. Guggenheim, and A. Misetich, J. Luminesc. 1, 2, 279 (1970).

9. D. D. Sell, R. L. Greene, and R. M. White, Phys. Rev. 158, 489 (1967).

10. Y. Tanabe, K-I Gondaira, and H. Murata, J. Phys. Soc. Japan 25, 1562 (1968).

Figure Captions

Fig. 1 Two-Magnon Raman spectra (denoted by M) at several different excitation frequencies ω_ℓ. Peaks I and σ_{1L} correspond to impurity and magnon-assisted luminescence lines respectively.

Fig. 2 (a) Two-magnon Raman shift and (b) Two-magnon Raman cross-section as a function of the excitation frequency ω_ℓ. The exciting and the scattering radiation are polarized along $\hat{y}$ and $\hat{x}$ respectively ($\hat{x},\hat{y} \perp \hat{c}$).

Fig. 3 (a) Two-magnon Raman shift and (b) Two-magnon Raman cross-section as a function of the excitation frequency ω_ℓ. The exciting and the scattering radiations are polarized along $\hat{z}$ and $\hat{x}$ respectively ($\hat{x} \perp \hat{c}$ and $\hat{z} \parallel \hat{c}$).

Figure 1

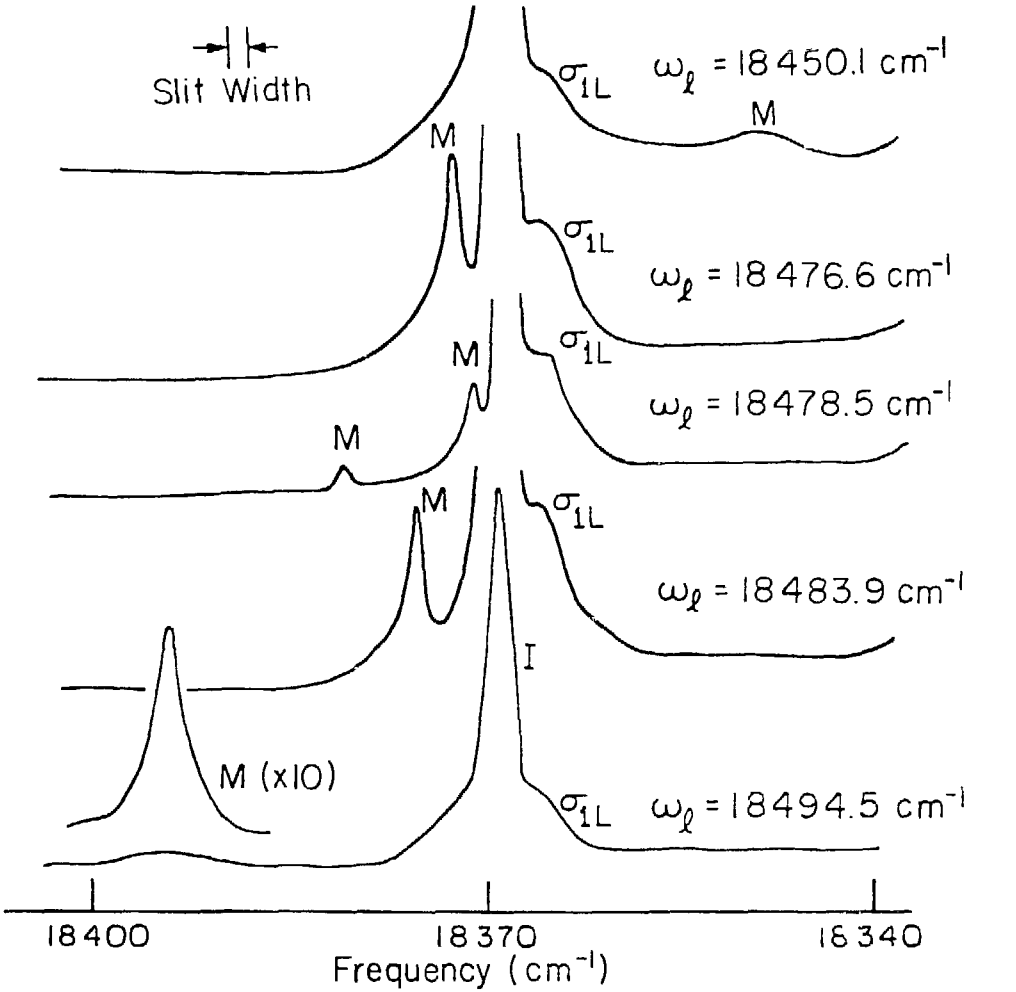

XBL753-5991A

Figure 2

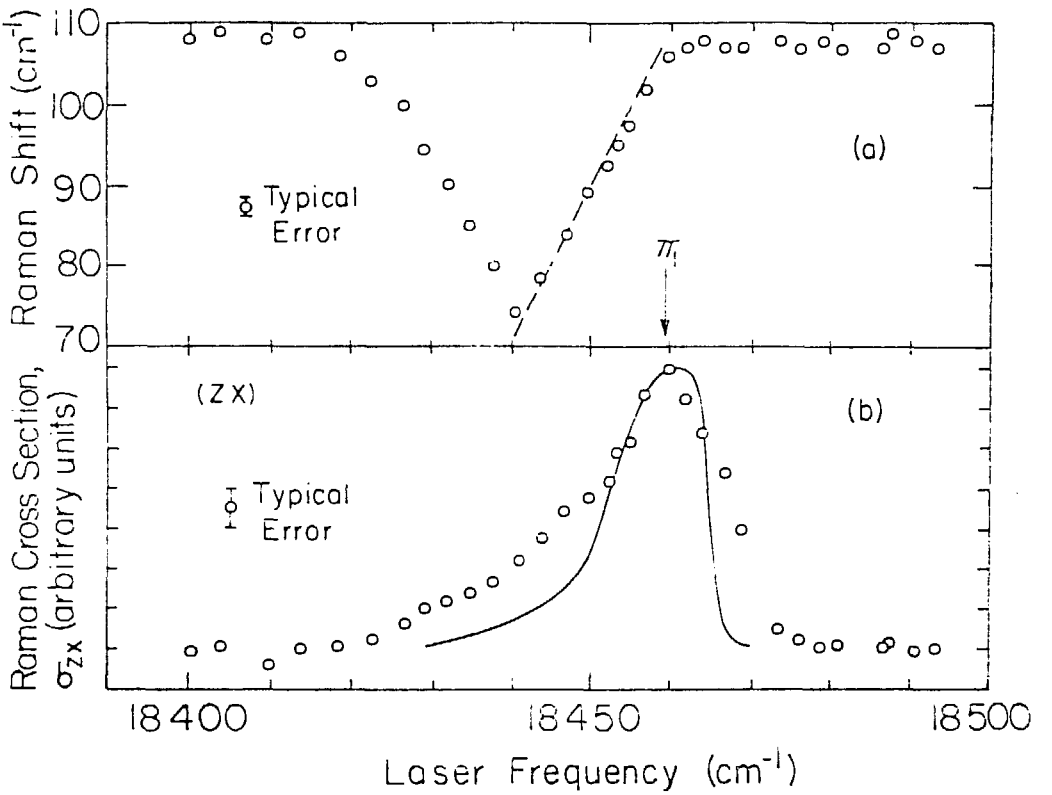

XBL 753-5989

Figure 3

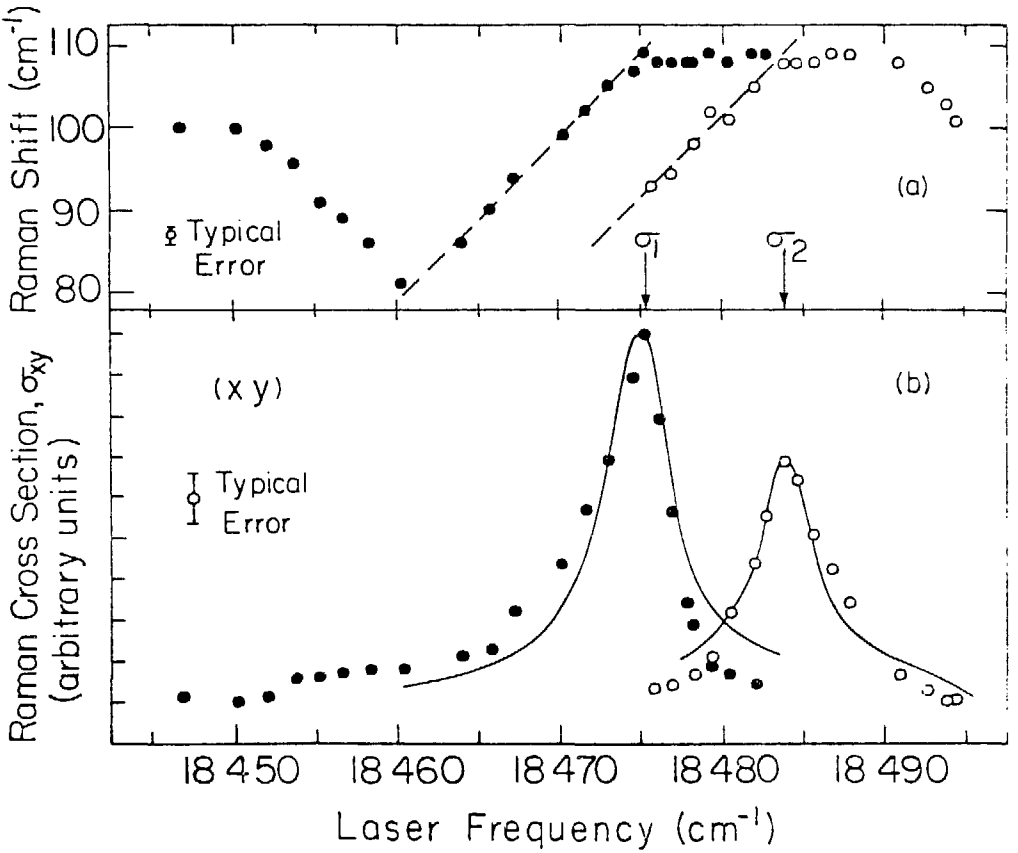

XBL 753-5988

VI. Interactions of Collective Excitations in MnF_2

A. Introduction

The common practice of treating the elementary excitations in a solid as independent particles works well under many circumstances. Nevertheless, this approximation generally breaks down in high excitation experiments (HEE) and sideband experiments (SBE). In HEE, a high density of elementary excitations is generated and new spectral features may appear. A well known example is the condensation of Wannier excitons in Si and Ge.[1] It is interesting to study similar effects for Frankel excitons. The E_1 exciton of MnF_2, with its long lifetime and narrow linewidth, provides a clean system for studying the exciton-exciton interaction. Some theoretical considerations and preliminary experimental results will be presented here. In SBE, two or more elementary excitations are generated simultaneously at close proximity and therefore strong renormalizing effects may occur. We have already seen one example in Section IV, viz., the exciton-magnon interaction[2] in MnF_2. We will examine possible experiments to measure this interaction. Other interesting interactions such as the magnon-magnon[3] and magnon-phonon[4] interactions have been studied extensively in the literature and will not be discussed here.

B. Theory

Referring back to Eqs. (2) and (4) of Section IV and related discussions, it is clear that one can selectively prepare E_1 exciton states in a shell in the Brillouin zone by monoenergetically pumping the magnon sideband of E_1. The exact distribution of the prepared E_1 excitons in

the Brillouin zone depends on the three dimensional structures of the magnon dispersion and the exciton-magnon interaction. Subsequently, by monitoring the magnon sideband luminescence spectrum the distribution of the E_1 exciton states in the Brillouin zone can be inferred. By pumping the magnon sideband of E_1 in absorption and monitoring the magnon sideband of E_1 in emission with certain time delay, two pieces of information can be obtained. With zero time delay, the exciton-magnon interaction can be deduced. This interaction has been reviewed quite extensively in Section IV and Ref. 2, and will not be repeated here. With variable time delay, the spectral diffusion of the E_1 excitons in the Brillouin zone as a function of time can be obtained. This time dependence is intimately related to the exciton-exciton scattering rate in the Brillouin zone, hence the exciton-exciton interaction can then be deduced.

Macfarlane et al.[5] did an experiment along this line. Due to the low resolution in their experiment, they could only deduce the order of magnitude of the exciton-exciton scattering rate. The following approximate rate equation can be used to describe their results.

$$d\rho_k/dt = P_k - [A(\int_{BZ} \rho_k d^3k) + B][\rho_k - \langle\rho_k\rangle] - \rho_k/\tau \ ,$$

with

$$A \sim 10^{-10} \text{ cm}^3/\text{sec} \quad ; \quad B(4^\circ K) < 10^6/\text{sec} \ . \tag{1}$$

ρ_k is the number of E_1 excitons with wavevector $\vec{k}$ per unit volume in real space and per unit volume in $\vec{k}$-space; it is a dimensionless quantity. $\langle\rho_k\rangle$ is the average of ρ_k in $\vec{k}$-space.

$$\langle \rho_k \rangle = \int_{BZ} \rho_k d^3k \Big/ \int_{BZ} d^3k \qquad (2)$$

where the integration is over the whole Brillouin zone, and

$$\int_{BZ} d^3k = 5.945 \times 10^{23}/cm^3 \qquad (3)$$

The optical pumping rate P_k is the number of E_1 excitons with wave vector $\vec{k}$ per unit volume in real space and per unit volume in $\vec{k}$-space generated per unit time. $\tau \approx 200$ μsec is the exciton lifetime which is dominated by trapping by impurities. Equation (1) says the exciton population distribution ρ_k generated by optical pumping tends to randomize in $\vec{k}$-space by two mechanisms, the first being exciton-exciton scattering with rate constant $A \sim 10^{-10}$ cm^3/sec, and the second being collision with impurities and phonons with rate constant $B < 10^6/sec$ for a temperature below 4°K. If P_k as a function of time is known, ρ_k can be solved. The exact value of P_k depends on the manner of excitation, the magnon dispersion, the exciton-magnon interaction, and the linewidth of E_1. It can be calculated exactly in principle, though complicated. For our purpose, a crude estimate of P_k for a given excitation condition is sufficient. This is illustrated in the following numerical example. If a focused laser beam of 1 W power and 50 μ diameter is used to pump around the peak of the magnon sideband in absorption, the photon current is 2.7×10^{18} photons/sec and the photon flux is 1.4×10^{23} photons/cm^2-sec. Assuming an absorption length of ~ 1 cm (peak absorption is 3.0 cm^{-1} for σ_1 and 1.7 cm^{-1} for π_1),[6] we obtain

$$\int_{BZ} P_k d^3k = 1.4 \times 10^{23} \text{ excitons/cm}^3\text{-sec} \qquad (4)$$

which is the number of E_1 excitons generated per unit volume per unit time. P_k is zero except for $\vec{k}$ in a thin shell in the Brillouin zone. The thickness of this shell depends on the laser linewidth and the E_1 exciton linewidth[7] ($\sim 0.5\ cm^{-1}$). Assuming a laser linewidth of $\sim 1\ cm^{-1}$, neglecting the exciton-magnon interaction, and approximating the E_1 dispersion with a linear dispersion (maximum magnon energy $\sim 5\ cm^{-1}$), we estimate the volume of the shell to be about $4\pi(\pi/5.5)^2(1/5)^3 \sim 2\%$ of the Brillouin zone. Therefore, by Eqs. (4) and (5),

$$P_k = 1.4 \times 10^{23}/(0.05 \times 3.945 \times 10^{23})$$

$$= 0.4\ \text{excitons/sec} \qquad (7)$$

within the shell and zero elsewhere.

Another experimental result related to the exciton-exciton interaction is the observation of two-exciton absorption lines.[6,8] A two-exciton transition can be considered as an exciton sideband of another exciton. The two-exciton transition energies are in general different from the sum of the energies of the separate single transitions. The energy mismatch is then a direct measure of the exciton-exciton interaction. Stokowski et al.[8] observed $E_1 + E_2$ and $2E_2$ two-exciton transitions in MnF_2 with energy mismatch of $+ 0.1\ cm^{-1}$ and $- 0.4\ cm^{-1}$, respectively. Unfortunately, the $2E_1$ two-exciton transition was not observed probably due to its much weaker oscillator strength.

The two-exciton transition energy mismatch and the exciton-exciton scattering rate can be related easily. The complete Hamiltonian for the exciton is

$$H = E_o\left(\sum_i a_i^+ a_i + \sum_j a_j^+ a_j\right) + \lambda\left(\sum_{<ii'>} a_i^+ a_i a_{i'}^+ a_{i'} + \sum_{<jj'>} a_j^+ a_j a_{j'}^+ a_{j'}\right) +$$

$$+ \sum_{<ij>} a_i^+ a_i a_j^+ a_j \qquad (6)$$

where E_o is the energy of the k_1 exciton state, a_i^+ the creation operator for an exciton localized on the i-th Mn^{++} ion of the spin-up sublattice, a_j the annihilation operator for an exciton localized on the j-th Mn^{++} ion of the spin-down sublattice, etc., λ and μ the exciton-exciton interaction energies. Since the exciton-exciton interaction is of short range, the second and the third terms in Eq. (6) are summed only over nearest neighbors $<ii'>$, $<jj'>$ on the same sublattice and next nearest neighbors $<ij>$ on the opposite sublattice, respectively. When there is only one exciton present, Eq. (6) predicts an energy of E_o as it should be. When there are two excitons present, Eq. (2) predicts a total energy of $2E_o$ if they are well separated, $2E_o + \lambda$ if they sit on nearest neighbors, and $2E_o + \mu$ if they sit on next nearest neighbors. For the two-exciton absorption transition, the two excitons generated are sitting on next nearest neighbors due to the spin selection rule. Therefore, μ is simply the measured energy mismatch in two-exciton transitions.

By transforming the local variables in Eq. (6) to wave variables, we have

$$H = E_o\sum_k \left(\alpha_k^+\alpha_k + \beta_k^+\beta_k\right) + \frac{2\lambda}{N}\sum_{k_1,k_2,p} \cos(cp_z)\left[\alpha_{k_2+p}^+\alpha_{k_1-p}^+\alpha_{k_2}\alpha_{k_1} + \right.$$

$$\left.\beta_{k_2+p}^+\beta_{k_1-p}^+\beta_{k_2}\beta_{k_1}\right] + \frac{8\mu}{N}\sum_{k_1,k_2,p} \cos(ap_x/2)\cos(ap_y/2)\cos(cp_z/2) \times$$

$$\beta_{k_2+p}^+\alpha_{k_1-p}^+\beta_{k_2}\alpha_{k_1} \qquad (7)$$

where a^+ and b^+ are exciton creation operators for the spin-up and spin-down sublattices, respectively, etc., a and c lattice constants, and N the number of unit cells in the crystal. The exciton-exciton scattering rate can be obtained by applying the Fermi golden rule to the states $|n_{k_1\uparrow} n_{k_2\uparrow} n_{k_1-p\uparrow} n_{k_2+p\uparrow}\rangle$ and $|n_{k_1\uparrow} n_{k_2\downarrow} n_{k_1-p\uparrow} n_{k_2+p\downarrow}\rangle$, and we have

$$\frac{dn_{k_1\uparrow}}{dt} = -\frac{2\pi}{\hbar^2}\sum_{k_2,p}\left\{\frac{4\lambda^2}{N^2}\cos^2(cp_z)\left(n_{k_2+p\uparrow}+1\right)\left(n_{k_1-p\uparrow}+1\right)n_{k_2\uparrow}n_{k_1\uparrow} + \right.$$

$$\frac{64\mu^2}{N^2}\cos^2(ap_x/2)\cos^2(ap_y/2)\cos^2(cp_z/2)\left(n_{k_2+p\downarrow}+1\right)\left(n_{k_1-p\uparrow}+1\right)$$

$$\left.\cdot\, n_{k_2\downarrow}n_{k_1\uparrow}\right\}\delta\left(\omega_{k_2+p}+\omega_{k_1-p}-\omega_{k_2}-\omega_{k_1}\right) \qquad (8)$$

where $n_{k_1\uparrow}$ is the mode occupation number for the spin-up sublattice, etc., and $\hbar\omega_{k_1}$ the energy of an exciton with momentum $\hbar k_1$, etc. The δ-function is always satisfied for the dispersionless E_1 exciton of MnF_2, therefore it should be replaced by $(4\ln 2/\pi)^{\frac{1}{2}}/\Delta\omega$, where $\Delta\omega$ is the Gaussian linewidth of the E_1 exciton.[7] The mode occupation numbers are much less than 1 under most experimental conditions, therefore we have

$$\frac{dn_{k_1\uparrow}}{dt} = -\frac{2\pi}{\hbar^2\Delta\omega}\left(\frac{4\ln 2}{\pi}\right)^{\frac{1}{2}}n_{k_1\uparrow}\sum_{k_2,p}\left\{\frac{4\lambda^2}{N^2}\cos^2(cp_z)n_{k_2\uparrow} + \right.$$

$$\left.\frac{64\mu^2}{N^2}\cos^2(ap_x/2)\cos^2(ap_y/2)\cos^2(cp_z/2)n_{k_2\downarrow}\right\} \qquad (9)$$

The sum over $\vec{p}$ can be easily evaluated. Equation (9) becomes

$$\frac{dn_{k_1\uparrow}}{dt} = -\frac{4}{N\hbar^2\Delta\omega}(\pi\ln 2)^{\frac{1}{2}}n_{k_1\uparrow}\sum_{k_2}\left(\lambda^2 n_{k_2\uparrow} + 4\mu^2 n_{k_2\downarrow}\right) \qquad (10)$$

Assuming $n_{k\uparrow} = n_{k\downarrow}$, an expression for A in Eq. (1) is easily derived.

$$A = \frac{2}{N_o \hbar^2 \Delta\omega} (\ln 2)^{\frac{1}{2}} (\lambda^2 + 4\mu^2) \tag{11}$$

where N_o is the number of unit cells per unit volume. With $\hbar\Delta\omega = 0.5$ cm^{-1} [6,7] and $A \sim 10^{-10}$ cm^3/sec, we obtain

$$\sqrt{\lambda^2 + 4\mu^2} \sim 1 \text{ cm}^{-1} \tag{12}$$

The $2E_1$ two-exciton absorption, if ever observable, should have an energy mismatch $\hbar\mu \lesssim 1$ cm^{-1}.

The energy shift of the E_1 exciton line under high level excitation can be evaluated by the equation of motion

$$i\hbar \frac{d\alpha_k}{dt} = E_{k\uparrow}\alpha_k = [\alpha_k, H] \tag{13}$$

where $E_{k\uparrow}$ is the renormalized energy for the spin-up sublattice. By Eqs. (7) and (13), we obtain

$$E_{k\uparrow}\alpha_k = E_o\alpha_k + \frac{4\lambda}{N}\sum_{p,q} \cos(cp_z)\alpha^+_{q+p}\alpha_q\alpha_{k+p} + \frac{8\mu}{N}\sum_{p,q} \times$$

$$\cos(ap_x/2)\cos(ap_y/2)\cos(cp_z/2)\beta^+_{q+p}\beta_q\alpha_{k+p} \tag{14}$$

Invoking the generalized Hartree-Fock approximation,[10] we obtain

$$E_{k\uparrow} \simeq E_o + \frac{4\lambda}{N}\sum_p \cos(cp_z)n_{k+p\uparrow} + \frac{4\lambda}{N}\sum_p n_{p\uparrow} + \frac{8\mu}{N}\sum_p n_{p\downarrow} \tag{15}$$

The renormalized energy depends explicitly on the mode occupation numbers. Assuming

$$n_{k\uparrow} = n_{k\downarrow} = \text{constant} \tag{16}$$

corresponding to a totally relaxed exciton distribution, we obtain

$$E = E_{k\uparrow} = E_{k\downarrow} = E_o + 4(\lambda + 2\mu)(n/2N) \tag{17}$$

where n is the total number of excitons, and n/2N is the fractional number of the Mn^{++} ions which are excited. For a fully excited system, n/2N is equal to one and the energy shift predicted by Eqs. (12) and (17) is only a few wavenumbers. In the above derivation, we have implicitly assumed the system is stable against the formation of new phases, such as biexcitons, exciton liquids, etc. The justification relies mostly on experimental results.

C. Experiments

A few experiments related to the exciton-exciton and exciton-magnon interactions are examined here. Some of them have actually been tried in our laboratory. The experimental setup used has been described in previous sections.

(i) Probing the exciton-magnon interaction by CW excitation-detection

We selectively prepare the exciton distribution in a shell in $\vec{k}$-space by CW optically pumping the magnon sideband. The geometry of the shell depends on the magnon dispersion and the exciton-magnon interaction. The prepared excitons relax in $\vec{k}$-space according to Eq. (1).

The steady state distribution of excitons in the $\vec{k}$-space is monitored by the magnon sideband luminescence. If the relaxation rate is slow enough, a nonuniform distribution of excitons should be observed and the exciton-magnon interaction can be deduced.

Assuming exciting laser power of x W focused into the sample with a beam diameter of 50 μ, and a wavelength near the Γ_1 absorption peak (absorption length ~ 1 cm), we obtain from Eqs. (4) and (5)

$$\int_{BZ} P_k d^3k = 1.4 \times 10^{23} \cdot x \text{ excitons/cm}^3\text{-sec} \tag{18}$$

and

$$P_k = 4.4 \times \text{excitons/sec} \tag{19}$$

within the shell and zero elsewhere. Integrating Eq. (1) over $\vec{k}$, we obtain

$$\frac{d}{dt}\int_{BZ} \rho_k d^3k = \int_{BZ} P_k d^3k - \frac{1}{\tau}\int_{BZ} \rho_k d^3k \tag{20}$$

For CW experiment, the time derivative is zero. Therefore,

$$\int_{BZ} \rho_k d^3k = 2 \times 10^{-4} \times \int_{BZ} P_k d^3k$$

$$= 2.8 \times 10^{19} \cdot x \text{ excitons/cm}^3 \tag{21}$$

By Eqs. (2) and (3), we obtain

$$\langle \rho_k \rangle = 7.1 \times 10^{-5} \cdot x \tag{22}$$

Substituting these values into Eq. (1), we obtain, for $\vec{k}_1$ within the shell selectively pumped by the laser

$$0 = 4.4\ x - [10^{-10} \times 2.8 \times 10^{19} \cdot x + B][\rho_{k_1} - 7.1 \times 10^{-5} \cdot x] - 5 \times 10^{3}\ \rho_{k_1} \tag{23}$$

and for $\vec{k}_2$ outside the shell

$$0 = 0 - [10^{-10} \times 2.8 \times 10^{19} \cdot x + B][\rho_{k_2} - 7.1 \times 10^{-5} \cdot x] - 5 \times 10^{3}\ \rho_{k_2} \tag{24}$$

These can be simplified to yield

$$R \equiv \frac{\rho_{k_1} - \rho_{k_2}}{\rho_{k_2}} = \frac{6.2 \times 10^{4}}{2.8 \times 10^{9} \cdot x + b} \tag{25}$$

R is the ratio of the excess population of excitons to the background, and is therefore the signal to background ratio expected in the luminescence spectrum. At higher pumping level (larger x), the ratio R is degraded due to larger exciton-exciton scattering rate.

We have performed this experiment at 2°K for various pumping levels ($10^{-6} < x < 0.1$) in the manner described in Section IV. No noticeable change in luminescence spectrum was observed. The noise to signal ratio in our spectrum around the σ_1 luminescence peak was approximately given by

$$N/S \approx 0.05 + 3.2 \times 10^{-4} \cdot x^{-\frac{1}{2}} \tag{26}$$

where the frist term was due to the laser power fluctuation ($\sim 4\%$) and spectrometer driver jitter ($\sim 1\%$) within an integration time ~ 5 seconds, and the second term due to the quantum noise of the light emitting process. For an incident laser power of 1 W ($x = 1$), typically 10^7 photon counts were collected during the integration time of ~ 5 seconds. The quantum noise to signal ratio was then $10^{7/2}/10^7 = 3.2 \times 10^{-4}$. Since we did not observe the effect, the following limit is set by Eqs. (25) and (26).

$$0.05 + 3.2 \times 10^{-4} \cdot x^{-\frac{1}{2}} \geqslant 6.2 \times 10^4/(2.8 \times 10^9 \cdot x + B) \qquad (27)$$

This can be solved to yield

$$B \geqslant \frac{1.9 \times 10^8}{x^{-\frac{1}{2}} + 1.6 \times 10^2} - 2.8 \times 10^9 \cdot x \quad (\text{sec}^{-1}) \qquad (28)$$

The right-hand side of Eq. (28) attains its maximum value of $\sim 5 \times 10^5$ when $x = 5 \times 10^{-5}$. Therefore

$$B(2°K) \geqslant 5 \times 10^5/\text{sec} \qquad (29)$$

From the data of Macfarlane et al.,[5]

$$B(4°K) < 10^6/\text{sec} \qquad (30)$$

We conclude

$$B \sim 10^6/\text{sec} \qquad (31)$$

at low temperatures.

It is clear from the above analysis that an improvement in signal to noise ratio is necessary in order to see this effect. From Eqs. (25), (26) and (30), it is easy to show that the ratio of R to N/S is maximized for $x \approx 10^{-4}$. At this value of x, $R \approx 5 \times 10^{-2}$ and $N/S \approx 8 \times 10^{-2}$. The laser power fluctuation contributes 4×10^{-2} to N/S; it is therefore non-negligible. In fact, if the laser power fluctuation can be eliminated, $N/S \lesssim R$ and the effect should be marginally observable. The laser power fluctuation can be either eliminated by using an active feedback system or avoided by adopting a phase sensitive detection scheme. Both techniques are not difficult to apply and should be tried in the future.

(ii) Probing the exciton-magnon interaction by pulsed excitation-detection

This is similar to Experiment (i) except the excitation and detection are done in very short time intervals. If the time intervals involved are short compared with the exciton relaxation time, the unrelaxed exciton distribution is observed and the exciton-magnon interaction can be deduced.

Let Δt_1 and Δt_2 (sec) be the excitation and detection intervals, respectively. Obviously we would like to choose them to have the same time origin because otherwise the detector would miss the signal if the beginning of Δt_1 should be after the beginning of Δt_2, or the prepared exciton distribution would have relaxed more than necessary if the beginning of Δt_1 should be before the beginning of Δt_2. Also we would like to choose

$$\Delta t_1 \leqslant \Delta t_2 \tag{32}$$

to avoid wasting the pump laser energy.

If the laser has peak intensity $P(W/cm^2)$ and a wavelength near the E_1 absorption peak (absorption length ~ 1 cm; photon energy ≈ 2.29 eV), then about

$$(6.25 \times 10^{18}/2.29)P\Delta t_1 \sim 3 \times 10^{18}\ P\Delta t_1 \tag{33}$$

excitons per cm^3 are generated after each laser pulse. By the definition of P_k (see Eqs. (1) and (20)) and Eq. (33), we obtain

$$\int_{\Delta t_1} dt \int_{BZ} P_k\, d^3k = 3 \times 10^{18}\ P\Delta t_1 \tag{34}$$

where the first integration is over the pulse duration time Δt_1. Integrating Eq. (20) with respect to t over the interval Δt_1, we obtain

$$\int_{BZ} \rho_k d^3k = \int_{\Delta t_1} dt \int_{BZ} P_k d^3k - \frac{\Delta t}{\tau} \int_{BZ} \rho_k d^3k \tag{35}$$

right after the laser pulse. Assuming $\Delta t_1 \ll \tau$ (~ 200 μsec) and combining Eqs. (34) and (35), we obtain

$$\int_{BZ} \rho_k d^3k \simeq 3 \times 10^{18}\ P\Delta t_1 \tag{36}$$

at the end of the laser pulse. Substituting Eqs. (36) and (31) into Eq. (1), the total exciton relaxation rate in $\vec{k}$-space is

$$A \int_{BZ} \rho_k d^3k + B = 3 \times 10^8\ P\Delta t_1 + 10^6 \quad (sec^{-1}) \tag{37}$$

The detection interval Δt_2 should be no longer than the inverse of the relaxation rate in order to observe the unrelaxed distribution, while as long as possible to see more signal. The optimum condition is given by

$$(\Delta t_2)^{-1} = 3 \times 10^8 P\Delta t_1 + 10^6 \tag{38}$$

The detection duty factor (DF), defined as the ratio of the detection interval Δt_2 to the exciton lifetime τ if $\Delta t_2 \ll \tau$, is equal to

$$DF = \Delta t_2/\tau = 5 \times 10^3 \Delta t_2 \tag{39}$$

The number of detected luminescence photons is proportional to both the detection duty factor and the number of excitons generated after each laser pulse. By Eqs. (33) and (39), the signal is maximized if

$$P\Delta t_1 \Delta t_2 = \text{maximum.} \tag{40}$$

Substituting Eq. (38) into Eq. (40), the condition becomes

$$P\Delta t_1 = \text{maximum,} \tag{41}$$

or

$$\Delta t_2 = \text{minimum.} \tag{42}$$

There is also a limit on P given by

$$P \leqslant P_b \tag{43}$$

where $P_b \approx 5 \times 10^8$ W/cm^2 is the experimentally determined sample breakdown threshold intensity.

There are in total four independent conditions given by Eqs. (32), (38), (41), and (43) for the three independent variables P, Δt_1, and Δt_2. After some simple algebra, it can be shown the solution is given by

$$\Delta t_1 = \Delta t_2 \approx 3 \times 10^{-9} \text{ sec}; \tag{44}$$

$$P = P_b = 5 \times 10^8 \text{ W/cm}^2. \tag{45}$$

The amount of detected signal is also proportional to the laser repetition rate R. However, R should be kept below $1/\tau$, or

$$R \lesssim 1/\tau = 5 \text{ kHz} \tag{46}$$

to avoid appreciable luminescence signal overlapping between successive laser pulses. If $R > 1/\tau$, the residual exciton population from previous laser pulses would contribute to the exciton-exciton scattering rate and the siganl to background ratio (contrast) of the spectrum would be degraded. Eqs. (44)-(46) are the conditions to be satisfied experimentally.

A nitrogen laser pumped dye laser is likely to be the most easily available pump source which satisfied Eqs. (44)-(46). Let us assume the following characteristics of such a laser : pulse width = 3 nsec, energy per pulse = 30 μj, and repetition rate R = 100 Hz.[11] The peak intentsity P is 500 MW/cm^2 when the laser light is focused down to a beam diameter of ~ 50 μ. The average power is 3 mW.

A clean luminescence spectrum with good signal to noise ratio and resolution can be obtained in about 2 minutes using the CW excitation-detection scheme (Experiment (i)) with a laser power of 1 mW. In the present experiment, the average incident power is about 3 mW, however the signal is reduced by the detection duty factor of $\sim 2 \times 10^{-5}$ (Eq. (39)) compared with the CW experiment. Therefore a minimum experimental time of $\sim 3 \times 10^{4}$ minutes $\sim$ 20 days is necessary for the present experiment. This is beyond our capability and we have not tried this experiment.

(iii) Induced absorption

A pump laser is used to selectivily prepare the exciton and magnon distributions in the Brillouin zone. The excitons and magnons generated can absorb light to reach higher levels. A second probe laser is used to monitor the absorption as functions of pump power, time delay (in case of pulsed excitation), pump and probe wavelengths, etc. Under favorable conditions, some useful information may be extracted. For example, the selectively prepared magnon states can absorb light to reach the E_1 exciton level. By monitoring the absorption in the antiStokes magnon sideband absorption region, the exciton-magnon interaction can be deduced. The situation is very similar to that in Experiments (i) and (ii), and the relevant theory can be developed in much the same way. Here, we need to worry about the relaxation of the prepared magnon distribution via magnon-magnon, magnon-phonon, and magnon-impurity collisions. Since most of the relevant paremeters are not known in the present case, we merely mention this possible experiment without detailed numerical analysis.

(iv) Probing the exciton-exciton interaction by HEE

Under high level excitation, the E_1 excitons either shift in energy according to Eq. (17) or form new phases such as biexcitons, exciton liquid, etc. We performed this experiment using the pulsed excitation-detection scheme described in Section IV. The flashlamp pumped dye laser was used to excite the E_1 absorption line directly. The highest pumping level was 500 MW/cm^2 (~ 5 mj per pulse focused down to a beam diameter of ~ 50 μ and a pulse width of ~ 0.4 μsec) limited by sample breakdown. The E_1 exciton line had a peak absorption coefficient of 0.71 cm^{-1} [6] Theoretically, $n/2N \simeq 0.01$ in Eq. (17) and a shift of about 0.01 cm^{-1} was expected. Experimentally, we monitored the E_1 luminescence line and no shift was observed with our highest spectrometer resolution of about 0.5 cm^{-1}. Furthermore, we didn't observe any new spectral line, which could be identified as biexcitons or exciton liquid, showing up as the pumping intensity was increased. Therefore, the mean field theory we used to derive Eq. (17) was in no contradiction with the experimental results.

A definite and quantitative check of our theory is difficult due the low breakdown threshold of our MnF_2 samples and the limit on resolution of our spectrometer. A possible alternative is to pump the higher allowed transitions. For allowed band to band transitions (such as $d \rightarrow p$, $d \rightarrow s$, or $p \rightarrow s$, etc.), the absorption length is typically 10^{-6} cm. With ~ 5 mj inciednt energy, the transition is easily saturated. If the excitations quickly relax down to the metastable E_1 state, $n/2N$ can be close to one. The shift is expected to be ~ 1 cm^{-1} and should be detectable. However, the temperature rise of the sample after the laser pulse can be very high due to the phonons emitted as the generated excitations relax down. This may complicate the final analysis. Neverthe-

less, we hope to perform this experiment in the future.

(v) Two-photon excitation

Some energy levels may be reached by two-photon absorption if the selection rules are satisfied. In particular, if an excitation is Raman active, it can also be reached by two-photon absorption. The two-magnon transition is an example. A far infrared molecular laser is needed for this purpose. Of more importance is the $2E_1$ two-exciton transition which has not been observed by single-photon absorption. If this can be observed by two-photon transition, the result should provide partial verification of our theory (Eq. (12) and related discussion).

D. Conclusion

We have studied the exciton-exciton and exciton-magnon interactions in MnF_2. In particular, a detailed theory of the exciton-exciton interaction is developed. A few possible experiments are examined. The techniques used are of either the pump-and-monitor or the pump-and-probe type. Many other experiments and techniques are possible, for example, the time correlated photon counting technique for precise relaxation time measurements,[12] the application of external magnetic[13] or electric field, stress experiment,[14] high pressure experiment, etc. The collective excitations in MnF_2 and their mutual interactions are clean enough that detailed quantitative theories can often be developed, yet they are complicated enough that a complete description is awaiting more sophisticated theories and experiments. We hope this work will stimulate further interest in this subject.

References

1. T. M. Rice, Solid State Phys. 32, 1 (1977); J. C. Hensel, T. G. Phillips, and G. A. Thomas, Solid State Phys. 32, 88 (1977).
2. S. Freeman and J. J. Hopfield, Phys. Rev. Lett. 21, 910 (1968); Y. Tanabe, K-I. Gondaira, and H. Murata, J. Phys. Soc. Japan 25, 1562 (1968); J. B. Parkinson and R. Loudon, J. Phys. C (Proc. Phys. Soc.) 1, 1568 (1968).
3. R. J. Elliott, M. F. Thorpe, G. F. Imbusch, R. Loudon, and J. B. Parkinson, Phys. Rev. Lett. 21, 151 (1968).
4. S. W. Lovesey, J. Phys. C : Solid State Phys. 5, 2769 (1972).
5. R. M. Macfarlane and A. C. Luntz, Phys. Rev. Lett. 31, 832 (1973).
6. R. L. Greene, D. D. Sell, W. M. Yen, A. L. Schalow, and R. M. White, Phys. Rev. Lett. 15, 656 (1965).
7. The E_1 exciton line is inhomogeneously broadened with a typical linewidth of 0.5 cm^{-1}. See Section IV.
8. S. E. Stokowski and D. D. Sell, Phys. Rev. B3, 208 (1971); S. E. Stokowski, D. D. Sell, and H. J. Guggenheim, Phys. Rev. B4, 3141 (1971).
9. T. Fujiwara, J. Phys. Soc. Japan 34, 36 (1973).
10. P. A. Wolff, Phys. Rev. 120, 814 (1960); T. Izuyama, D.-J. Kim, and R. Kubo, J. Phys. Soc. Japan 18, 1025 (1963).
11. These are typical numbers.
12. K. G. Spears, Laser Focus 14, 96 (1978).
13. J. F. Holzrichter, R. M. Macfarlane, and A. L. Schawlow, Phys. Rev. Lett. 26, 652 (1971).
14. R. E. Dietz, A. Misetich, and H. J. Guggenheim, Phys. Rev. Lett.

16, 841 (1966).

VII. Brillouin Scattering in GaSe

A. Introduction

Brillouin scattering in solids[1,2] has attracted much attention in recent years. It proves to be a very useful technique for materials study. It also gives insight into the fundamental nature of the coupling of the acoustic phonons to the electronic states responsible for the optical properties. In this section, I will present our recent Brillouin scattering experiment results on GaSe.[3] First, this technique will be demonstrated to be a powerful probe of the elastic properties of solids. In particular, all five independent elastic constants of GaSe have been measured accurately. Second, the results on resonant Brillouin scattering will be presented and discussed.

GaSe is a layered compound; its crystal structure has been described in Section II. Due to the weakness of the van der Waals bounding between adjacent layers, GaSe has been thought for some time to be a system with two-dimensional properties. However, recent band structure calculations[4] as well as measurements of optical and electronic transport properties have indicated that GaSe has nearly isotropic electronic states at the forbidden gap.[5] The crystal is easily cleaved along the layers, showing the mechanical properties are anisotropic. It is interesting to measure the sound velocities as functions of propagation direction; the elastic constants can then be deduced. Such measurements have been done using ultrasonic techniques.[6] However, only incomplete information has been obtained. The accuracy of the ultrasonic results is also much lower than that of our Brillouin results.

GaSe is also a semiconductor with a gap energy around 2 eV. It has

been shown in Section II that the Raman cross sections of the optical phonons show resonant behavior as the laser frequency is tuned near the direct gap. Some modes are strongly enhanced while others show antiresonant behavior. Also multiphonon modes show up. It is interesting to investigate the resonant behavior of the acoustic phonons. Such a study has been performed on a few materials, including CdS,[2,7,8] ZnO,[8] GaAs,[9,10] ZnSe,[11] etc. However, no such study has been performed on GaSe previously.

B. Experimental Setup

We have constructed a Brillouin spectrometer with a three-pass, piezoelectrically scanned Fabry-Perot interferometer as the center core. The construction is similar to that of Sandercock[12] and that of Dil and Brody.[13]

All the optical components used were mounted on single piece of 3' × 9' × 2" steel plate for rigidity and stability. The steel plate was put on top of a sand box which in turn was supported by inflated inner tubes. With this arrangement, the building vibration was suppressed to an undetectable level.

The flow diagram of the Brillouin spectrometer is shown in Fig. 1. The laser used for excitation was either a Spectra Physics model 125 He-Ne laser with an output power of 50 mW or a homebuilt CW jet stream dye laser with a typical output power of 100 mW. The dye laser was tunable between 5350 Å and 6600 Å with a linewidth of 2 GHz by inserting one or two etalons in the cavity. It could also be made single-mode by inserting more etalons in the cavity. In that case, the laser linewidth was dominated by jitter and was about 50 MHz. The He-Ne laser had a fixed

linewidth of 2 GHz. The laser linewidth was monitored by a spectrum analyzer during the measurements.

After passing through a polarization rotator, the laser light was focused onto the sample via lens L_1. In the particular case shown in Fig. 1, the backscattering geometry was employed. The same lens used to focus the laser light was also used to collect the scattered light. After passing through the polarizer analyzer A, the scattered light was spatially filtered by lenses L_2, L_3 and pinhole P_1 to eliminate diffusely scattered light. Two corner cubes C_1 and C_2 were used to pass the light three times through the Fabry-Perot interferometer to increase the background rejection ratio. The scattered light was finally filtered by a 1/4 meter J-Y monochromator with a 10 Å bandpass to eliminate sample luminescence and Raman signals, and detected by a cooled FW-130 photomultiplier. Standard photon counting electronics and a multichannel analyzer were used for data collection.

One of the Fabry-Perot mirrors was mounted on three piezoelectric transducers (PZT's). The microprocessor based control box applied linear ramping voltages to these PZT's to mechanically drive the mirror over a distance of about 0.8 μ for an applied 250 V ramp. The control box and the multichannel analyzer were fully synchronized such that each channel in the multichannel analyzer corresponded to a fixed position of the mirror. The photon counts from the photomultiplier were stored in successive channels as the mirror moved. The result was then a Brillouin spectrum. The ramping voltages were applied repetitively to facilitate signal averaging. The ramping frequency was adjustable and was typically a few Hz. The voltages applied to the PZT's were also DC biased. These DC bias voltages could be manually adjusted for initial

alignment of the mirrors. Due to thermal and mechanical drifts, the initial alignment would be destroyed after a few minutes. By self-modulating the DC bias voltages and monitoring the transmission peaks of the laser light detected by the photomultiplier, the control box automatically[14] adjusted the DC bias voltages to maintain the alignment indefinitely.

The Fabry-Perot mirrors were purchased from Burleigh, Inc. These were flat to $\lambda/200$ and coated for 5500 Å to 6500 Å with a nominal reflectivity of 93% optimized for three-pass operation. The theoretical finesse of the Fabry-Perot system was 78, contrast 3×10^8, and transmission efficiency 83%. The finesse was degraded somewhat by the modulation of the DC bias voltages applied to the PZT's; the measured value was about 60. Since the intensity of the elastically scattered laser light from the sample surface was typically 10^7 or even more stronger than the Brillouin signals, the high constrast value of 3×10^8 associated with the three-pass configuration was a necessity. A usual single-pass system using mirrors with 96% reflectivity would have a contrast value of 1.5×10^3, far from enough. The free spectral range of the system was adjustable and was fixed at 92.0 GHz during the measurements.

Lenses L_1, L_2, L_3, and L_4 had focal lengthes equal to 4.9, 6.7, 6.7, and 6.7 cm, respectively. These were coated achromatic plano-convex lenses with clear apertures 0.5 cm in diameter. The half collecting angle within the sample was about 1° which was about our angular resolution. Pinholes P_1 and P_2 had diameters of 100 μ. The pinhole finesse,[15] being equal to 700, was much greater than the Fabry-Perot finesse. Its effect on overall resolution could therefore be negelected.

C. Sound Velocity Measurements

(i) Experiment and results

In order to propagate sound waves in any possible direction in the crystal, three scattering geometries including backward scattering, reflection scattering, and nearly 90° scattering, shown in Fig. 2, were used. The sample had a cleaved surface perpendicular to the $\hat{c}$-axis and a polished surface nearly parallel to the $\hat{c}$-axis, and was mounted on a goniometer type mount for angle measurements. The He-Ne laser was used as the excitation source. Some typical spectra obtained in different scattering geometries were included in Fig. 2. From the scattering geometry, the momenta of the phonons were calculated in the usual manner.[16] The indices of refraction used in the calculation were taken from Ref. 17. From the measured Brillouin shifts and calculated momenta, the sound velocities as functions of propagation directions were obtained and summarized in Fig. 3. The results were obtained at room temperature and were independent of incident laser power indicating no appreciable local heating. The absolute Brillouin scattering cross sections were not measured since the collection efficiencies were difficult to estimate with high accuracy. The widths of the Brillouin modes could in principle be used to deduce the phonon damping parameters. However, the experimentally observed widths were often broadened by crystal imperfections. Thus, the measurements were not so meaningful. The widths of the Brillouin modes shown in Fig. 2 were actually dominated by the laser and instrument linewidths. The polarizations of the Brillouin modes were checked with the theoretical predictions with good agreement.

(ii) Theory and discussion

The space symmetry group of GaSe is D_{3h} ($\bar{6}$m2). There are five in-

depent elastic constants[18] C_{11}, C_{12}, C_{13}, C_{33}, and C_{44}. The equations of motion can be solved straightforwardly[19] to give the sound velocities and polarizations. There is one mode which is purely transverse for all propagation directions; its velocity v_T is given by

$$v_T(\theta) = \left[\tfrac{1}{2}(C_{11} - C_{12})\sin^2\theta + C_{44}\cos^2\theta\right]^{1/2}/\rho \qquad (1)$$

where θ is the angle between propagation direction and the $\hat{c}$-axis, and ρ is the mass density equal to 5.03 g/cm^3 for GaSe.[20] The other two modes are in general mixed TA and LA modes; their velocities are given by

$$v_{\pm}(\theta) = (1/\rho)\Big\{\tfrac{1}{2}(C_{44} + C_{11}\sin^2\theta + C_{33}\cos^2\theta) \pm \tfrac{1}{2}\big[(C_{44} + C_{11}\sin^2\theta - C_{33}\cos^2\theta)^2 - 4C_{44}(C_{11}\sin^2\theta - C_{33}\cos^2\theta)\sin^2\theta + C_{13}(C_{13} + 2C_{44})\sin^2 2\theta\big]^{1/2}\Big\}^{1/2} \qquad (2)$$

At θ = 0 and 90°, the "+" and "−" modes become purely longitudinal and purely tranverse, respectively, hence they are called quasi-longitudinal and quasi-transverse modes, respectively. We have

$$v_+(0) = (C_{33}/\rho)^{1/2}$$

$$v_-(0) = v_-(90°) = v_T(0) = (C_{44}/\rho)^{1/2}$$

$$v_+(90°) = (C_{11}/\rho)^{1/2}$$

$$v_T(90°) = \left[\frac{1}{2}(C_{11} - C_{12})/\rho\right]^{1/2} \tag{3}$$

Therefore, from the measured sound velocities for $\theta = 0$ and 90°, four elastic constants C_{11}, C_{12}, C_{33}, and C_{44} can be deduced. In order to obtain C_{13}, a different propagation direction has to be used.

The solid curves in Fig. 3 are theoretical curves obtained by fitting the data using Eqs.(1) and (2). All five elastic constants have been obtained and are listed in Table I. The accuracy of these values are better than 5% judged by the scattering of the data points. Also shown in Table I are the values obtained by Khalilov et al.[6] using the ultrasonic technique at 1.67 MHz. Some of their values are quite different from ours probably due to the inferior quality of their samples. In particular, they didn't measure C_{13} because measuring C_{13} would require cutting the sample in an oblique plane relative to the cleaved plane. Since GaSe is very soft, cutting the crystal in an oblique plane is very difficult without severe mechanical damaging. In contrast, the Brillouin scattering technique can yield the desired information readily by choosing suitable scattering geometries.

The Brillouin scattering cross section is related to the photoelastic tensor $\overleftrightarrow{p}$ by[1]

$$\sigma_{ij} \propto |\hat{e}_i \hat{e}_j : \overleftrightarrow{p} : (\nabla \vec{u})|^2 \tag{4}$$

where $\hat{e}_i$ and $\hat{e}_j$ are the unit polarization vectors of the incident and scattered light respectively, and $\vec{u}$ is the displacement vector of the phonon field. From the known form of the photoelastic tensor,[1,18] the polarization selection rules can be easily derived. The results for ba-

ckward and 90° scattering geometries are shown in Table II. The data points in Fig. 3 have been checked with these selection rules with good agreement.

The data in Fig. 3 clearly shows the anisotropy of the mechanical properties. For example, the LA velocity is 2.7×10^5 cm/sec for $\theta = 0$, which is much lower than the value of 4.6×10^5 cm/sec for $\theta = 90°$. A good measure of the anisotropy is given by the ratio

$$r = v_+^2(0)/v_+^2(90°) = C_{33}/C_{11} = 0.334 \qquad (5)$$

The same ratio should approach 0 for a two-dimensional solid characterized by zero coupling between layers, and should be 1 for an isotropic solid. For most crystals, $r > 0.5$. The low value of r for GaSe is certainly connected with its layered structure.

(iii) Summary and conclusion

We have measured the sound velocities of the three acoustic modes in GaSe as functions of propagation direction by the Brillouin scattering technique. Accurate values for all the five elastic constants have been deduced; polarization selection rules have been verified. The results show the mechanical properties of GaSe are very anisotropic due to the layered structure of the crystal.

D. Resonant Brillouin Scattering

(i) Experiment and results

In measuring the resonant behavior of the acoustic phonon modes, the tunable dye laser was used as the excitation source. The experiment was done at room temperature with the scattering geometry shown in Fig.

2(a) and an incidence angle of 70° with respect to $\hat{c}$. Both incident and scattered light were polarized in the scattering plane. In this arrangement, the quasi-TA "-" and the quasi-LA "+" modes were observed simultaneously. The Brillouin cross sections were corrected for absorption in the manner described in Section II. It was found that the cross sections of the quasi-TA and the quasi-LA modes remained proportional over our dye laser tuning range. Therefore it is sufficient to show only the results on the quasi-TA mode. This is given in Fig. 4. Due to the unavoidable strong luminescence when exciting near the absorption edge, the Brillouin signals were lost in the high luminescence background for $\omega_\ell \gtrsim$ 2 eV. Other scattering geometries were also tried and the results were similar.

(ii) Discussion

The direct exciton of GaSe is at 2.005 eV at room temperature. The absorption coefficient near the exciton absorption edge has been measured.[21] The effective absorption coefficient on the Urbach tail for extraordinary light with an incidence angle of 70° is given by

$$\alpha = 5.9 \times \exp(102 \times E - 198) + 1.5 \quad (cm^{-1}) \tag{6}$$

where E is photon energy in eV. This is plotted in Fig. 4 as a solid line.

A simple perturbation theory[2,22] predicts the Brillouin cross sections should be proportional to α^2 (or α) if intraband electron-phonon matrix element is nonzero (or zero). We see from Fig. 4 the Brillouin cross section is essentially a constant while α increases by three orders of magnitude approaching the direct exciton. Therefore there is no

resonant enhancement. In some other scattering geometries, it was possible to follow the Brillouin peaks above the band gap up to 2.1 eV. But in all the cases we studied, no resonant behavior was found. This is the first known example of a crystal with acoustic phonons which show no resonant behavior near the fundamental gap. The tentative interpretation is that the electron-acoustic phonon interaction is quite small for the lowest conduction band and the top valence band of GaSe and the nonresonant Brillouin cross sections are dominated by other electronic transitions. No experimental or theoretical values of the electron-acoustic phonon matrix elements of GaSe are available.

(iii) Summary and conclusion

We have searched for possible resonant enhancement of the Brillouin cross sections of GaSe near the fundamental gap. No resonant behavior has been found. The results seem to suggest the electron-acoustic phonon coupling is small for the fundamental gap. Further experimental and theoretical studies are necessary to verify this assertion.

References

1. R. Vacher and L. Boyer, Phys. Rev. B6, 639 (1972).

2. A. S. Pine, Topics Appl. Phys. 8, 253 (1975).

3. T. C. Chiang, J. Dumas, and Y. R. Shen, Bull. Am. Phys. Soc. 23, 388 (1978); Sol. State Commun., to be published.

4. A. Bourdon, J. de Physique 35, C3-261 (1964); M. Schlüter, Il Nuovo Cimento 13B, 313 (1973).

5. G. Ottaviani, C. Canali, F. Nava, Ph. Schmid, E. Mooser, R. Minder and I. Zschokke, Sol. State Commun. 14, 933 (1974).

6. Kh. M. Khalilov and K. I. Rzaev, Sov. Phys.-Crys. 11, 786 (1967).

7. A. S. Pine, Phys. Rev. B5, 3003 (1972).

8. R. Berkowicz and D. H. R. Price, Sol. State Commun. 14, 195 (1974).

9. D. K. Garrod and R. Bray, Phys. Rev. B6, 1314 (1972).

10. R. G. Ulbrich and C. Weisbuch, Phys. Rev. Lett. 38, 865 (1977).

11. K. Ando and C. Hamaguchi, Sol. State Commun. 16, 57 (1975).

12. J. R. Sandercock, Opt. Commun. 2, 73 (1970).

13. J. G. Dil and E. M. Brody, Phys. Rev. B14, 5218 (1976); J. G. Dil, Ph.D. thesis (Institute of Optics, University of Rochester, 1975) (unpublished), available in print at Phillips Research Lab., Eindhoven, Netherlands.

14. The control box is designed and constructed by the Electronics Shop, Department of Physics, University of California at Berkeley. The detailed feedback algorithms are described in the Brillouin Stabilizer User's Manual, available at the Electronics Shop.

15. Tech Memo on Multipass Fabry Perot, available in print at Burleigh Instruments Inc., 100 Despatch Drive, P.O. Box 388, East Rochester,

New York 14445.

16. R. W. Dixon, IEEE J. Quan. Elect., QE-3, 85 (1967).

17. T. A. McMath and J. C. Irwin, Phys. Status Solidi A38, 731 (1977).

18. J. F. Nye, Physical Properties of Crystals, Oxford : Clarendon, 1960.

19. See, for example, Kittel, Introduction to Solid State Physics, 3rd Edition.

20. J. Dumas, private communication.

21. A. Balzarotti and M. Piacentini, Sol. State Commun. 10, 421 (1972); J. D. Wasscher and J. Dieleman, Phys. Lett. 39A, 279 (1972); R. Le Toullec, N. Piccioli, M. Mejatty, and M. Balkanski, Il Nuovo Cimento, 38B, 159 (1977).

22. R. Loudon, Proc. Roy. Soc. (London) A275, 218 (1963).

TABLE I

Values of the elastic constants of GaSe deduced from our Brillouin scattering experiment and from the ultrasonic measurement of Khalilov and Rzaev (Ref. 6).

	Brillouin Scattering (present experiment)	Ultrasonic Meas. (Khalilov and Rzaev)
Acoustic Phonon Frequency	10 - 40 GHz	1.67 MHZ
C_{11} (gm/cm - sec^2)	1.05×10^{12}	1.02×10^{12}
C_{33}	3.51×10^{11}	3.07×10^{11}
C_{44}	1.04×10^{11}	0.70×10^{11}
C_{12}	3.25×10^{11}	3.24×10^{11}
C_{13}	1.26×10^{11}	Unknown

TABLE II

Polarization selection rules for backward and 90° Brillouin scattering of acoustic phonon modes, "+", "-", and TA, in GaSe. VV, HH, VH, and HV refer to the various polarization configurations.

	Backward Scattering			90° Scattering
	$\theta = 0°$	$0° < \theta < 90°$	$\theta = 90°$	
VV; HH	+	+, -	+	+, -
VH; HV		TA		TA

Figure Captions

Fig. 1 Flow diagram of the Brillouin spectrometer. L_1, L_2, L_3, and L_4 are lenses, A a polarizer, P_1 and P_2 pinholes, C_1 and C_2 corner cube prisms, F.P. Fabry-Perot plates, PMT a photomultiplier, and MCA a multichannel analyzer.

Fig. 2 Typical Brillouin spectra of GaSe obtained in the three scattering geometries: (a) back scattering; (b) reflection scattering; (c) nearly 90° scattering. (a) and (b) were obtained in the HH polarization configuration and (c) in the VV configuration, where H and V refer to polarizations parallel and perpendicular to the scattering plane respectively.

Fig. 3 Velocities of the three acoustic phonon modes in GaSe as functions of the propagation direction. θ is defined as the angle between the crystal $\hat{c}$-axis and the propagation direction. Solid curves are the theoretical curves obtained from Eqs. (1) and (2).

Fig. 4 Measured Brillouin scattering cross-sections (crossed data points) of the "-" phonon mode in GaSe as a function of the incident laser frequency. The scattering geometry was that shown in Fig. 2(a) with an incident angle of 70° with respect to $\hat{c}$ and an HH polarization configuration. The solid curve gives the absorption coefficient of the crystal in this frequency region.

Figure 1

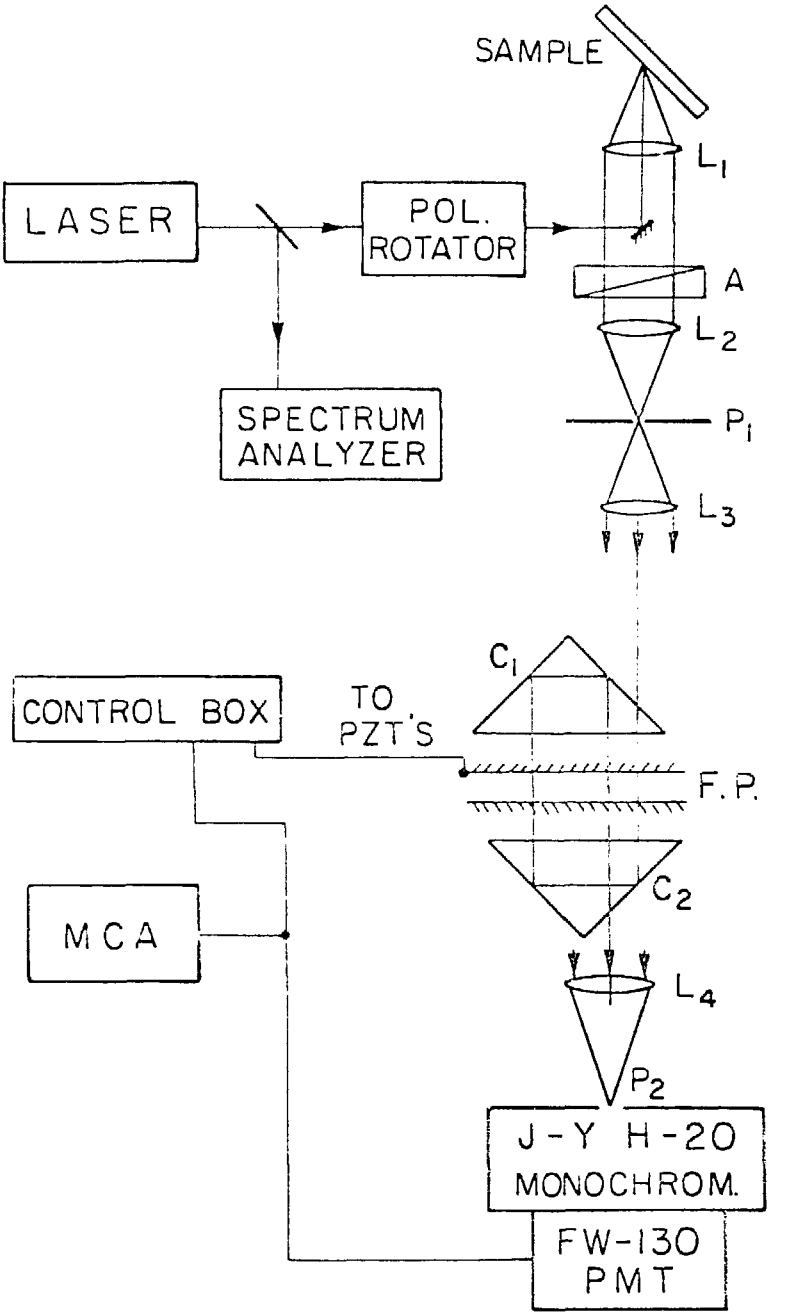

XBL 788-5489

Figure 2

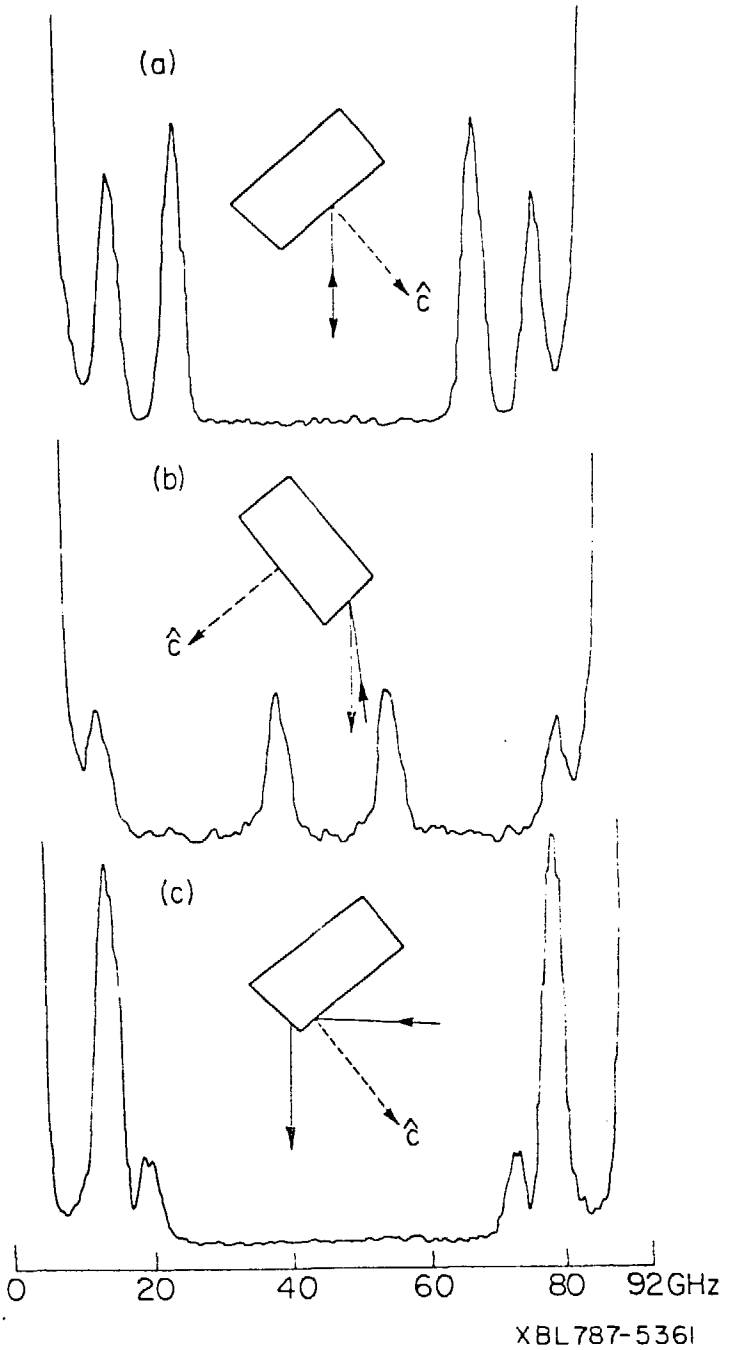

Figure 3

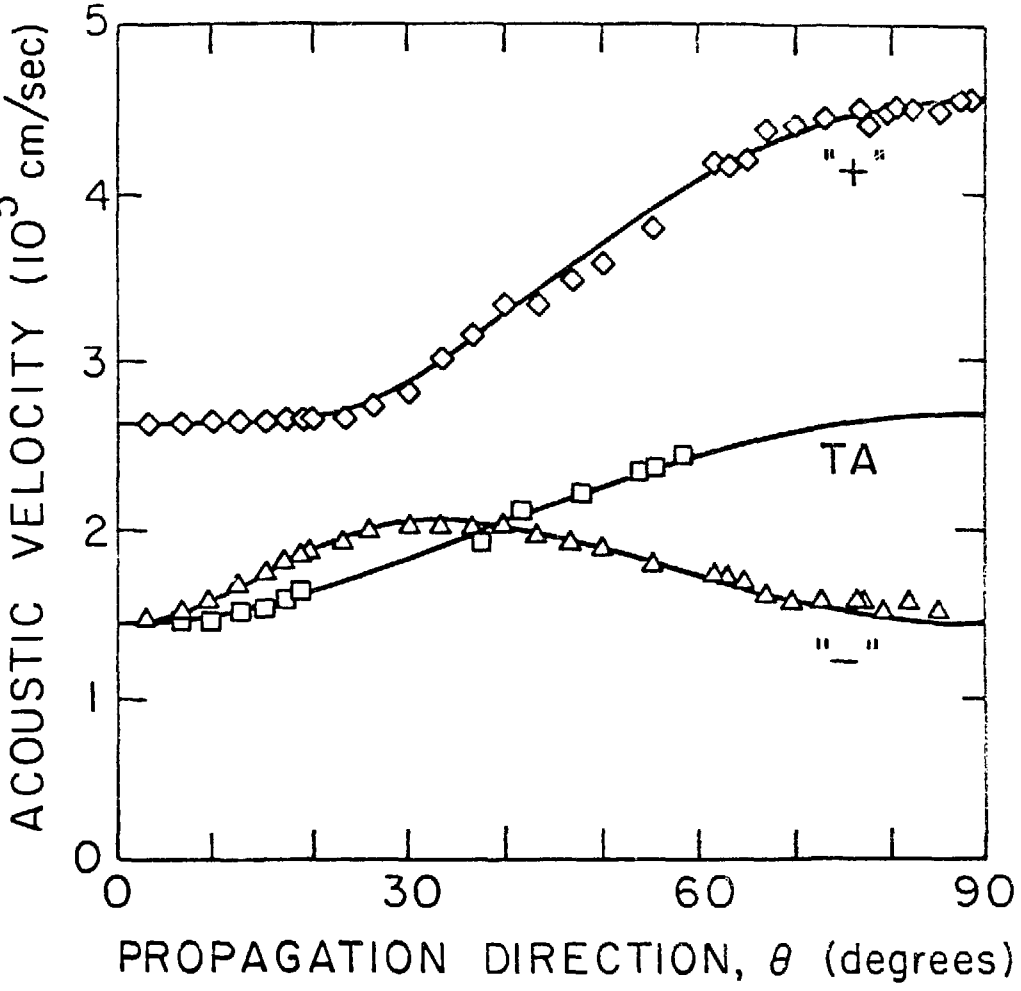

XBL 787-5360

Figure 4

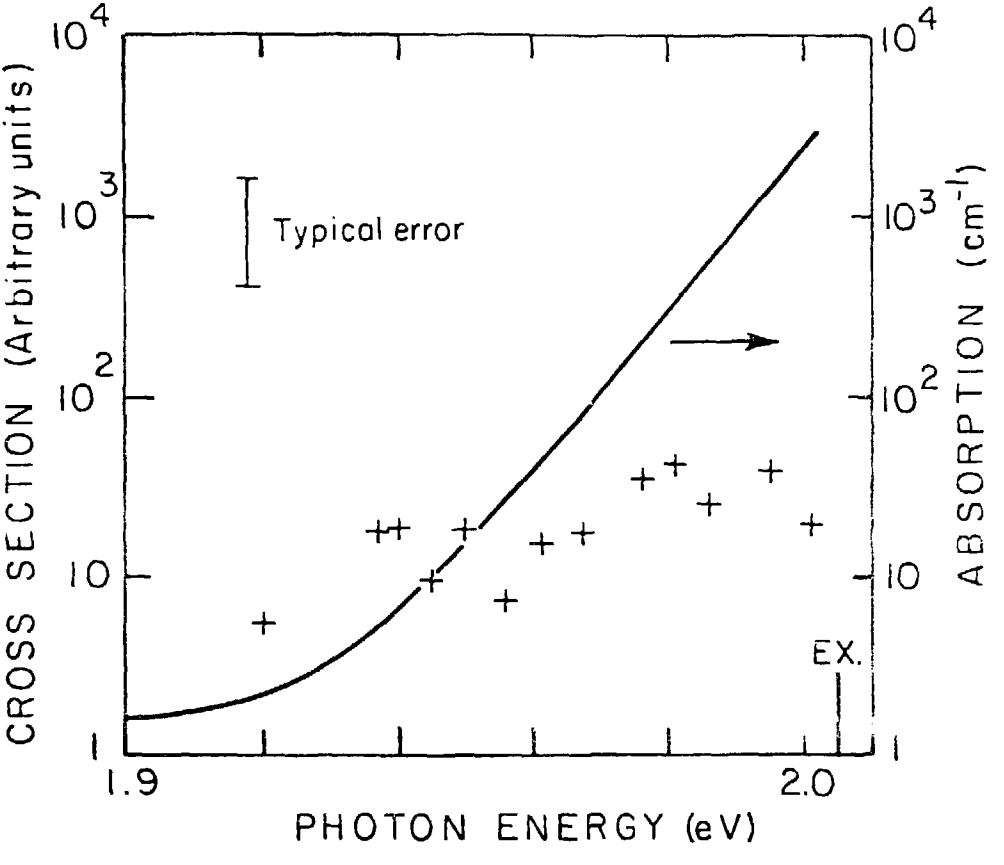

XBL 787-5359

VIII. Two-Photon Parametric Scattering in Sodium Vapor

A. Introduction

Parametric interaction of light waves in nonlinear media has received much attention in recent years.[1] It has proved to be a very important mechanism for generating new frequencies and providing light amplification. One-photon parametric scattering has been well studied both experimentally and theoretically in the literature.[2] I present here a theoretical calculation of the two-photon parametric scattering in sodium vapor. Preliminary experimental result will also be discussed.

The two-photon parametric scattering process is an energy conserving process

$$2\hbar\omega_1 = \hbar\omega_2 + \hbar\omega_3 \tag{1}$$

where two pump photons with energy $\hbar\omega_1$ are converted into one signal photon with energy $\hbar\omega_3$ and an idler photon of energy $\hbar\omega_2$. The nonlinear medium mediates the transition but does not undergo any change itself. Therefore the total photon momentum is also conserved.

$$2\vec{k}_1 = \vec{k}_2 + \vec{k}_3 \tag{2}$$

This is also known as the phase-matching condition.

Sodium vapor, the nonlinear medium in our case, is a centrosymmetric system. Therefore, one-photon parametric scattering is electric dipole forbidden. Although quadrupole transitions have been shown[3] to lead to large nonlinearities suitable for this purpose, we restrict our discus-

sion to the two-photon parametric process because of an easy access to a two-photon resonance.

The spectroscopic data of sodium is well known. There is only one optically active electron. Figure 1 shows a partial energy level diagram.[4] The two-photon parametric process is resonantly enhanced by choosing $2\hbar\omega_1$ close to the 3s → 5s two-photon transition. This is further resonantly enhanced if $\hbar\omega_3$ is close to the single photon transition 5s → 3p or 3p → 3s. The overall process is shown schematically in Fig. 1. Since the transition matrix elements are known, the cross section can be easily calculated.

B. Theory

Let the electric fields of the pump, idler, and signal beams be $\vec{E}_i(t)$ with i = 1, 2, and 3, respectively. We define the complex fields $\vec{E}_i$ by

$$\vec{E}_i(t) = \mathrm{Re}\left(\vec{E}_i\, e^{-i\omega_i t}\right) \tag{3}$$

where Re means the real part. The nonlinear complex polarization at the signal frequency ω_3 is defined by

$$\vec{P}_3 = 3\overleftrightarrow{\chi}^{(3)}(\omega_3 = 2\omega_1 - \omega_2) \vdots \vec{E}_1\vec{E}_1\vec{E}_2^* \tag{4}$$

where $\overleftrightarrow{\chi}^{(3)}$ is the third order nonlinear susceptibility and the factor 3 is the degeneracy factor. $\overleftrightarrow{\chi}^{(3)}$ can be calculated[5] using the perturbation theory within the dipole approximation. Assuming two-photon near resonance with the 3s → 5s transition, we have

$$\overleftrightarrow{\chi}^{(3)} = -\frac{Ne^4}{12\hbar^3}\sum_{n,m,n',m'} \langle 3s\ 0|\vec{r}|n'pm'\rangle\langle n'pm'|\vec{r}|5s\ 0\rangle\langle 5s\ 0|\vec{r}|npm\rangle$$

$$\langle npm|\vec{r}|3s\ 0\rangle \frac{1}{(2\omega_1 - \omega_{5s})}\left[\frac{2}{3}\frac{1}{\omega_1 - \omega_{nP_{3/2}}} + \frac{1}{3}\frac{1}{\omega_1 - \omega_{nP_{1/2}}}\right] \times$$

$$\left[\frac{2}{3}\frac{1}{\omega_3 - \omega_{n'P_{3/2}}} + \frac{1}{3}\frac{1}{\omega_3 - \omega_{n'P_{1/2}}} + \frac{2}{3}\frac{1}{\omega_2 - \omega_{n'P_{3/2}}} + \right.$$

$$\left.\frac{1}{3}\frac{1}{\omega_2 - \omega_{n'P_{1/2}}}\right] \qquad (5)$$

N is the number of sodium atoms per unit volume, e is the electronic charge. The dipole matrix elements are evaluated with respect to the basis vectors $|n\ell m\rangle$, where n is the principal quantum number, ℓ = s, p, etc. the orbital-angular-momentum quantum number, and m the magnetic quantum number. Due to spin-orbit interaction, np state is split into $nP_{3/2}$ and $nP_{1/2}$ states. To first order approximation, these two levels contribute 2/3 and 1/3 of the total oscillator strength of the transition, respectively.[6] Hyperfine interaction has been neglected in Eq. (5).

It is clear from Eq. (5) that $\overleftrightarrow{\chi}^{(3)}$ is symmetric with respect to interchange of ω_2 and ω_3. Since a sodium atom has spherical symmetry, it can be shown the only non-vanishing components of $\overleftrightarrow{\chi}^{(3)}$ are

$$\chi^{(3)}_{xxxx} = \chi^{(3)}_{yyyy} = \chi^{(3)}_{zzzz}$$

$$\chi^{(3)}_{xxyy} = \chi^{(3)}_{yyxx} = \chi^{(3)}_{yyzz} = \chi^{(3)}_{zzyy} = \chi^{(3)}_{zzxx} = \chi^{(3)}_{xxzz}$$

$$\chi^{(3)}_{xyxy} = \chi^{(3)}_{yxyx} = \chi^{(3)}_{yzyz} = \chi^{(3)}_{zyzy} = \chi^{(3)}_{zxzx} = \chi^{(3)}_{xzxz}$$

$$\chi^{(3)}_{xyyx} = \chi^{(3)}_{yxxy} = \chi^{(3)}_{yzzy} = \chi^{(3)}_{zyyz} = \chi^{(3)}_{zxxz} = \chi^{(3)}_{xzzx} \qquad (6)$$

Since we retain only the 5s two-photon resonant intermediate state in Eq. (5), the only significant components of $\overleftrightarrow{\chi}^{(3)}$ are[6]

$$\chi^{(3)}_{xxxx} = \chi^{(3)}_{yyyy} = \chi^{(3)}_{zzzz} = \chi^{(3)}_{xxyy} = \chi^{(3)}_{yyxx} =$$

$$\chi^{(3)}_{yyzz} = \chi^{(3)}_{zzyy} = \chi^{(3)}_{zzxx} = \chi^{(3)}_{xxzz} \tag{7}$$

The interaction Hamiltonian is obtained from the classical energy expression, and is given by

$$H = \frac{3}{4}\int d^3r\ \overleftrightarrow{\chi}^{(3)} \vdots\ \vec{E}_1\vec{E}_1\vec{E}_2^*\vec{E}_3^* \tag{8}$$

The electric field is quantized in the usual way

$$\vec{E}(r,t) = \frac{1}{2}\sum_{\vec{k}}\left(\frac{8\pi\hbar\omega}{V}\right)^{\frac{1}{2}}\frac{1}{n(\omega)}\left[\vec{a}_k\, e^{i(\vec{k}\cdot\vec{r} - \omega t)} + \vec{a}_k^{+}\, e^{-i(\vec{k}\cdot\vec{r} - \omega t)}\right] \tag{9}$$

where V is the volume of quantization, $n(\omega)$ the index of refraction at angular frequency ω, and $\vec{a}_k$ and $\vec{a}_k^{+}$ the photon annihilation and creation operators, respectively. Combining Eqs. (8) and (9), we obtain

$$H = \frac{48\pi^2\hbar^2}{V}\,\frac{(\omega_1^2\omega_2\omega_3)^{\frac{1}{2}}}{n^2(\omega_1)n(\omega_2)n(\omega_3)}\,\chi_{3211}\,\delta_{2\vec{k}_1 - \vec{k}_2 - \vec{k}_3}\, a_2^{+}\, a_3^{+}\, a_1\, a_1$$

with

$$\chi_{3211} \equiv \chi^{(3)} \vdots\ \hat{e}_1\hat{e}_1\hat{e}_2\hat{e}_3 \tag{10}$$

where $\hat{e}_i$ is the polarization vector of the i-th field. The initial and

final states of the process are assumed to be incoherent; they are given by

$$|i\rangle = \frac{1}{(n_1!)^{\frac{1}{2}}} (a_1^+)^{n_1} |0\rangle$$
$$|f\rangle = \frac{1}{[(n_1-2)!]^{\frac{1}{2}}} (a_1^+)^{n_1-2} a_2^+ a_3^+ |0\rangle \tag{11}$$

respectively, where n_1 is the number of pump photons in volume V, and $|0\rangle$ the vacuum state. The transition probability is given by the Fermi golden rule. Neglecting pump depletion, we obtain

$$W = 4608 \frac{\pi^5}{c^2} I_1^2 |\chi_{2311}|^2 \frac{\omega_2\omega_3}{n^2(\omega_1)n^2(\omega_2)n^2(\omega_3)} \delta(2\vec{k}_1 - \vec{k}_2 - \vec{k}_3) \times$$
$$\delta(2\omega_1 - \omega_2 - \omega_3) \tag{12}$$

where

$$I_1 = \frac{n_1}{V} \frac{c}{n(\omega_1)} \hbar\omega_1 \tag{13}$$

is the pump intensity. Energy and momentum conservations are described by the two δ-functions. For a given ω_3, ω_2 is determined by Eq. (1). The magnitudes of $\vec{k}_1$, $\vec{k}_2$, and $\vec{k}_3$ are determined by

$$k_i = \omega_i n(\omega_i)/c \tag{14}$$

By Eq. (2), the scattering geometry is then uniquely determined and is shown in the inset of Fig. 2. The scattering angle θ_3 is given by

$$\theta_3 = \theta_3(\omega_3) = \cos^{-1}[(k_3^2 + 4k_1^2 - k_2^2)/4k_1k_3] \tag{15}$$

with a similar expression for θ_2. Conversely, if θ_3 (direction of observation) is defined first, $\vec{k}_2$, $\vec{k}_3$, ω_2, and ω_3 are all determined to within an exchange of signal and idler waves. In other words, for a given spectrometer setting, signal can be seen only for one particular θ_3; for a given direction of observation θ_3, siganl can be detected only at two wave-lengths. This is important in distinguishing a parametric process from other processes, e.g., a Raman process. For a Raman process, the atom undergoes a transition and picks up any possible recoil momentum, hence the scattered photon has arbirtary direction.

To obtain the cross section, Eq. (12) is summed over $\vec{k}_2$ and its polarization. For simplicity, we assume the pump light is linearly polarized (at any angle with respect to the scattering plane) and we do not analyze the polarization of the signal light. We obtain

$$\frac{d^2n_3}{dt\, d\lambda_3} = 1152\,\pi^3\,\frac{V|\chi|^2I_1^2}{c^5}\left[1 + \cos^2(\theta_2 - \theta_3)\right]\frac{\omega_2\omega_3^3\, n(\omega_3)}{n^2(\omega_1)n^2(\omega_2)}\left|\frac{d\theta_3}{d\lambda_3}\right| \tag{16}$$

where $d^2n_3/dt\, d\lambda_3$ is the number of scattered signal photons per unit time per unit wavelength (measured in air) and χ is $\chi^{(3)}_{zzzz}$. This is the quantity most easily measured experimentally. We can also measure the angular distribution given by

$$\frac{d^2n_3}{dt\, d\theta_3} = 1152\,\pi^3\,\frac{V|\chi|^2I_1^2}{c^5}\left[1 + \cos^2(\theta_2 - \theta_3)\right]\frac{\omega_2\omega_3^3\, n(\omega_3)}{n^2(\omega_1)n^2(\omega_2)} \tag{17}$$

To evaluate $\theta_3(\omega_3)$ by Eq. (15) and the cross section by Eq. (16) or

(17), the refractive index is required. This is given by the Sellmeier formula

$$(n + i\kappa)^2 = 1 + \frac{4\pi Ne^2}{m_0}\sum_n f_{np}\left[\frac{2}{3}\frac{1}{\omega_{nP_{3/2}}^2 - \omega^2} + \frac{1}{3}\frac{1}{\omega_{nP_{1/2}}^2 - \omega^2}\right] \tag{18}$$

from which n and κ can be obtained separately. m_0 is the electron mass. f_{np} is the oscillator strength of the np level. The spin-orbit interaction has been taken into account.

The energy eigenvalues in Eqs. (16), (17) and (18) are in general complex.[7] For a given level j,

$$\omega_j = \mathrm{Re}(\omega_j) - i\gamma_j(N)/2 \tag{19}$$

where $\gamma_j(N)$ is the full width at half maximum of the level and is a function of N.

$$\gamma_j(N) = \gamma_j(0) + \delta\gamma_j \times N/N_0 \tag{20}$$

where $\gamma_j(0)$ is the natural linewidth, $\delta\gamma_j$ the self-broadened linewidth at standard temperature and pressure, and $N_0 = 2.69 \times 10^{19}$ /cm^3.

We have numerically evaluated Eqs. (15) and (17) by assuming the following experimental conditions. A CW dye laser with 100 mW output power and a wavelength of 6020 Å focused down to a beam waist of 25 μ is used as the pump source. The detuning from the 3s → 5s transition is 12.7 cm^{-1} assuming a refractive index of 1.0002765 for air. The scattering volume has a length of 0.5 cm determined by the collection optics. The scattered light travels a distance of 3 cm in the sodium vapor of

uniform density 7×10^{16} atoms/cm^3 before being collected and detected. The linear absorption of the sodium vapor is taken into account. The levels to be considered in the summation in Eqs. (15) and (17) are limited to n = 3, 4, 5, and 6. The relevant quantities are listed in Table I.[7] The results on $\theta_3(\lambda_3)$ and $d^2n_3/dt\, d\lambda_3$ are shown in Figs. 2 and 3, respectively. It is clear from Fig. 2 that the anamolous dispersion associated with the 3s → 3p transition renders the phase matching angle θ_3 large near 5900 Å and 6300 Å. This is desirable experimentally, since the pump light can then be easily rejected spatially. Phase matching for $\theta_3 \lesssim$ 5900 Å and $\theta_3 \gtrsim$ 6300 Å is not possible. From Fig. 3, we see the process is strongly resonantly enhanced near the 5s → 3p and 3p → 3s transitions, but the enhancement near the 3p → 3s transition is more than offset by the strong absorption of the sodium vapor at this wavelength.

C. Experiment

We have performed preliminary experiment in order to verify the theory. The Raman setup described in previous sections was used. A focused CW dye laser beam with a beam convergence $\lesssim 1°$ was used as the pump source. A heat pipe oven produced the uniform sodium vapor. The principle of use and construction of the heat pipe oven have been described in detail in Ref. 6. A mask with an annular cutaway was put after the oven to define the range of scattering angle θ_3. Typical anaular resolution defined by the mask was about 1°. The scattered light was detected by a double monochromator followed by a photomultiplier and photon counting electronics. The relevant experimental parameters were approximately as stated in the last paragraph, hence the results shown

in Figs. 2 and 3 were expected. We tried to determent $d^2n_3/dt\, d\lambda_3$ within certain range of θ_3 with a spectrometer resolution of ~ 1 Å. The overall photon detection efficiency of our system was $\lesssim 1\%$, considering the reflection loss due to the optical elements, spectrometer efficiency, photomultiplier quantum yield, etc. A maximum count rate of about 10^3 /sec was expected near $\lambda_3 = 6148$ Å according to Fig. 3.

The experimental results were disappointing. The sodium dimers, Na_2, though present only in small amount, gave out enormous amount of fluorescence[8] ($> 10^6$ counts /sec) which totally swamped the parametric signal. We tried to lower the relative dimer concentration by reducing the sodium vapor density, but the expected signal was also lowered. In all the cases we tried, either the dimer fluorescence dominated the spectra or no signal at all was observed above noise.

D. Discussion

A better experimental approach is to use low sodium density and a pulsed laser as the pump source. Since the two-photon parametric process depends quadratically on the pump intensity while the dimer fluorescence depends only linearly on the pump intensity, the signal to background ratio can be greatly increased with the high peak power from the pulsed laser. However, stimulated emission may occur at high enough pump intensity. The transition from a spontaneous scattering process to a stimulated process is an interesting and yet complicated problem. A mathematical treatment is not attempted here.

Another possible approach is to use a different atomic vapor such as strontium which has low dimer concentration, or an atomic vapor whose dimer fluorescence is very weak. However, a good candidate should also

have energy levels in the right energy range for convenient pumping.

E. Summary

We have derived the expression for the cross section of the two-photon parametric process in sodium vapor near the 3s → 5s transition. A numerical example is worked out. Preliminary experiment has not been successful due to the presence of strong dimer fluorescence. Future experiment using a pulsed laser or a different atomic vapor is suggested.

References

1. See, for example, S. A. Akhmanov and R. V. Khohklov, Soviet Phys.-Usp. 9, 210 (1966).

2. W. H. Louisell and A. Yariv, Phys. Rev. 124, 1646 (1961); S. E. Harris, M. K. Oshman, and R. L. Byer, Phys. Rev. Lett. 18, 732 (1967); R. L. Byer and S. E. Harris, Phys. Rev. 168, 1064 (1968); D. Madge and H. Mahr, Phys. Rev. 171, 393 (1968); T. G. Giallorenzi and C. L. Tang, Phys. Rev. 166, 225 (1968).

3. D. S. Bethune, R. W. Smith, and Y. R. Shen, Phys. Rev. Lett. 37, 431 (1976).

4. Striganov and Sventiskii, Tables of Spectral Lines of Neutral and Ionized Atoms, IFI/Plenum, New York-Washington (1968).

5. See, for example, N. Bloembergen, Nonlinear Optics, Benjamin, New York (1965).

6. D. S. Bethune, Ph. D. thesis, Department of Physics, University of California at Berkeley (1977), unpublished.

7. R. B. Miles and S. E. Harris, IEEE J. Quant. Elect. QE-9, 470 (1973).

8. M. M. Hessel, E. W. Smith, and R. E. Drullinger, Phys. Rev. Lett. 33, 1251 (1974)

TABLE I

Parameters for sodium vapor used in Eqs. (16)-(20).

np	$\omega/2\pi c$ (cm^{-1})	$\gamma(0)/2\pi c$ (cm^{-1})	$\delta\gamma/2\pi c$ (cm^{-1})	f	$\langle 3s\|z\|np\rangle\langle np\|z\|5s\rangle$ ((Bohr radius)^2)
3p $^2P_{1/2}$	16956.18	3.3×10^{-4}	68.3	0.982	-1.3253
3p $^2P_{3/2}$	16973.38	3.3×10^{-4}	78.9		
4p	30270.63	1.5×10^{-5}	0.35	0.0142	-1.3912
5p	35041.95	3.1×10^{-6}	0.05	0.00221	0.9374
6p	37297.34	0	0	0.00073	0.0633

Figure Captions

Fig. 1 Partial energy level diagram of the sodium atom. Two photon parpmetric process with $2\omega_1 = \omega_2 + \omega_3$ is shown schematically.

Fig. 2 The phase-matching angle θ_3 as a function of wavelength λ_3 for $n = 7 \times 10^{16}$ atoms/cm^3. The inset shows schematically the scattering geometry.

Fig. 3 The calculated scattering cross section $d^2n_3/dt\, d\lambda_3$ as a function of λ_3 under the experimental conditions stated in the text.

Figure 1

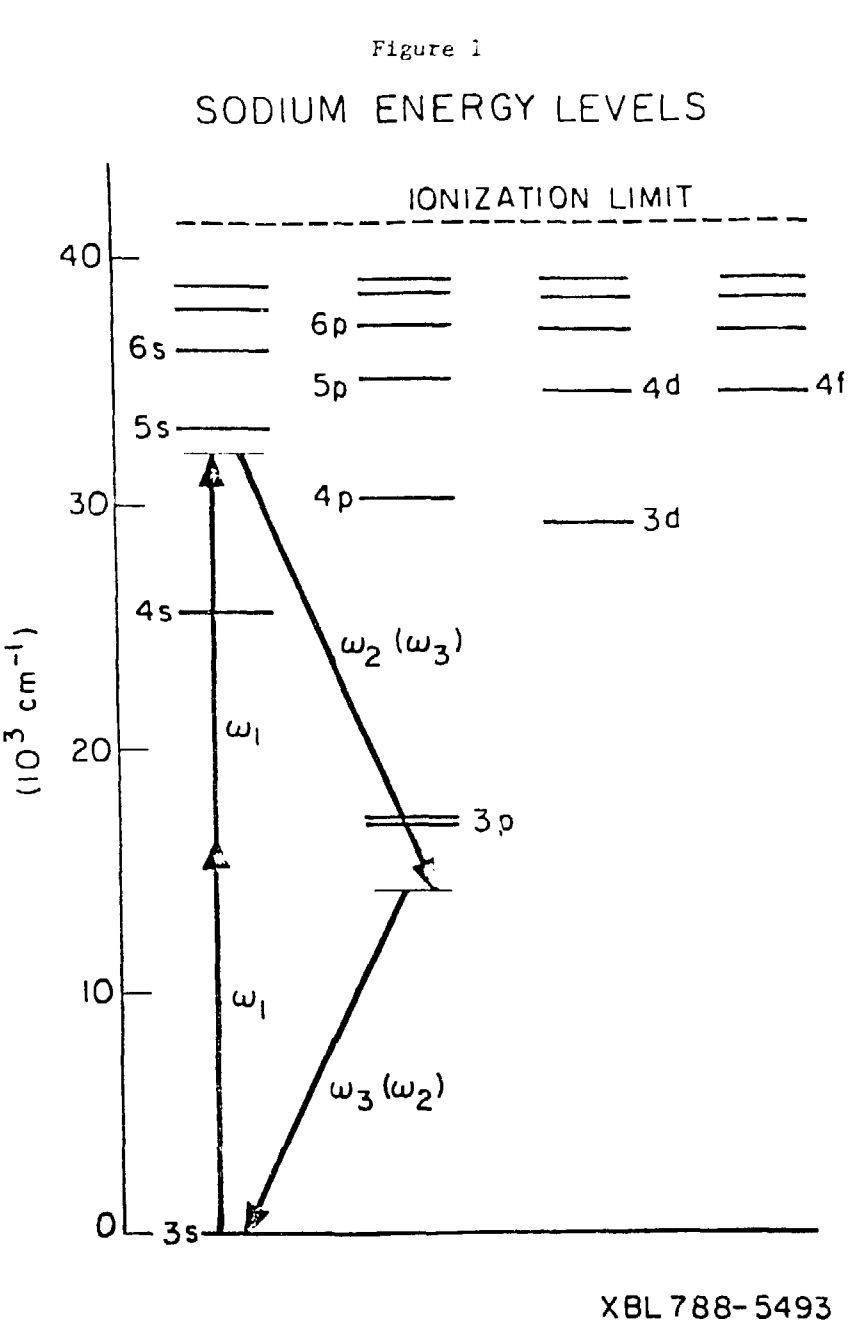
SODIUM ENERGY LEVELS
IONIZATION LIMIT
40
30
20
10
0
(10³ cm⁻¹)
6s
5s
4s
3s
6p
5p
4p
3p
4d
3d
4f
ω1
ω1
ω2 (ω3)
ω3 (ω2)
XBL 788-5493

Figure 2

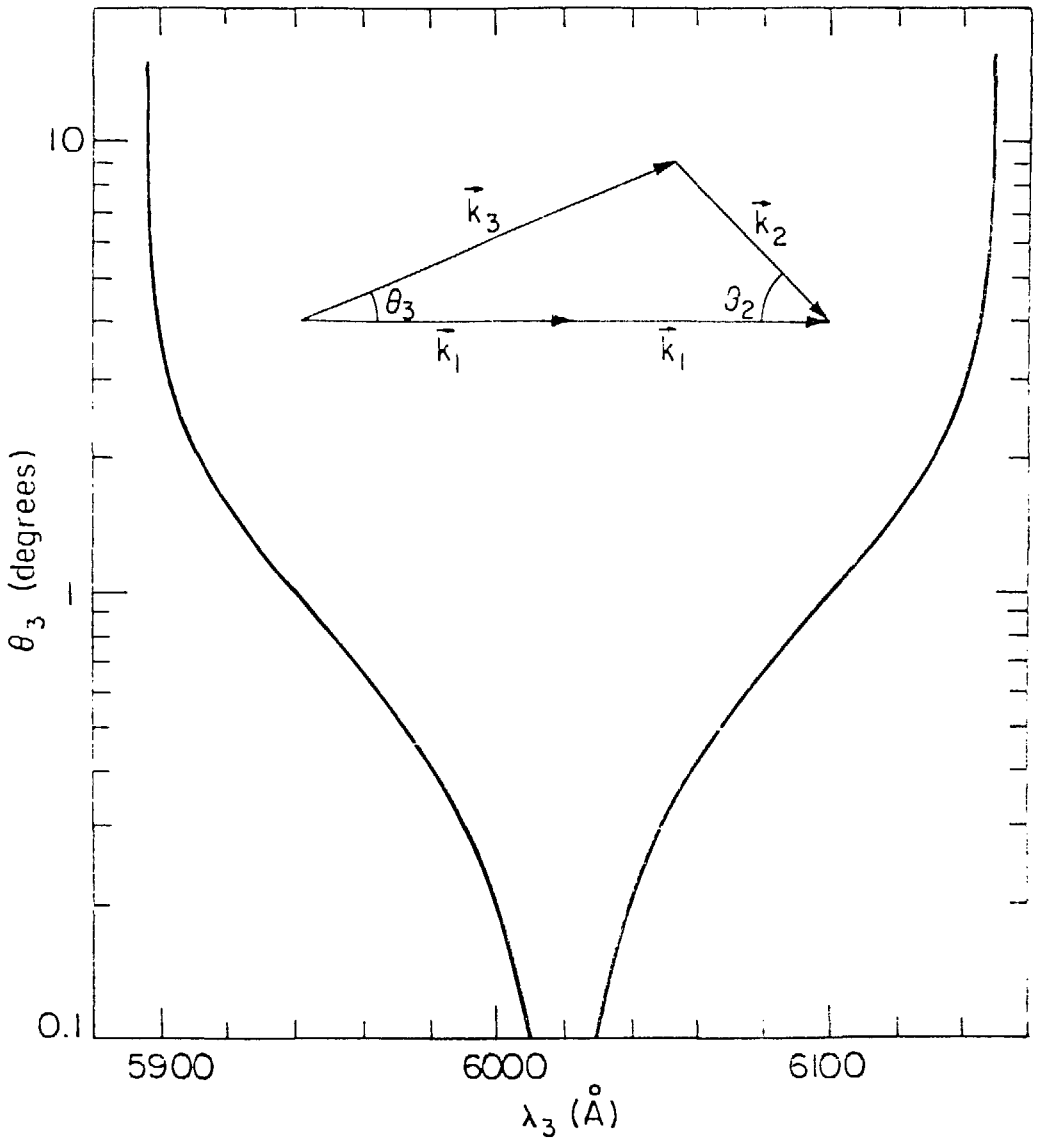

XBL 788-5494

Figure 3

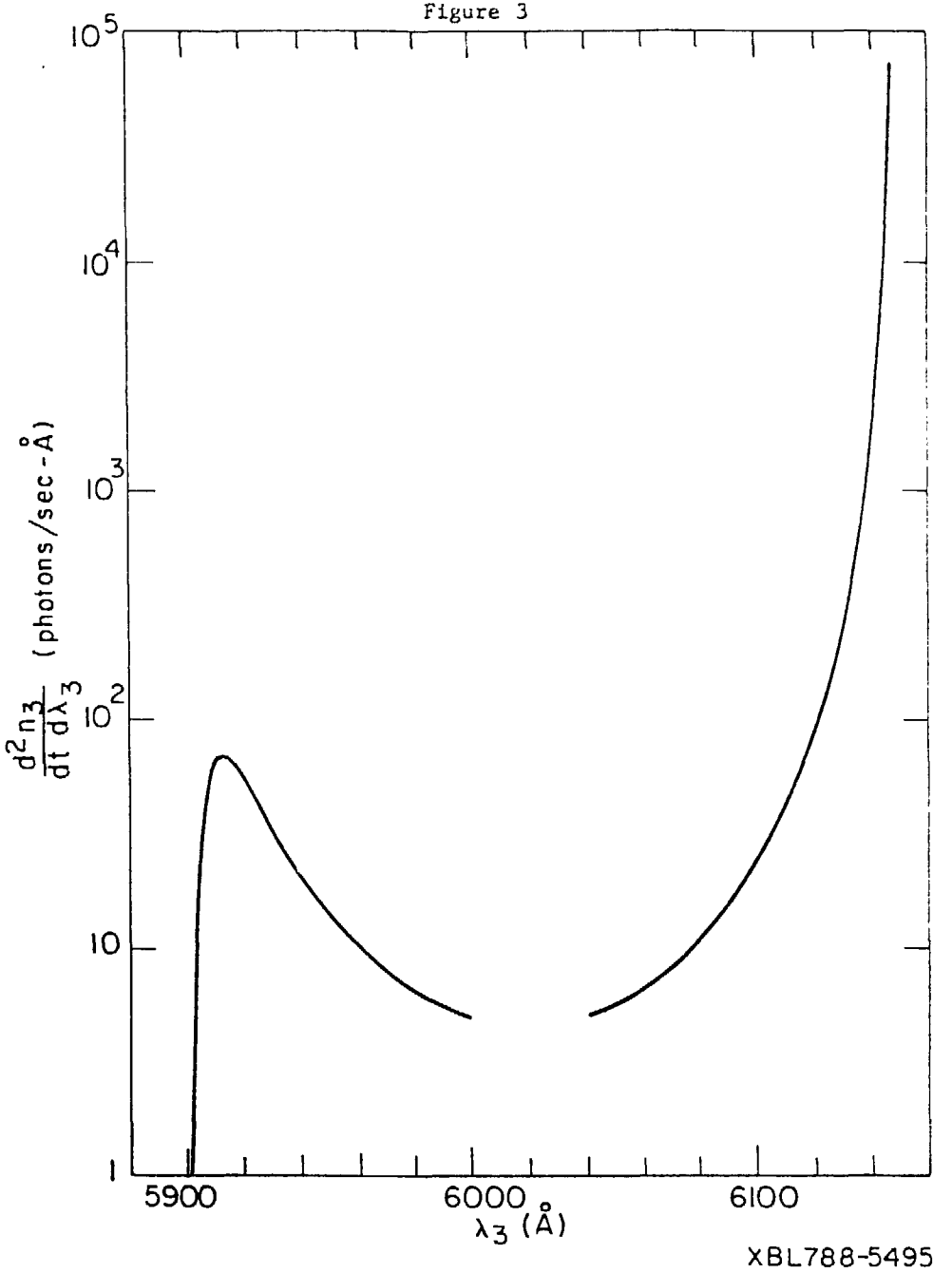
10^5
10^4
10^3
10^2
10
1
$\frac{d^2 n_3}{dt\, d\lambda_3}$ (photons/sec-Å)
5900
6000
6100
λ_3 (Å)
XBL788-5495